Ion-beam processes in group-III nitrides

Sergei Olegovich Kucheyev

A thesis submitted for the degree of

Doctor of Philosophy

of

The Australian National University

March 2002

CERTIFICATE

This thesis, to the best of my knowledge and belief, does not contain any results previously published by another person or submitted for a degree or diploma at any university except where due reference is made in the text.

_____

Sergei O. Kucheyev

Посвящается моим родителям

Acknowledgments

The work presented in this thesis was done under the supervision of Prof. James S. Williams and Prof. Chennupati Jagadish at the Department of Electronic Materials Engineering, Research School of Physical Sciences and Engineering, ANU. I wish to express my deepest appreciation and gratitude to Profs. Williams and Jagadish for their introduction to an amazing field of experimental physics and materials research and for their invaluable support and guidance throughout the course of this work, which made my Ph.D. years a truly exciting and dynamic experience.

I wish to thank (i) Dr. Miloš Tóth (University of Cambridge) for numerous helpful discussions and for participating in some of the CL experiments presented in this thesis, (ii) Dr. Matthew R. Phillips (University of Technology, Sydney) for a fruitful collaboration on CL studies, (iii) Dr. Jin Zou (University of Sydney) for a number of helpful discussions and for conducting much of the TEM characterization presented here, (iv) Jodie E. Bradby (ANU) for helpful discussions and for performing nanoindentation measurements, (v) Prof. Henri Boudinov (UFRGS, Brazil) for fruitful discussions and for his assistance with electrical measurements, (vi) Dr. Vincent S. J. Craig and Dr. Tim J. Senden (ANU) for their assistance with AFM measurements, and (vii) Dr. Margareta Linnarsson and Prof. Bengt Svensson (Royal Institute of Technology, Sweden) for SIMS measurements. My understanding of CL, TEM, nanoindentation, electrical characterization, AFM, and SIMS techniques greatly increased through many discussions with all these collaborators.

I thank Dr. Gang Li (Ledex Corp.) for supplying most of the samples investigated. Dr. Y. Nakagawa (Nichia Corp.) and Dr. M. Pophristic, Dr. S. Guo, and Dr. I. T. Ferguson (EMCORE Corp.) have kindly supplied some of the AlGaN and AlN samples studied.

I thank Prof. Stephen J. Pearton (University of Florida) for his continuous support during the course of this work and Prof. Andrey Ivanovich Titov (St. Petersburg State Technical University) for numerous discussions stimulating my research. Prof. Robert G. Elliman, Prof. Michael V. Swain, Prof. John A. Davies, and Dr. Nicolas J. Welham are gratefully acknowledged for helpful discussions.

Finally, I thank staff of the EME — Martin J. Conway, Laura Walmsley, Dr. Michael I. Cohen, Dr. H. Hoe Tan, Anthony J. Watt, Alan H. Hayes, Tom Halstead, Dr. Lan Fu, Dr. Manuela Buda, Dr. Prakash (Sanju) N. K. Deenapanray, Dr. Yin-Yin (Jenny) Wong-Leung, and David J. Llewellyn — for their help with practical aspects of this work.

This work was supported by DETYA of the Australian Government and by the ANU.

Abstract

Group-III-nitride semiconductors (GaN, InGaN, and AlGaN) are important for the fabrication of a range of optoelectronic devices (such as blue-green light emitting diodes, laser diodes, and UV detectors) as well as devices for high-temperature/high-power electronics. In the fabrication of these devices, ion bombardment represents a very attractive technological tool. However, a successful application of ion implantation depends on an understanding of the effects of radiation damage. Hence, this thesis explores a number of fundamental aspects of radiation effects in wurtzite III-nitrides. Emphasis is given to an understanding of (i) the evolution of defect structures in III-nitrides during ion irradiation and (ii) the influence of ion bombardment on structural, mechanical, optical, and electrical properties of these materials.

Structural characteristics of GaN bombarded with keV ions are studied by Rutherford backscattering/channeling (RBS/C) spectrometry and transmission electron microscopy (TEM). Results show that strong dynamic annealing leads to a complex dependence of the damage buildup on ion species with preferential surface disordering. Such preferential surface disordering is due to the formation of surface amorphous layers, attributed to the trapping of mobile point defects by the GaN surface. Planar defects are formed for a wide range of implant conditions during bombardment. For some irradiation regimes, bulk disorder saturates below the amorphization level, and, with increasing ion dose, amorphization proceeds layer-by-layer only from the GaN surface. In the case of light ions, chemical effects of implanted species can strongly affect damage buildup. For heavier ions, an increase in the density of collision cascades strongly increases the level of stable implantation-produced lattice disorder. Physical mechanisms of surface and bulk amorphization and various defect interaction processes in GaN are discussed.

Structural studies by RBS/C, TEM, and atomic force microscopy (AFM) reveal anomalous swelling of implanted regions as a result of the formation of a porous structure of amorphous GaN. Results suggest that such a porous structure consists of N_2 gas bubbles embedded into a highly N-deficient amorphous GaN matrix. The evolution of the porous structure appears to be a result of stoichiometric imbalance, where N- and Ga-rich regions are produced by ion bombardment. Prior to amorphization, ion bombardment does not produce a porous structure due to efficient dynamic annealing in the crystalline phase.

The influence of In and Al content on the accumulation of structural damage in InGaN and AlGaN under heavy-ion bombardment is studied by RBS/C and TEM. Results show that an increase in In concentration strongly suppresses dynamic annealing processes, while an increase in Al content dramatically enhances dynamic annealing. Lattice amorphization in AlN is not observed even for very large doses of keV heavy ions at -196 °C. In contrast to the case of GaN, no preferential surface disordering is observed in InGaN, AlGaN, and AlN. Similar implantation-produced defect structures are revealed by TEM in GaN, InGaN, AlGaN, and AlN.

The deformation behavior of GaN modified by ion bombardment is studied by spherical nanoindentation. Results show that implantation disorder significantly changes the mechanical properties of GaN. In particular, amorphous GaN exhibits plastic deformation even for very low loads with dramatically reduced values of hardness and Young's modulus compared to the values of as-grown GaN. Moreover, implantation-produced defects in crystalline GaN suppress the plastic component of deformation.

The influence of ion-beam-produced lattice defects as well as a range of implanted species on the luminescence properties of GaN is studied by cathodoluminescence (CL). Results indicate that intrinsic lattice defects mainly act as nonradiative recombination centers and do not give rise to yellow luminescence (YL). Even relatively low dose keV light-ion bombardment results in a dramatic quenching of visible CL emission. Postimplantation annealing at temperatures up to 1050 °C generally causes a partial recovery of measured CL intensities. However, CL depth profiles indicate that, in most cases, such a recovery results from CL emission from virgin GaN, beyond the implanted layer, due to a reduction in the extent of light absorption within the implanted layer. Experimental data also shows that H, C, and O are involved in the formation of YL. The chemical origin of YL is discussed based on experimental data.

Finally, the evolution of sheet resistance of GaN epilayers irradiated with MeV light ions is studied *in-situ*. Results show that the threshold dose of electrical isolation linearly depends on the original free electron concentration and is inversely proportional to the number of atomic displacements produced by the ion beam. Furthermore, such isolation is stable to rapid thermal annealing at temperatures up to 900 °C. Results also show that both implantation temperature and ion beam flux can affect the process of electrical isolation. This behavior is consistent with significant dynamic annealing, which suggests

a scenario where the centers responsible for electrical isolation are defect clusters and/or antisite-related defects. A qualitative model is proposed to explain temperature and flux effects.

The work presented in this thesis has resulted in the identification and understanding of a number of both fundamental and technologically important ion-beam processes in III-nitrides. Most of the phenomena investigated are related to the nature and effects of implantation damage, such as lattice amorphization, formation of planar defects, preferential surface disordering, porosity, decomposition, and quenching of CL. These effects are often technologically undesirable, and the work of this thesis has indicated, in some cases, how such effects can be minimized or controlled. However, the thesis has also investigated one example where irradiation-produced defects can be successfully applied for a technological benefit, namely for electrical isolation of GaN-based devices. Finally, results of this thesis will clearly stimulate further research both to probe some of the mechanisms for unusual ion-induced effects and also to develop processes to avoid or repair unwanted lattice damage produced by ion bombardment.

Contents

1 Introduction **1**

1.1 Unique properties and applications of III-nitrides 2

1.2 Motivation 2

1.3 Thesis structure 4

2 Experimental **6**

2.1 Samples 7

2.2 Experimental techniques 8

2.2.1 Introduction 8

2.2.2 Ion implantation 8

2.2.3 Rutherford backscattering/channeling spectrometry 13

2.2.4 Transmission electron microscopy 16

2.2.5 Atomic force microscopy 17

2.2.6 Cathodoluminescence spectroscopy 19

2.2.7 Nanoindentation 20

2.2.8 Electrical characterization 22

2.2.9 Furnace annealing 23

3 Damage accumulation in GaN **24**

3.1 Introduction 25

3.2 Previous damage buildup studies 25

3.3 Experimental 29

3.4 Results 31

3.4.1 Hydrogen 31

3.4.2 Carbon 32

3.4.3 Oxygen 39

3.4.4 Intermediate-mass ions: ^{28}Si, ^{63}Cu, and ^{107}Ag 41
3.4.5 Heavy ions: ^{197}Au and ^{209}Bi 45
3.5 Discussion 56
3.5.1 Effect of ion species 57
3.5.2 Scenario for defect interaction processes 61
3.5.3 Formation of extended defects and their influence on amorphization 66
3.5.4 Saturation of bulk disorder 66
3.5.5 Surface amorphization 67
3.5.6 Chemical effects 72
3.5.7 Role of collision cascade density 73
3.6 Comparison with other materials 76
3.7 Summary 77

4 Ion-beam-induced porosity of GaN 79
4.1 Introduction 80
4.2 Experimental 80
4.3 Swelling and porosity 80
4.4 Voids or gas bubbles? 85
4.5 Stoichiometric imbalance 87
4.6 Summary 88

5 Effect of In and Al content on damage buildup in III-nitrides 89
5.1 Introduction 90
5.2 Experimental 90
5.3 Damage in InGaN 92
5.4 Damage in AlGaN 96
5.5 Damage in AlN 100
5.5.1 Introduction 100
5.5.2 Results and discussion 101
5.6 Summary 107

6 Mechanical properties of ion-implanted GaN 109
6.1 Introduction 110

6.2 Experimental . . . 111
6.3 Results and discussion . . . 112
6.4 Summary . . . 115

7 Optical properties of ion-implanted GaN 117
7.1 Introduction . . . 118
7.2 Experimental . . . 120
7.3 Influence of defects on luminescence and absorption . . . 121
7.4 Thermal annealing of implantation damage . . . 128
7.5 Role of implanted species in yellow luminescence . . . 130
7.5.1 Oxygen . . . 132
7.5.2 Carbon . . . 133
7.5.3 Hydrogen . . . 134
7.6 Discussion of the chemical origin of yellow luminescence . . . 136
7.7 Summary . . . 138

8 Electrical characterization of ion-implanted GaN 140
8.1 Introduction . . . 141
8.2 Experimental . . . 143
8.3 Results and discussion . . . 144
8.3.1 Effect of initial free electron concentration . . . 144
8.3.2 Effect of ion mass . . . 146
8.3.3 Effect of irradiation temperature and beam flux . . . 148
8.4 Summary . . . 153

9 Concluding remarks 155

List of Figures

2.1 Calculated profiles of vacancies produced in GaN by 40 keV C, 100 keV Au, and 300 keV Au ions 9

2.2 ANU 1.7 MV tandem accelerator (NEC, 5SDH-4) 11

2.3 Schematic diagram illustrating detector geometry for RBS/C measurements 16

2.4 Cathodoluminescence system response curve 20

2.5 Schematic diagram of Ohmic contacts for sheet resistance and Hall effect measurements 23

3.1 RBS/C spectra showing the damage buildup for 10 keV H ion bombardment of GaN at LN_2 31

3.2 RBS/C spectra showing the damage buildup for 40 keV C ion bombardment of GaN at LN_2 and RT 33

3.3 RBS/C spectra of GaN implanted to high doses with 40 keV C ions at LN_2 34

3.4 Dark-field XTEM images of the GaN epilayers bombarded at LN_2 with 40 keV C ions to a dose of 8×10^{15} cm^{-2} 36

3.5 (a) Bright-field XTEM image taken from the same GaN sample depicted in Fig. 3.4. (b) Bright-field XTEM image of GaN implanted at LN_2 with 100 keV Au ions to a dose of 3×10^{14} cm^{-2} 36

3.6 Weak-beam XTEM images of the GaN epilayers bombarded with 40 keV C ions to a dose of 1×10^{15} cm^{-2} at LN_2 and RT 37

3.7 Dose dependence of the magnitudes of the bulk and surface defect peaks for 40 keV C and 300 keV Au ion bombardment of GaN at LN_2 and RT . . 38

3.8 Bright-field XTEM images of GaN bombarded with 40 keV C ions at LN_2 and RT to doses of 2×10^{16} and 5×10^{16} cm^{-2} 38

3.9 RBS/C spectra showing the damage buildup for 50 keV O ion bombardment of GaN at LN_2 and RT 40

3.10 Dark-field XTEM images of GaN bombarded at LN_2 with 50 keV O ions to a dose of 6×10^{16} cm^{-2} 41
3.11 RBS/C spectra showing the damage buildup in GaN bombarded at LN_2 with 60 keV Si, 130 keV Cu, and 200 keV Ag ions 42
3.12 RBS/C spectra showing the damage buildup for 60 keV Si ion bombardment of GaN at RT 43
3.13 RBS/C spectra showing the damage buildup for 130 keV Cu ion bombardment of GaN at RT 44
3.14 RBS/C spectra showing the damage buildup for 200 keV Ag ion bombardment of GaN at RT 44
3.15 Dark-field XTEM images of the GaN epilayers bombarded at RT with 60 keV Si ions to a dose of 2×10^{16} cm^{-2} 45
3.16 RBS/C spectra showing the damage buildup for 100 keV Au ion bombardment of GaN at LN_2 and RT 46
3.17 Dark-field XTEM images of the GaN epilayers bombarded with 100 keV Au ions to doses of 2×10^{14} and 3×10^{14} cm^{-2} at LN_2 47
3.18 RBS/C spectra showing the damage buildup for 300 keV Au ion bombardment of GaN at LN_2 and RT 49
3.19 Dose dependence of the magnitudes of the bulk and surface defect peaks for 300 keV Au ion bombardment at LN_2 and RT 50
3.20 Dark-field and bright-field XTEM images of the GaN epilayers bombarded at RT with 300 keV Au ions to doses of 8×10^{13}, 7×10^{14}, and 1.5×10^{15} cm^{-2} 51
3.21 Bright-field XTEM images of GaN implanted with 300 keV Au ions at RT to doses of 8×10^{13} and 7×10^{14} cm^{-2} 51
3.22 RBS/C spectra showing the damage buildup in GaN capped with a SiO_x or Si_xN_y layer. Implantation was carried out with 450 keV Au ions at LN_2 and RT 53
3.23 RBS/C spectra of GaN implanted with 300 keV Au ions to a dose of 3×10^{14} cm^{-2} at LN_2 and RT 55
3.24 RBS/C spectra showing the damage buildup for 500 keV Bi ion bombardment of GaN at LN_2 and RT 56

3.25 Maximum relative disorder in GaN in the bulk defect peak as a function of dose for different ions implanted at LN_2 and RT 58
3.26 Left axis: the ion mass dependence of the ion dose necessary to produce relative disorder of 0.3 by implantation of GaN at LN_2 and RT. Right axis: the dependence of ξ_{M_1} on ion mass 60
3.27 RBS/C spectra illustrating the damage buildup in GaN bombarded at LN_2 with 100 keV, 300 keV, and 2000 keV Au ions 69
3.28 Dependence of the thickness of surface amorphous layers on dpa for bombardment of GaN with 130 keV Cu, 200 keV Ag, and 300 keV Au ions at RT 71

4.1 Tapping-mode AFM image illustrating the border between implanted and unimplanted areas of a GaN sample bombarded with 2 MeV Au ions at LN_2 to a dose of 1×10^{16} cm^{-2} 81
4.2 Dose dependence of the step height between implanted and unimplanted regions of GaN films bombarded with 2 MeV Au ions at LN_2 82
4.3 Bright-field XTEM images of the GaN epilayer bombarded with 2 MeV Au ions at LN_2 to a dose of 1×10^{16} cm^{-2} 82
4.4 Height-mode AFM images of virgin GaN and of GaN bombarded with 2 MeV Au ions at LN_2 to doses of 1×10^{16} and 4×10^{16} cm^{-2} 84
4.5 Bright-field XTEM images of GaN bombarded with 2 MeV Au ions at LN_2 to doses of 5×10^{15}, 1×10^{16}, and 3×10^{16} cm^{-2} 85
4.6 (a) Typical top-view amplitude-mode AFM image of GaN bombarded with 2 MeV Au ions at LN_2 to a dose of 1.2×10^{16} cm^{-2} and subsequently annealed for 10 minutes at 450 °C. (b) Typical bright-field XTEM image of the GaN sample with surface and buried amorphous layers annealed in vacuum at 500 °C for $\sim$ 2 hours 87

5.1 RBS/C spectra illustrating lattice damage in $In_xGa_{1-x}N$ films bombarded at 20 °C with 300 keV Au ions to a dose of 4×10^{13} cm^{-2} 92
5.2 RBS/C spectra showing the damage buildup for 300 keV Au ion bombardment of $In_{0.12}Ga_{0.88}N$ at 20 °C 93

5.3 Dose dependence of relative disorder in the bulk defect peak region for $In_xGa_{1-x}N$ bombarded with 300 keV Au ions at 20 °C 94
5.4 Dark-field XTEM images of an $In_{0.16}Ga_{0.84}N$ epilayer bombarded at 20 °C with 300 keV Au ions to a dose of 4×10^{13} cm^{-2} 95
5.5 XTEM images of an $In_{0.18}Ga_{0.82}N$ epilayer bombarded at 20 °C with 300 keV Au ions to a dose of 2×10^{14} cm^{-2} 96
5.6 RBS/C spectra showing the damage buildup for 300 keV Au ion bombardment of $Al_{0.08}Ga_{0.92}N$ at 20 °C 97
5.7 Dose dependence of maximum relative disorder in the bulk defect peak region for $Al_xGa_{1-x}N$ samples bombarded with 300 keV Au ions at 20 °C . 98
5.8 Dark-field XTEM images of $Al_{0.08}Ga_{0.92}N$ and $Al_{0.19}Ga_{0.81}N$ epilayers bombarded at 20 °C with 300 keV Au ions to doses of 4×10^{15} and 9×10^{15} cm^{-2} 99
5.9 RBS/C spectra showing the damage buildup for 300 keV Au ion bombardment of AlN at −196 and 20 °C 102
5.10 Dose dependence of the RBS/C yield in the bulk defect peak region for AlN samples bombarded with 300 keV Au ions at −196 and 20 °C 104
5.11 Dark-field XTEM images of an AlN epilayer bombarded at 20 °C with 300 keV Au ions to a dose of 4×10^{16} cm^{-2} 105
5.12 Dark-field XTEM images of AlN epilayers bombarded at −196 °C with 300 keV Au ions to doses of 5×10^{15} and 3×10^{16} cm^{-2} 106

6.1 Typical continuous load–unload curves of as-grown, "ion-damaged," and amorphized GaN films 113
6.2 Typical amplitude-mode AFM images of as-grown and "ion-damaged" GaN films indented to a maximum load of 100 mN 113
6.3 Curves of the hardness and Young's modulus as a function of indenter penetration below the circle of contact. Figures show data for as-grown, "ion-damaged," and amorphized GaN 114
6.4 Partial load–unload curves of as-grown, "ion-damaged," and amorphized GaN films 116

7.1 CL spectra obtained at RT and LN_2 from virgin and implanted regions of GaN bombarded with 150 keV C ions at LN_2 to a dose of 10^{14} cm^{-2}. The inset illustrates the ion dose dependence of the intensities of near-gap and yellow luminescence peaks measured at RT from implanted parts of the samples relative to the corresponding CL intensities in the virgin parts of these samples 122

7.2 Near-gap and YL depth profiles obtained at RT from as-grown GaN 124

7.3 Near-gap and YL depth profiles obtained at RT from a GaN sample bombarded with 150 keV C ions at LN_2 to a dose of 5×10^{13} cm^{-2}. Shown are the depth profiles of the implanted GaN sample before and after postimplantation annealing at 1050°C for 15 s 125

7.4 Schematic diagram illustrating that CL emission measured from GaN implanted with keV ions is actually generated by the electron beam impinging on virgin GaN, beyond the implanted layer 126

7.5 CL spectra obtained at RT from as-grown GaN and GaN implanted with H, C, and O ions 127

7.6 CL spectra obtained at RT from GaN implanted with H, C, and O ions and subsequently annealed at 1050 °C for 15 s 131

7.7 Intensities of near-gap and YL peaks measured at RT from GaN samples implanted with H, C, and O ions, and subsequently annealed at 1050 °C for 15 s, as a function of electron beam current obtained with a finely focused electron beam 136

8.1 (a) Dose dependence of sheet resistance of GaN samples irradiated with 6.6 MeV ^{12}C ions. (b) Original free carrier concentration of the samples vs threshold doses 145

8.2 (a) Dose dependence of sheet resistance in identical samples for irradiation with different ions. (b) The estimated concentration of atomic displacements (N_d) is plotted vs threshold doses. 147

8.3 Dose dependence of sheet resistance of GaN samples irradiated with 6.6 MeV C ions at different temperatures 148

8.4 Dependencies of sheet electron density, effective Hall mobility, and sheet resistance on isochronal annealing temperature for a GaN sample implanted at RT with 0.6 MeV H ions to a dose of 2.4×10^{14} cm^{-2} 150

8.5 Dose dependence of sheet resistance of GaN samples irradiated with 6.6 MeV C ions at RT with different values of beam flux 151

8.6 Dose dependence of sheet resistance of GaN samples irradiated with 0.6 MeV H ions at RT with different values of beam flux 151

List of Tables

1.1 Some properties of III-nitrides 3

3.1 A summary of previous structural studies of implantation-produced damage in GaN 27

3.2 Implant conditions for which the effect of damage saturation in the crystal bulk has been observed 29

3.3 Implant conditions used in this study of structural disorder in GaN 30

6.1 Implant conditions used to prepare the "ion-damaged" sample by multiple-energy bombardment with ^{197}Au ions at 300 °C 111

6.2 Values of hardness and Young's modulus for the three GaN samples used in this study of mechanical properties 114

7.1 Free electron concentration and effective Hall mobility of the three GaN wafers used in sequential implantation experiments in optical studies 120

7.2 Implant conditions used to introduce C, O, and H species into GaN by sequential ion implantation at RT. Calculated values of projected ion ranges and the average number of lattice vacancies produced by one ion are also given 121

7.3 Intensities of near-gap and YL peaks obtained from samples cut from GaN wafers A, B, and C implanted with H, C, and O ions. 131

8.1 Original free electron concentration, effective Hall mobility, and sheet resistance of the three GaN wafers used in our study of electrical characteristics of ion-implanted GaN 143

Table of acronyms

ξ_{M_1}	the ratio of the level of lattice disorder measured to the damage level predicted
$\Phi_{0.3}$	the ion dose necessary to produce relative disorder of 0.3
Φ_{th}	the threshold ion dose for electrical isolation
AFM	atomic force microscopy
CL	cathodoluminescence
dpa	displacements per atom
DAP	donor–acceptor pair
E	Young's modulus
E_d	the effective threshold energy for atomic displacements
EPR	electron paramagnetic resonance
Ga_i	gallium interstitial
H	hardness
LN_2	liquid nitrogen temperature
NEC	National Electrostatics Corporation
N_i	nitrogen interstitial
RBS/C	Rutherford backscattering/channeling spectrometry
R_s	sheet resistance
RT	room temperature
RTA	rapid thermal annealing
SNICS	source of negative ions from cesium sputtering
TEM	transmission electron microscopy
V_{Ga}	gallium vacancy
V_N	nitrogen vacancy
XTEM	cross-sectional transmission electron microscopy
YL	yellow luminescence

Journal publications related to this thesis

1. S.O. Kucheyev, J.S. Williams, J. Zou, G. Li, C. Jagadish, M.O. Manasreh, M. Pophristic, S. Guo and I.T. Ferguson, "Structural disorder in ion-implanted $Al_xGa_{1-x}N$," *Applied Physics Letters* **80**(5): 787–789, 2002.

2. S.O. Kucheyev, J.S. Williams, C. Jagadish, J. Zou and G. Li, "Blistering of H-implanted GaN," *Journal of Applied Physics* **91**(6): 3928–3930, 2002.

3. S.O. Kucheyev, M. Toth, M.R. Phillips, J.S. Williams, C. Jagadish and G. Li, "X-ray spectrometry investigation of electrical isolation in GaN," *Journal of Applied Physics* **91**(6): 3940–3942, 2002.

4. S.O. Kucheyev, H. Boudinov, J.S. Williams, C. Jagadish and G. Li, "Effect of irradiation temperature and ion flux on electrical isolation of GaN," *Journal of Applied Physics* **91**(7): 4117–4120, 2002.

5. J.E. Bradby, S.O. Kucheyev, J.S. Williams, J. Wong-Leung, M.V. Swain, P. Munroe, G. Li, and M.R. Phillips, "Indentation-induced damage in GaN epilayers," *Applied Physics Letters* **80**(3): 383–385, 2002.

6. S.O. Kucheyev, J.S. Williams and S.J. Pearton, "Ion implantation into GaN," *Materials Science and Engineering, R, Reports: A Review Journal* **33**(2-3): 51–107, 2001.

7. S.O. Kucheyev, M. Toth, M.R. Phillips, J.S. Williams and C. Jagadish, "Effect of excitation density on cathodoluminescence from GaN," *Applied Physics Letters* **79**(14): 2154–2156, 2001.

8. S.O. Kucheyev, J.S. Williams, J. Zou, S.J. Pearton and Y. Nakagawa, "Implantation-produced structural damage in $In_xGa_{1-x}N$," *Applied Physics Letters* **79**(5): 602–604, 2001.

9. S.O. Kucheyev, J.S. Williams, A.I. Titov, G. Li and C. Jagadish, "Effect of the density of collision cascades on implantation damage in GaN," *Applied Physics Letters* **78**(18): 2694–2696, 2001.

10. S.O. Kucheyev, J.E. Bradby, J.S. Williams, C. Jagadish, M.V. Swain and G. Li, "Deformation behavior of ion-beam-modified GaN," *Applied Physics Letters* **78**(2): 156–158, 2001.

11. S.O. Kucheyev, M. Toth, M.R. Phillips, J.S. Williams, C. Jagadish and G. Li, "Cathodoluminescence depth profiling of ion-implanted GaN," *Applied Physics Letters* **78**(1): 34–36, 2001.

12. S.O. Kucheyev, J.S. Williams, J. Zou, C. Jagadish and G. Li, "Disordering and anomalous surface erosion of GaN during ion bombardment at elevated temperatures," *Applied Physics Letters* **78**(10): 1373–1375, 2001.

13. H. Boudinov, S.O. Kucheyev, J.S. Williams, C. Jagadish and G. Li, "Electrical isolation of GaN by MeV ion irradiation," *Applied Physics Letters* **78**(7): 943–945, 2001.

14. S.O. Kucheyev, J.S. Williams, J. Zou, J.E. Bradby, C. Jagadish and G. Li, "Ion-beam-induced reconstruction of amorphous GaN," *Physical Review B* **63**(11): 113202 (4 pages), 2001.

15. S.O. Kucheyev, J.S. Williams, C. Jagadish, J. Zou, G. Li and A.I. Titov, "Effect of ion species on the accumulation of ion-beam damage in GaN," *Physical Review B* **64**(3): 035202 (10 pages), 2001.

16. S.O. Kucheyev, J.S. Williams, J. Zou, C. Jagadish and G. Li, "The effects of ion mass, energy, dose, flux and irradiation temperature on implantation disorder in GaN," *Nuclear Instruments and Methods in Physics Research Section B* **178**: 209–213, 2001.

17. S.O. Kucheyev, J.S. Williams, J. Zou, C. Jagadish and G. Li, "High-dose ion implantation into GaN," *Nuclear Instruments and Methods in Physics Research Section B* **175-177**: 214–218, 2001.

18. S.O. Kucheyev, J.S. Williams, J. Zou, C. Jagadish and G. Li, "Ion-beam-induced dissociation and bubble formation in GaN," *Applied Physics Letters* **77**(22): 3577–3579, 2000.

19. S.O. Kucheyev, J.E. Bradby, J.S. Williams, C. Jagadish, M. Toth, M.R. Phillips, and M.V. Swain, "Nanoindentation of epitaxial GaN films," *Applied Physics Letters* **77**(21): 3373–3375, 2000.

20. S.O. Kucheyev, J.S. Williams, C. Jagadish, J. Zou, V.S.J. Craig and G. Li, "Ion-beam-induced porosity of GaN," *Applied Physics Letters* **77**(10): 1455–1457, 2000.

21. S.O. Kucheyev, J.S. Williams, C. Jagadish, G. Li and S.J. Pearton, "Strong surface disorder and loss of N produced by ion bombardment of GaN," *Applied Physics Letters* **76**(26): 3899–3901, 2000.

22. M. Toth, S.O. Kucheyev, J.S. Williams, C. Jagadish, M.R. Phillips and G. Li, "Imaging charge trap distributions in GaN using environmental scanning electron microscopy," *Applied Physics Letters* **77**(9): 1342–1344, 2000.

23. S.O. Kucheyev, J.S. Williams, C. Jagadish, J. Zou and G. Li, "Polycrystallization and surface erosion of amorphous GaN during elevated temperature ion bombardment," *Journal of Applied Physics* **88**(9): 5493–5495, 2000.

24. S.O. Kucheyev, J.S. Williams, C. Jagadish, J. Zou and G. Li, "Damage buildup in GaN under ion bombardment," *Physical Review B* **62**(11): 7510–7522, 2000.

25. S.O. Kucheyev, M. Toth, M.R. Phillips, J.S. Williams, C. Jagadish and G. Li, "Chemical origin of the yellow luminescence in GaN," *Journal of Applied Physics* (accepted for publication).

26. S.O. Kucheyev, J.S. Williams, J. Zou, G. Li, C. Jagadish and A.I. Titov, "Effect of ion species on implantation-produced disorder in GaN at liquid nitrogen temperature," *Nuclear Instruments and Methods in Physics Research Section B* (accepted for publication).

27. J.E. Bradby, J.S. Williams, J. Wong-Leung, S.O. Kucheyev, M.V. Swain, P. Munroe, and G. Li, "Spherical indentation of compound semiconductors," *Philosophical Magazine A* (accepted for publication).

28. M.R. Phillips, H. Telg, S.O. Kucheyev, O. Gelhausen and M. Toth, "Cathodoluminescence efficiency dependence on excitation density in *n*-type gallium nitride," *Microscopy and Microanalysis* (accepted for publication).

29. S.O. Kucheyev, J.S. Williams, J. Zou, C. Jagadish, M. Pophristic, S. Guo, I.T. Ferguson and M.O. Manasreh, "Ion-beam-produced damage and its stability in AlN films," *Journal of Applied Physics* (submitted).

Chapter 1

Introduction

1.1 Unique properties and applications of III-nitrides

For much of the past decade, group-III nitride semiconductors (GaN, InGaN, and AlGaN) have been a subject of extensive research due to very important technological applications of these materials. Current applications of III-nitrides include light-emitting diodes (LED's), laser diodes, UV detectors, and microwave power and ultra-high power switches. Below, we briefly discuss some of the unique material properties which make group-III-nitrides highly attractive for a range of (opto)electronic device applications. Extensive reviews on the growth and properties of III-nitrides can be found, for example, in Refs. [1–7] and will not be reproduced here.

At ambient conditions, the thermodynamically stable crystal structure of GaN, AlN, and InN is *wurtzite* [1–7]. The wurtzite structure consists of two inter-penetrating hexagonal close packed sublattices, each with one type of atoms (i.e., either Al/Ga/In or N), offset along the c-axis by 5/8 of the cell height. The space grouping of the wurtzite structure is $P6_3mc$ (C_{6v}^4). Although metastable zinc blende (cubic) GaN and InN can also be grown, they will not be considered in this thesis. Table 1.1 summarizes some basic properties of wurtzite III-nitride semiconductors at room temperature (RT).

The wurtzite polytypes of GaN, AlN, and InN form a continuous alloy system with direct RT band-gaps from 1.9 eV up to 6.2 eV (see Table 1.1), throughout much of the visible spectrum well into the ultraviolet wavelengths. This makes the III-nitride system extremely attractive for optoelectronic device applications.

Another very important application of III-nitrides is in high-temperature/high-power electronics. The interest here stems from the following properties of III-nitrides: (i) the wide band-gap nature of these materials, which makes the onset of pronounced thermally-induced intrinsic conductivity occur at much higher temperatures than in the case of mature semiconductors such as Si and GaAs, (ii) high breakdown electric field, and (iii) high saturation drift velocity of electrons.

1.2 Motivation

The excellent fundamental properties of III-nitrides make them ideal candidates for a range of (opto)electronic devices. However, a successful application of these materials for device fabrication requires a development of an appropriate device processing technology.

Table 1.1: Some properties of wurtzite III-nitrides at room temperature (after http://www.ioffe.rssi.ru/SVA/NSM/Semicond).

	Units	GaN	AlN	InN
Density	g/cm^3	6.15	3.23	6.81
Atomic density	10^{22} at./cm^3	8.9	9.6	6.4
Band gap	eV	3.4	6.2	1.9
Melting point	°C	~ 2500	3000	1100
Ionicity		0.500	0.499	0.578

Ion implantation represents a very attractive tool for several technological steps in the fabrication of group-III-nitride-based devices, such as (i) electrical and optical selective-area doping, (ii) dry etching, (iii) electrical isolation, (iv) quantum well intermixing, and (v) ion-cut (see, for example, recent reviews in Refs. [8–10]). However, bombardment with energetic ions inevitably produces lattice defects, which is often an undesirable side effect of ion-beam processing. It is well known that a successful application of ion implantation depends on understanding the production and annealing of radiation damage. Thus, detailed studies of ion implantation damage in III-nitrides are not only important for investigating fundamental defect processes in solids under ion bombardment but are also vital for the fast developing III-nitride industry.

A number of studies of selective-area electrical and optical doping of GaN by ion implantation have previously been reported in the literature [8–10]. Previous implantation studies have revealed that, unlike the situation for mature semiconductors such as Si and GaAs, GaN exhibits a rather complex behavior under ion bombardment. For example, previous attempts to achieve controllable n- and, in particular, p-type electrical doping by ion implantation have faced difficulties with rather low carrier mobility and low dopant activation efficiency, particularly in the case of high-dose ion implantation [8–10]. These problems have stemmed from an adverse influence of lattice defects produced by energetic ions. It has been shown that implantation-produced defects cannot be completely removed by thermal annealing even at rather high temperatures (as high as $1300 - 1400$ °C) [8–10].

Optical doping of GaN by implantation with optically-active ions (such as rare-earth ions) has also faced similar problems due to undesirable effects of ion-beam-produced lattice defects which act as very efficient non-radiative recombination centers and, hence,

essentially kill light emission from the optically-active species implanted [8–10].

By the late 1990's, it became evident that *systematic* studies of the evolution of lattice defects in GaN during ion bombardment as well as during postimplantation thermal annealing were needed for a successful application of ion implantation in the fabrication of GaN-based devices. Such a systematic study of ion-beam processes in GaN has been the subject of the present work.

It should also be noted that, in contrast to some progress with exploring the possibilities of ion implantation as a device processing tool in the GaN technology, prior to the work presented in this thesis, the structural characteristics of ion-implanted $Al_xGa_{1-x}N$ and $In_xGa_{1-x}N$ alloys had not been studied at all. This situation is somewhat surprising since AlGaN and InGaN are of great importance to the nitride technology because of their role as both active and cladding layers in optoelectronic devices [1–7]. Our study of ion-beam damage in AlGaN and InGaN, presented in this thesis, is crucial for the estimation and control of implantation-produced disorder in InGaN/GaN and AlGaN/GaN heterostructures.

Hence, the work presented in this thesis focuses on an understanding of the microstructure evolution of group-III-nitride semiconductors (GaN, AlGaN, and InGaN) exposed to ion bombardment. Specific objectives have been to understand the effect of ion irradiation on structural, mechanical, optical, and electrical properties of III-nitrides.

1.3 Thesis structure

This thesis has the following structure. The experimental techniques used in this work are briefly discussed in Chapter 2. For clarity, a literature review relevant to discussions in specific chapters has been included in the introductory sections, as well as in the main text, of each chapter. The behavior of the buildup of ion-beam-produced *structural* disorder in GaN is presented in Chapter 3. Intriguing effects of ion-beam-induced porosity in GaN and associated material decomposition are presented in Chapter 4. Chapter 5 is focused on the damage accumulation in AlGaN and InGaN epilayers. The influence of ion-irradiation-produced defects on mechanical, optical, and electrical properties of GaN is discussed in Chapters 6, 7, and 8, respectively. In Chapter 7, a study of the chemical origin of the notorious yellow luminescence in GaN is also presented. Finally, Chapter 9

highlights additional studies which are desirable for a better understanding of ion-beam processes in III-nitrides, essential for a successful application of ion implantation for the fabrication of III-nitride-based devices.

Chapter 2

Experimental

2.1 Samples

The samples used in this study were single-crystal wurtzite GaN epilayers grown on *c*-plane sapphire substrates by metalorganic chemical vapor deposition (MOCVD) in a rotating disk reactor at Ledex Corporation (Taiwan) by Dr. Gang Li. Typical growth conditions involved a low temperature GaN buffer layer followed by the growth of a GaN film at $\sim 1100 - 1150$ °C. The thickness of different GaN films was from ~ 1.8 to 4 μm, as measured by cross-sectional transmission electron microscopy (XTEM) or as specified by the grower. Only unintentionally doped GaN epilayers were studied, unless otherwise specified.

In addition to the information supplied by growers, the quality of GaN samples has been assessed by tapping-mode atomic force microscopy (AFM), cathodoluminescence (CL) spectroscopy, and Rutherford backscattering/channeling (RBS/C) spectrometry. Moreover, most of the samples have been studied by XTEM and Hall effect measurements. Results showed that these samples were of excellent quality. They exhibited a smooth surface (typically < 20 Å rms roughness for a 5×5 μm^2 scan), a small density of micro-pits (< 2 pits/mm^2 viewed with 200× magnification), a strong intensity of near-gap optical emission at room temperature (RT), and a concentration of threading dislocations of $< 10^8$ cm^{-2}, as revealed by TEM, which is typical for high quality GaN layers grown by MOCVD.

In addition to GaN samples, single-crystal epitaxial InGaN, AlGaN, and AlN films were used in this study. About 0.14-μm-thick $In_xGa_{1-x}N$ films ($x = 0.00$, 0.03, 0.07, 0.12, 0.16, 0.18, and 0.20, with $\Delta x = 0.01$, as measured by Rutherford backscattering) on the top of $\sim$ 2-μm-thick wurtzite undoped GaN epilayers were grown on *c*-plane sapphire substrates by MOCVD in a rotating disk reactor at Nichia Corporation (Japan). About 0.5-μm-thick $Al_xGa_{1-x}N$ films ($x = 0.00$, 0.05, 0.08, 0.10, 0.19, 0.40, and 0.60, with $\Delta x = 0.02$, as assessed by Rutherford backscattering and X-ray diffraction) on the top of $\sim$ 1-μm-thick wurtzite undoped GaN epilayers were grown on *c*-plane sapphire substrates by MOCVD in two different EMCORE reactors at Ledex Corporation (Taiwan) and at EMCORE Corporation (U.S.A.). About 0.2-μm-thick AlN films (with a concentration of Ga impurity of ≤ 1 at.% introduced during growth, as assessed by Rutherford backscattering) were grown on *c*-plane sapphire substrates by MOCVD in a rotating disk reactor at EMCORE Corporation. Our RBS/C and XTEM investigation showed that the quality of

these InGaN, AlGaN, and AlN epilayers was satisfactory for studies of ion-beam-produced structural disorder discussed in Chapter 5.

2.2 Experimental techniques

2.2.1 Introduction

The experimental techniques used in this work are ion implantation, RBS/C, XTEM, AFM, CL, spherical nanoindentation, and electrical measurements (sheet resistance and and Hall effect measurements). All these are mature, well understood experimental techniques. A detailed description of common experimental systems and the physical principles involved in these methods can be found in standard textbooks and monographs[1] and will not be reproduced here. Instead, this chapter focuses on a description of the basic physical principles of the techniques and specific features of the experimental systems used. A further description of experimental details relevant to specific chapters will be included in experimental parts, as well as in the main text, of each chapter.

2.2.2 Ion implantation

Concepts

In this section, we describe the main concepts of ion implantation which are relevant to this thesis. In ion implantation, targets (or samples) are irradiated with ionized atoms (i.e., ions) which are accelerated to energies usually from several keV up to several MeV. When such an energetic ion propagates through a solid, it looses its energy via interactions (i.e., collisions) with target nuclei and electrons. Such energy loss can result in displacements of atoms in the target, leaving lattice defects in crystalline solids.

Ion ranges and atomic displacements produced in III-nitrides by ion bombardment can be calculated using, for example, the TRIM (TRansport of Ions in Matter) code [22], a Monte Carlo computer simulation program. Other methods often used to calculate the profiles of implanted species and atoms displaced involve analytical calculations such as

[1] See, for example, Ref. [11] for ion implantation, Ref. [12] for RBS/C, Ref. [13] for XTEM, Refs. [14,15] for AFM, Ref. [16] for CL, Refs. [17–20] for nanoindentation, and Ref. [21] for electrical characterization techniques.

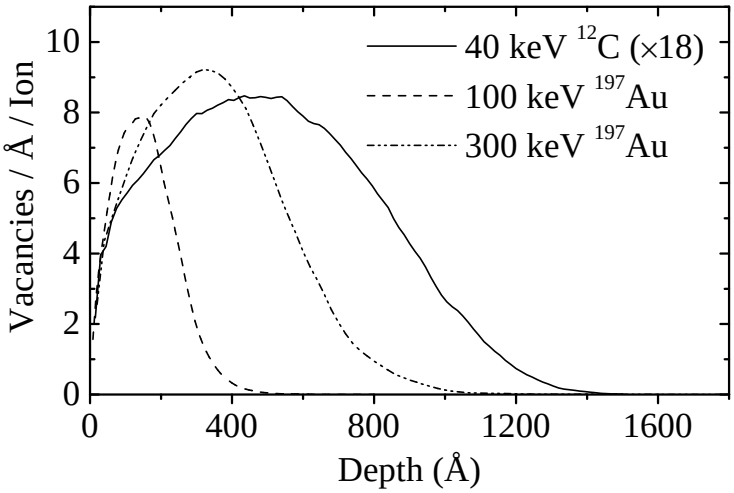

Figure 2.1: Profiles of vacancies produced in GaN by 40 keV ^{12}C, 100 keV ^{197}Au, and 300 keV ^{197}Au ions, as calculated using the TRIM code [22].

developed by Lindhard, Scharf, and Schiott [often called the LSS theory (see, for example, Ref. [23])] and an approach based on the Boltzmann transport equation [24].

In calculations of atomic displacements presented in this work using the TRIM code [22], the threshold displacement energy of atoms (E_d) was assumed to be 25 eV for both Ga and N sublattices in GaN. To our knowledge, no experimental studies to determine the value of E_d in GaN have been reported in the literature. TRIM simulations [22] show that the number of atomic displacements *nonlinearly* decreases with increasing E_d. However, qualitatively, the results presented in this work are independent of E_d since the dependence of the ratios of the number of atomic displacements produced by different ions on E_d is negligible for E_d values from 5 to 30 eV.

As an example, Fig. 2.1 shows profiles of vacancies produced in GaN by implantation with 40 keV ^{12}C, 100 keV ^{197}Au, and 300 keV ^{197}Au ions. It is seen from this figure that ion implantation produces skewed Gaussian-like (unimodal) profiles of atomic displacements. The thickness of the layer modified by ion bombardment as well as the number of atomic displacements generated depends on ion mass and energy, as illustrated in Fig. 2.1.

Such theoretical calculations of atomic displacements take into account only ballistic processes and completely neglect *dynamic annealing* (i.e., defect migration and interaction processes). However, ion-generated simple point defects, which survive after quenching of collision cascades, may migrate through the lattice and experience annihilation and cluster

formation. As a result, damage–depth profiles in GaN experimentally measured after ion bombardment may depart from predictions based only on collisional processes.

It is well known that complex dynamic annealing processes in solids under ion bombardment are highly dependent on implant conditions such as ion mass, energy, dose, substrate temperature, and beam flux (see, for example, Ref. [25]). In contrast to our ability to calculate atomic displacements in solids, stable lattice disorder produced by ion bombardment is usually difficult to predict. Experimental studies are essential to both determine and understand the effects of implant conditions on implantation disorder. Such studies are very important because lattice disorder strongly affects device performance.

Experimental details

All ion implantation experiments presented in this thesis were carried out with either the ANU 180 kV ion implanter (for implants with ion energies below 180 keV) or an ANU 1.7 MV tandem accelerator (National Electrostatics Corporation, U.S.A., model 5SDH-4). Figure 2.2 shows a schematic diagram of an ANU 1.7 MV tandem accelerator (NEC, 5SDH-4). The accelerator is equipped with a SNICS ion source (i.e., source of negative ions from cesium sputtering) [26, 27], which can produce a large variety of negative ion beams from solid cathode targets. In the SNICS, solid/liquid cesium is heated to form a vapor. The cesium vapor stream is ionized, forming positively charged cesium ions which are accelerated to the tip of a cathode. Cesium ions sputter the cathode material. In this study, we used elemental metal/semiconductor cathodes for implantation with Bi, Au, Ag, Cu, Si, C, and B ions. Pressed TiH_2 and Al_2O_3 powders were used as cathode materials to produce H and O ions, respectively. Sputtered atoms of the cathode are ionized and then accelerated through an aperture in the ionizer. The Einzel lens is used to focus the extracted beam.

The beam then passes through a pre-acceleration section, known as the source bias. Selection of the desired species is done with a 90° magnet. The bias voltage gives the beam energy sufficient to allow good species resolution by the magnet. The beam is delivered by the magnet to another Einzel lens and $x - y$ magnetic steerers for injection into the high voltage tank.

On entering the accelerator (the low energy end), the beam of negative ions is accelerated toward a positively charged terminal at the center of the accelerator tube. The

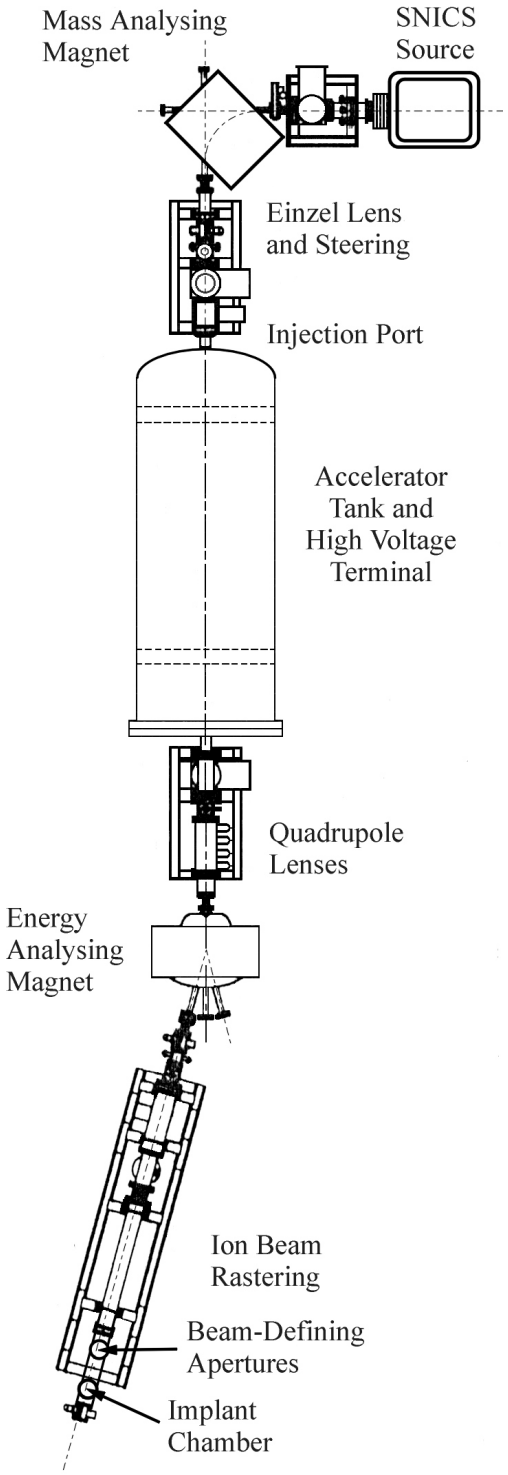

Figure 2.2: Schematic diagram of an ANU 1.7 MV tandem accelerator (NEC, 5SDH-4).

accelerator column surrounding the tube maintains an even voltage gradient up along the tube to the terminal. The terminal can hold a maximum charge of 1.7 MV. The charge is delivered to the terminal by two nylon chains containing steel pellets on each link (the so-called *pelletron* accelerator design).

At the terminal, electrons are stripped from the beam by the introduction of a small amount of nitrogen gas to the vacuum in the terminal space. Collisions between ion beam and nitrogen gas molecules produce neutral as well as single and multiply charged positive ions. The fast moving positively charged beam particles now see the ground potential at the far end of the accelerator (the high energy end) as a further attractive force and continue to be accelerated until their exit from the accelerator. The tank space surrounding the accelerator tube is filled with SF_6 gas for the electrical insulation of high voltage.

A 15° switching magnet is used to tune ions of the desired charge on to the target for implantation. The energy of the beam at the target is a function of the pre-acceleration stage (cathode, extractor, and bias voltages), the terminal voltage of the accelerator, and the charge of the ion selected by the switching magnet. A negative beam can be used for implantation by not stripping electrons from ions in the terminal. In this case, any gain in energy in the low energy end of the accelerator will be lost due to deceleration in the high energy end of the accelerator. As a result, negative ions will possess the injection energy.

A quadruple lens and further steering is employed to bring a suitably focused ion beam onto the target in the target chamber. The beam is then scanned across the target in a typical raster pattern up to the dose required for the particular experiment. The area on the target implanted is determined by a variable (tantalum metal) aperture at the entrance to the target chamber. The size of the aperture used in most of the implants discussed in this thesis was $\sim 1 \times 1$ cm^2. During implantation experiments discussed herein, vacuum in the target chamber was typically better than 5×10^{-7} torr. In addition to maintaining good vacuum, sample surface contamination with hydrocarbons during ion irradiation was minimized by maintaining a cylindrical Cu cold shield, surrounding the sample holder, at liquid nitrogen temperature (LN_2).

The target holders used in this study were made from Ni metal and designed to maintain temperature from LN_2 up to $\sim$ 600 °C. Sample temperature measurements were achieved using a K-type thermocouple embedded into the Ni target block. Samples were mounted on the Ni block using either steel clips or a conductive silver paste (so-called

"silver dag") to improve the thermal contact between the sample and the holder. Before implantation, samples were partly masked by a piece of a Si wafer. During implantation, samples were tilted by $\sim 7^\circ$ relative to the incident ion beam to minimize channeling.

The above description of the design and operation of the ANU 1.7 MV tandem accelerator shown in Fig. 2.2 also applies to the ANU 180 kV ion implanter used in this study. Indeed, this low energy (up to 180 kV) implanter has a very similar design from the ion source up to the injection port (see Fig. 2.2) and from the analyzing (15°) magnet to the target chamber. In contrast to the tandem accelerator shown in Fig. 2.2, the ANU 180 keV ion implanter does not have a high-voltage tank, quadruple lenses (necessary to focus high energy ion beams), and a switching magnet. This low energy implanter is used for implantation with negative ions of energies up to 180 keV.

2.2.3 Rutherford backscattering/channeling spectrometry

Concepts

The RBS/C technique [12] is based on collisions between atomic nuclei. It involves measuring the number and energy of ions which backscatter after colliding with atoms in the near-surface region of a sample being analyzed. With this information, it is possible to determine atomic mass and elemental concentrations in solids vs depth below the surface. The energy position of the surface peak for a particular element (determined by the so-called *kinematic factor*) can be precisely calculated taking into account scattering geometry, beam energy, and masses of the element and analyzing beam particles. RBS/C is ideally suited for determining the concentration of trace elements heavier than the major constituents of the substrate. The RBS random yield (i.e., surface spectrum height) can also be precisely calculated since it is directly proportional to the aerial density of the element and the scattering cross-section. In the case of Rutherford scattering (i.e., pure Coulomb scattering), which is a good approximation for conditions of the RBS/C experiments presented in this thesis, the scattering cross-section is $\sigma_R \propto (Z_1 Z_2/E)^2$, where Z_1 and Z_2 are atomic numbers of the analyzing particles and target atoms, respectively, and E is ion beam energy. Hence, the RBS yield increases with increasing Z_1 and Z_2 and with decreasing ion energy.

In addition to elemental composition information, RBS in combination with ion chan-

neling can be used to study the structure of single-crystal samples. For channeling, the rows of atoms in the lattice are aligned parallel to the incident analyzing ion beam. The analyzing beam will backscatter from the first few monolayers of the material at the same rate as in the case of a non-aligned sample, but backscattering from buried atoms in the crystalline lattice will be drastically reduced since these atoms are shielded from the incident ions by the atoms in the near-surface layers. The minimum normalized RBS/C yield (χ_{min}) can be calculated using, for example, the following equation [28]: $\chi_{min} = 18.8 n_{at} d u_1^2$, where n_{at} is atomic concentration, d is the atomic spacing along the axial channeling direction, and u_1 is the one dimensional vibrational amplitude. For example, for axial channeling along the c-axis of GaN, the above equation gives $\chi_{min} \cong 1\%$, indicating a *dramatic reduction* in the RBS/C yield compared to the random level. By measuring the reduction in backscattering when a sample is channeled, it is possible to *quantitatively* measure and *depth profile* the crystal perfection of a sample and to determine its crystal orientation.

As mentioned above, an important feature of the RBS/C technique is a depth profiling capability. This is achieved because the energy of backscattered particles is related to the depth in the sample where scattering occurred. Indeed, when analyzing beam particles (in this study, ^{4}He) move through a solid, they gradually lose energy mainly via interactions with target electrons since collisions with nuclei are rare (the probability for a particle to be backscattered into the detector is $\sim 10^{-5} - 10^{-6}$ for a typical geometry). A relation between the energy of backscattered particles and sample depth can be easily calculated taking into account the kinematic factor, ion stopping power, and the scattering geometry (determining the path which particles travel within the solid before and after backscattering events) [12]. It should be noted that ion stopping power and, hence, the depth scale in RBS/C spectra can be altered by compositional changes and ion channeling, as will be discussed in more detail in Chapter 3.

For a typical experimental geometry (with ~ 2 MeV He ions and a detector at $\sim 170°$ relative to the incident beam direction), the thickness of the near-surface layer analyzed is $\sim 1 - 2$ μm, with a depth resolution of ~ 300 Å close to the surface. However, the RBS/C depth resolution in the near-surface region can be improved by using a so-called glancing-angle detector geometry when a detector is placed at a small glancing angle (usually $\sim 3 - 25°$) relative to the sample surface. In this case, after experiencing backscattering,

ions travel a longer distance within the sample on the way to the detector, resulting in an increased energy loss and, hence, an improved depth resolution (typically of ~ 50 Å) in the near-surface region. Such a glancing-angle detector geometry has been used in the present work.

A more detailed discussion of the RBS/C technique can be found, for example, in Ref. [12] and will not be reproduced here. Below, we concentrate on specific features of the RBS/C machines used in the present study.

Experimental details

The RBS/C measurements presented in this thesis were done using either the ANU 2 MV Van de Graaff single-ended accelerator or an ANU 1.7 MV tandem accelerator (National Electrostatics Corporation, U.S.A., model 5SDH). The design of the latter accelerator, is similar to that of the ANU 1.7 MV tandem accelerator (NEC 5SDH-4), used for ion implantation and discussed in Sect. 2.2.2 (see Fig. 2.2). However, the accelerator used for the RBS/C analysis has a rubidium ion source (not a SNICS) and a high-voltage tank with only one nylon chain.[2]

The ANU 2 MV Van de Graaff single-ended accelerator used during the early stages of this work used a canvas and rubber belt to carry charge to the terminal. The ion source for this machine was an RF (radio frequency) source which was fixed onto the terminal. From the source, the ion beam was focused as it entered the accelerator tube and then accelerated to MeV energies before leaving the accelerator tank. After acceleration, the beam passed through a 25° switching magnet which was used to select the correct energetic particles. A long beam line ensured a well collimated beam (to better than 0.01°) at the chamber.

Below, we discuss the design of the beam line and the target chamber, which is common for both accelerators used for the RBS/C analysis in this thesis. An aperture box was used to place the correct sized beam diameter onto the center of the goniometer sample holder (with typically $\sim 50 - 80$ nA beam current with a beam spot of ~ 1 mm in diameter on the target). The sample holder had four degrees of freedom allowing a 25 mm translation in x and y directions and a 15° tilt about both x and y axes.

[2]One chain is sufficient since beam currents typically required for the RBS/C analysis are relatively low (typically < 100 nA) compared to beam currents used for high-dose ion implantation (typically $1 - 10$ μA).

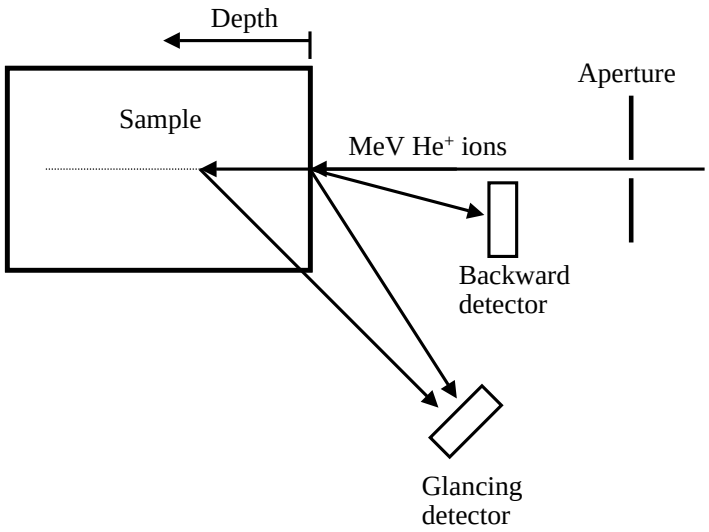

Figure 2.3: Schematic diagram illustrating detector geometry for RBS/C measurements.

A diagram schematically illustrating detector geometry is shown in Fig. 2.3. Two detectors are available in the chamber, one set for particles scattered (almost) back along the incident beam direction, and one for particles scattered at a glancing angle to the sample surface. The detectors are Au on Si surface barrier detectors with the output of each multiplexed into a computer for collection and analysis. In the present work, unless otherwise stated, the RBS/C analysis was done *ex-situ* at RT with 1.8 MeV $^4He^+$ ions incident along the [0001] direction of III-nitride films (which were typically better than $\pm 0.5^\circ$ *c*-axis oriented) and backscattered into detectors at $\sim 170^\circ$ and 98° relative to the incident beam direction. The latter glancing-angle detector was used to provide enhanced depth resolution (by increasing the exit path length of ions scattered from within the sample) when examining near-surface damage accumulation.

2.2.4 Transmission electron microscopy

Transmission electron microscopy is currently one of the most powerful techniques used to identify the nature of implantation-produced defects in semiconductors [13]. It can provide information about the crystallographic structure, composition, as well as types and (sometimes) concentrations of lattice defects. In this study, standard bright-field

and dark-field XTEM imaging conditions have been used. In this case, XTEM images are formed due to diffraction contrast (also called amplitude contrast). During imaging, samples are tilted so that diffraction from only one set of atomic planes is strong. In this case, there are only two strong spots in the selected-area diffraction pattern — the direct and diffracted beams (the so-called "two-beam condition"). By putting an objective aperture, only the diffracted beam (corresponding to electrons diffracted from only one set of crystal planes) can be selected to form the image. If this diffracted beam is chosen, a dark-field image is formed, in which sample regions at the Bragg condition appear bright. If the direct beam is chosen, a bright-field image is formed, in which regions of the crystal obeying the Bragg condition look dark. In addition, so-called weak-beam imaging can give improved resolution of defect structures in dark-field images by selecting a two-beam condition in which the diffracted beam is only weakly excited. A further description of the TEM technique can be found in standard textbooks (see, for example, an excellent description in Ref. [13]) and will not be reproduced here.

In this study, XTEM was performed with a commercial Philips CM12 transmission electron microscope operating at 120 keV. XTEM specimens were prepared by mechanical polishing followed by 3 keV Ar^+ ion beam thinning using a Gatan precision ion-polishing system.

2.2.5 Atomic force microscopy

The AFM technique can be used to study the surface morphology of semiconductors. AFM can be performed in contact, non-contact, and tapping modes. In contact-mode AFM, the tip scans the sample in close contact with the surface. The force on the tip is repulsive with a mean value of $\sim$ 1 nN. This force is set by pushing the cantilever against the sample surface with a piezoelectric positioning element. The deflection of the cantilever is sensed and compared in a DC feedback amplifier to some desired value of deflection. If the measured deflection is different from the desired value, the feedback amplifier applies a voltage to the piezo to raise or lower the sample relative to the cantilever to restore the desired value of deflection. The voltage that the feedback amplifier applies to the piezo is a measure of the height of features on the sample surface. It is displayed as a function of the lateral position of the sample.

Contact mode is the common mode used in the force microscope. However, this mode

of operation has several problems caused by excessive tracking forces applied by the probe to the sample, which can damage the sample and the tip. Moreover, under ambient conditions, sample surfaces are covered by a layer of adsorbed gases (typically $\sim 10 - 30$ monolayers thick) consisting primarily of water vapor and nitrogen. When the probe touches this contaminant layer, a meniscus forms, and the cantilever is pulled by surface tension toward the sample surface. These problems can be avoided by doing so-called tapping-mode AFM, which has been used in this study.

Tapping-mode AFM allows high resolution topographic imaging of sample surfaces that are easily damaged, loosely hold to their substrate, or difficult to image by other AFM techniques. Tapping mode overcomes problems associated with friction, adhesion, electrostatic forces, and other difficulties of contact-mode AFM by alternately placing the tip in contact with the surface to provide high resolution and then lifting the tip off the surface to avoid dragging the tip across the surface. Tapping-mode imaging is implemented in ambient air by oscillating the cantilever assembly at or near the cantilever's resonant frequency using a piezoelectric crystal. The piezo motion causes the cantilever to oscillate with a high amplitude (typically greater than 20 nm) when the tip is not in contact with the surface. The oscillating tip is then moved toward the surface until it begins to lightly touch (or tap) the surface. During scanning, the vertically oscillating tip alternately contacts the surface and lifts off, generally at a frequency of $50 - 500$ kHz. As the oscillating cantilever begins to intermittently contact the surface, the cantilever oscillation is reduced due to energy loss caused by the tip contacting the surface. The reduction in oscillation amplitude is used to identify and measure surface features. When the tip passes over a bump on the surface, the cantilever has less room to oscillate, and the amplitude of oscillation decreases. Conversely, when the tip passes over a divot, the cantilever has more room to oscillate, and the amplitude increases (approaching the maximum free air amplitude). The oscillation amplitude of the tip is measured by the detector and input to the controller electronics. The digital feedback loop then adjusts the tip-sample separation to maintain a constant amplitude and force on the sample.

Tapping mode inherently prevents the tip from sticking to the surface. Unlike contact mode, when the tip contacts the surface, it has sufficient oscillation amplitude to overcome the tip-sample adhesion forces. Also, the surface material is not pulled sideways by shear forces since the applied force is always vertical. Another advantage of the tapping-mode

AFM technique is its large, linear operating range. This makes the vertical feedback system highly stable, allowing routine reproducible sample measurements. A more detailed description of the AFM technique can be found, for example, in Refs. [14] and [15].

In this study, AFM measurements were performed under ambient conditions with a Digital Instruments Nanoscope III scanning probe microscope (which detection system is based on the beam-bounce optical method [14, 15]) in a tapping mode using commercial single-beam Si cantilevers with force constants of $30 - 120$ N m^{-1}. Amplitude-mode and height-mode AFM imaging conditions were used.

2.2.6 Cathodoluminescence spectroscopy

Cathodoluminescence spectroscopy (CL) is ideally suited to investigate, with high spatial resolution, optical properties of semiconductors. In CL measurements in a scanning electron microscope, a focused beam of electrons is scanned over the sample, and light emitted from the sample, excited by energetic electrons, is detected. Four common modes of CL analysis exist: CL spectroscopy, imaging, kinetics profiling, and depth profiling. In spectroscopy, CL intensity is detected as a function of light wavelength. In imaging, the electron beam is scanned over the sample, and CL emission is detected [either in a small spectral interval around a specific wavelength (monochromatic imaging) or for all wavelengths registered by the detector (panchromatic imaging)] as a function of electron beam position. Kinetics profiling employs measurements of CL intensity as a function of time. Finally, CL depth profiling involves CL intensity measurements as a function of electron beam energy (and, hence, as a function of the electron penetration range). Indeed, the electron penetration range increases with increasing beam energy. For example, a typical electron penetration range in GaN is ~ 0.2 μm for an electron energy of 5 keV and ~ 2 μm for a beam energy of 20 keV.

In semiconductors, CL is emitted as a result of electronic transitions between quantum mechanical states of different energy. Luminescence can be either intrinsic (due to recombination of electrons and holes across the band gap) or extrinsic (involving electronic levels of various impurities and lattice defects). A detailed description of the CL technique as well as optical processes in semiconductors can be found, for example, in Refs. [16, 29] and will not be reproduced here.

All CL measurements presented in this thesis were done with an Oxford Instruments

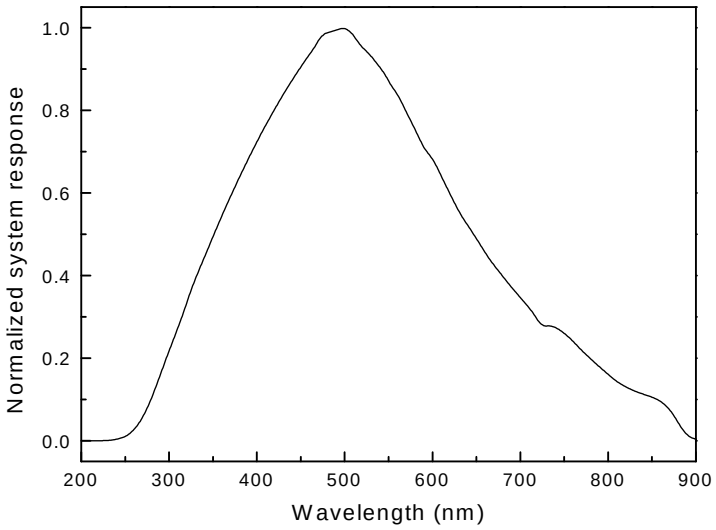

Figure 2.4: CL system response curve (courtesy of M. Toth).

MonoCL2 system installed on a JEOL 35C scanning electron microscope. The CL signal was collected using a paraboloidal mirror, dispersed by a 1200 lines/mm grating blazed at 500 nm, and detected using a Hamamatsu R943-02 peltier cooled photomultiplier tube. The RT band gap of GaN is $\sim$ 3.4 eV (corresponding to $\sim$ 366 nm), which is in the UV spectral region. Hence, to measure near-gap and deep-level-related emission, CL spectra were typically collected from $\sim$ 350 up to $\sim$ 800 nm. Cathodoluminescence spectra were corrected for system response using the curve shown in Figure 2.4. The JEOL 35C scanning electron microscope was also equipped with an Oxford Instruments liquid nitrogen cold stage, enabling CL measurements to be done at low temperatures. Additional details of CL measurements will be given in Chapter 7.

2.2.7 Nanoindentation

To study the mechanical properties of GaN, we have used continuous-depth-sensing indentation testing (generally known as nanoindentation) [17–20]. Nanoindentation is capable of providing information on a range of mechanical properties such as hardness and elastic properties and their variation continuously with indenter penetration depth. Such information can be readily obtained directly from force–displacement measurements. In addition, nanoindentation is ideal for monitoring the mechanical properties of very thin

films, which is the case of keV ion implantation when only a thin near-surface layer is modified by energetic ions. It is well known that, if the substrate is harder than the film, the substrate influence is usually negligible when the penetration depth of the indenter is less than $\sim 10\%$ of the film thickness (see, for example, Ref. [30]). Hence, nanoindentation appears to be an ideal technique to study ion-beam-modified GaN films grown on sapphire substrates (which are significantly harder than GaN).

In this study, nanoindentation experiments were done with an ANU UMIS-2000 nanoindentation system (designed and developed in CSIRO, Australia) with an ~ 4.2 μm radius spherical indenter. Because a knowledge of indenter geometry is important for data analysis and tip correction, the shape of the indenter tip was characterized by scanning electron microscopy. In addition, the indentation system and indenter tip were carefully calibrated by indenting fused silica of known mechanical properties.

During loading, both elastic (recoverable) and plastic (un-recoverable) deformation occurs under the indenter as the contact area changes with increasing depth. The unloading part of the force–displacement curve is usually dominated by elastic displacements. During the indentation process, an indenter is loaded onto the specimen with a known force (contact force). The indenter load is then increased by specified increments, while force and depth (or penetration) are measured independently at each step of the process. When the maximum force is reached, the indenter is unloaded by the same number of increments until zero load is registered on the indenter. From the measured load–unload curve, mechanical properties such as hardness and elastic modulus can be calculated. The type of nanoindentation measurements (i.e., continuous or partial load–unload measurements, discussed below), contact force, maximum force, and the number of increments are all user specified parameters.

There are two main regimes of indentation measurements — continuous and partial load–unload cycles. In the *continuous load–unload* cycle, the indenter is loaded from the contact force to the maximum force in a specified number of increments. The indenter is then unloaded to zero force by the same number of increments. At each load and unload step force and depth are measured. In the *partial load–unload* cycle, the indenter is loaded from the contact force to the maximum force, again, in a specified number of increments. At each step, however, force and depth are measured, and then the indenter is unloaded by a percentage of the force at that step. Force and depth are measured again. The indenter

force is then increased by the next increment. This partial load–unload continues until and including the maximum force. A more detailed description of nanoindentation can be found in Ref. [17–20] and will not be reproduced here.

In this study, a series of both partial and continuous load–unload indents was carried out at various maximum loads. All indents were performed at RT. The load–unload data was analyzed using the method of Field and Swain [31] to extract the hardness and elastic modulus as a function of indenter penetration. This is a standard method incorporated in the UMIS software.

2.2.8 Electrical characterization

The electrical characterization techniques used in this study are sheet resistance and Hall effects measurements. Both of these methods are well understood and developed experimental techniques. A detailed description of physical processes as well as related experimental systems can be found in Ref. [21] and will not be reproduced here.

Sheet resistance (R_s) is the resistance between opposite edges of a square of arbitrary dimensions. Sheet resistance is independent of the size of the square and is determined by material resistivity and sample thickness. Hence, R_s is a property of the sheet. For R_s measurements, rectangular samples ($\sim 5 \times 3$ mm^2) were cut from (two inch in diameter) GaN wafers. On two opposite sides of each sample, Ohmic contacts were fabricated, as illustrated in Fig. 2.5(a). Sheet resistance measurements of ion-bombarded GaN were done *in-situ* (without breaking vacuum in the target chamber of the implanter) with a specially designed sample holder. Measurements were performed several minutes after each ion dose had been delivered. In cases when electrical characterization was done at low or elevated temperatures, samples were brought to RT before each measurement.

For Hall effect measurements, the Van der Pauw method was used [21], with four Ohmic contacts in the corners of $\sim 5 \times 5$ mm^2 samples, as illustrated in Fig. 2.5(b). More details of Ohmic contact fabrication and electrical measurements will be given in Chapter 8.

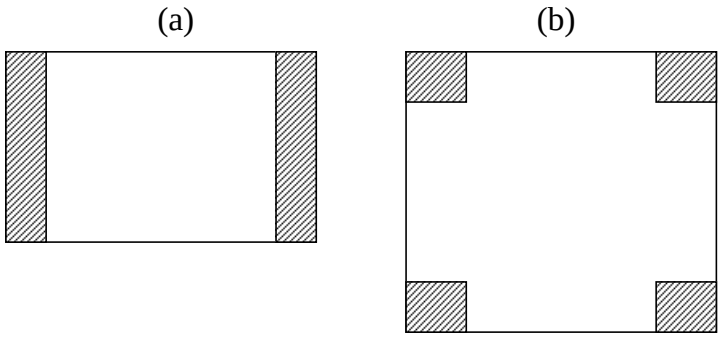

Figure 2.5: Schematic diagram of Ohmic contacts for sheet resistance (a) and Hall effect (b) measurements. Ohmic contacts are denoted by hatched areas.

2.2.9 Furnace annealing

Furnace annealing experiments presented in this thesis were carried out either in a rapid thermal annealing (RTA) system (AET-ADDAX RX) or in a conventional horizontal single-zone quartz tube furnace (Lindberg) under flowing argon or nitrogen gas. Special precautions (typical for semiconductor device processing) were made to ensure that the quartz tube (in the case of conventional furnace annealing) or the quartz liner (in the case of RTA anneals) used were clean. Annealing experiments were done in the proximity geometry, where samples are placed face-to-face in order to minimize material decomposition.

Chapter 3

Damage accumulation in GaN

3.1 Introduction

Lattice disorder is always a concomitant effect of ion bombardment. As discussed in Chapter 1, undesirable damage produced by an ion beam is, in fact, the main problem for satisfactory electrical and optical doping made by ion implantation. Dry etching is also always accompanied by undesirable damage introduced into near-surface layers. Therefore, studies of implantation disorder and its consequences are necessary for a successful application of ion implantation in device fabrication.

In this chapter, we discuss the buildup of *structural* damage (i.e., lattice damage as a function of ion dose) in wurtzite GaN under ion bombardment. A brief review of previous damage buildup studies in GaN is given in the next section. Section 3.3 presents experimental conditions of this study. Results are given in Sect. 3.4. In Sect. 3.5, based on our experimental data, we give a detailed discussion of various defect processes in GaN under ion bombardment. Finally, Sect. 3.6 presents a brief comparison of the damage buildup in GaN with that in other materials.

3.2 Previous damage buildup studies

The structural characteristics of semiconductors exposed to ion bombardment are usually studied by Rutherford backscattering/channeling (RBS/C) spectrometry, cross-sectional transmission electron microscopy (XTEM), and X-ray diffraction (XRD). Implantation-produced structural disorder in GaN has been studied by several groups [32–51], as summarized in Table 3.1. It is seen from this table that damage buildup has been studied for ions of different masses (from H to Au), for different ion energies, and at different implantation temperatures. However, no *systematic* studies of the effects of irradiation parameters on the defect accumulation in GaN had been carried out prior to the work presented in this thesis. For example, the effect of ion mass on the damage buildup in GaN has not previously been studied in any detail. Studies of the amorphization behavior with increasing ion dose have been reported only for bombardment of GaN with intermediate-mass ions such as Si [32,33], Ar [37], and Ca [37] ions at liquid nitrogen temperature (LN_2) and with relatively light O ions at -83 and -63 °C [44]. In addition, a rather detailed damage buildup study in GaN bombarded with heavy (Au) ions was done by Jiang et al. [45, 46] (see Table 3.1) simultaneously and independently from our damage buildup

studies presented in this thesis. In the following sections of this chapter, we discuss data by Jiang et al. [44–46] and compare it with our results.

Previous reports, summarized in Table 3.1, have unambiguously shown that GaN exhibits substantial *dynamic annealing* (i.e., defect migration and interaction) during ion bombardment even at LN_2. This conclusion directly follows from the fact that the amount of lattice disorder measured experimentally after ion irradiation is much less than that predicted by ballistic calculations (such as the TRIM code [22]), which take into account only collisional processes and neglect defect diffusion and annihilation. Defect migration, interaction, and agglomeration processes in GaN during ion bombardment are very efficient, resulting in a situation where most of ion-beam-generated defects experience effective annihilation.

In addition to the effect of ion mass/species, the effects of implantation temperature and beam flux on the buildup of structural disorder in GaN have not been systematically studied and, hence, not well understood. The effect of irradiation temperature on the damage accumulation in GaN has been studied in Refs. [35, 38, 39, 42, 46]. For example, Parikh et al. [35] studied, by RBS/C and XTEM, GaN bombarded with 120 keV Mg and 160 keV Si ions at 550 °C. Suvkhanov et al. [39] reported a RBS/C study of GaN bombarded at 700 °C with 100 keV Si and 80 keV Mg ions. Tan et al. [38] studied (by RBS/C) structural changes in GaN irradiated with 350 keV Te ions at temperatures from LN_2 up to 200 °C. A RBS/C study of GaN bombarded with 1 MeV Au ions (60° off the surface normal) at LN_2 and room temperature (RT) was reported by Jiang et al. [46]. Results from Refs. [35,38,39,46] have shown that, with increasing irradiation temperature, accumulation of stable defects and amorphization are suppressed.

However, an interesting and unexpected result has been reported by Wenzel et al. [42], who studied by RBS/C lattice disorder produced by a moderate dose of 90 keV Mg ions implanted into GaN at temperatures up to 550 °C. They have observed that lattice disorder in GaN bombarded with 90 keV Mg ions increases with increasing implantation temperature from RT up to 550 °C. In this chapter, we will discuss the effect of implantation temperature on the damage buildup behavior in GaN in more detail and show a somewhat similar effect of apparently increased damage produced at RT compared to LN_2 for light-ion (40 keV C) bombardment to low doses.

Wenzel et al. [42] have also reported that variation of beam flux (from 3.1×10^{12} to

Table 3.1: A summary of previous damage buildup studies (structural characteristics) in GaN. Note that the work done by the author of this thesis is not included in this table. For table entries marked with an asterisk, implantation was done 60° off the surface normal.

Ion	Energy (keV)	Implantation temperature (°C)	Ion dose (10^{14} cm^{-2})	Analysis	References
Si	90	–196	0.5 – 400	RBS/C, XTEM	[32, 33, 38]
Te	350	–196, 20, 200	10	RBS/C	[38]
Zn	200	20	0.5, 50	XTEM, XRD	[34]
Si	160	550	10	RBS/C, XTEM	[35]
Mg	120	20, 550	1, 5, 10	RBS/C	[35]
Ca	180	–196	0.0.5 – 60	RBS/C, XTEM, XRD	[36, 37]
Ar	180	–196	0.0.5 – 60	RBS/C, XTEM, XRD	[36, 37]
Mg	90	25, 300, 550	1 – 50	RBS/C	[41, 42]
Si	100	–196, 20, 700	0.01 – 70	RBS/C	[39]
Mg	80	–196, 20, 700	0.01 – 70	RBS/C	[39]
Mg	150	20	0.5	XRD	[40]
Be	200	20	5	XRD	[40]
O	600*	–83, –63	0.5 – 500	RBS/C	[44]
Au	1000*	–93, 20	0.4 – 50	RBS/C	[46]
Au	3000*	20	0.88 – 86	RBS/C	[45]
^{2}H	50	20	10 – 1000	RBS/C	[43]
Er	160	20	6, 60	RBS/C	[48]
Er	80	20, 450	4	RBS/C, XRD	[51]
Fe	150	20	10, 100	RBS/C, XRD	[49]
Ar	100	20	500	XTEM	[50]

1.3×10^{14} cm^{-2} s^{-1}) of 90 keV Mg ions implanted into GaN at RT has no effect on damage measured by RBS/C. Although this result seems to be somewhat surprising (at least the effects of beam heating could become pronounced for the largest beam flux used), it is consistent with the independence of implantation disorder on beam flux for light-ion (40 keV C) bombardment of GaN at RT discussed in Ref. [52]. In this chapter, we will discuss physical processes responsible for the flux effect and present our flux effect study for the case of heavy (Au) ion bombardment, where an interesting so-called *reverse flux effect* has been observed.

There was also an apparent discrepancy in the depth distribution of the damage buildup in GaN reported by different groups. For example, Tan et al. [32] showed that amorphization produced by 90 keV Si ions at LN_2 began from the surface, and the amorphous layer broadened gradually toward greater depths with increasing ion dose. On the other hand, Liu et al. [37], studying 180 keV Ca and Ar ion induced damage accumulation in GaN at LN_2, concluded that amorphization nucleated at a depth close to the projected ion range. In this chapter, we give a detailed discussion of the disorder depth profiles in ion-irradiated GaN, based on our RBS/C study with enhanced depth resolution.

Previous studies by Jiang et al. [44–46] (as well as by our group, as discussed below) have also revealed a rather interesting and unexpected effect in the damage buildup behavior of GaN — a saturation of bulk disorder. Jiang et al. [44–46] have shown that, with increasing ion dose, for implant conditions summarized in Table 3.2, ion-beam-produced disorder in the bulk region saturates below the random level (as measured by RBS/C). Such a saturation of bulk disorder suggests that the processes of defect production (by the ion beam) and removal (via defect annihilation and, presumably, expansion of the defect band) are balanced during ion irradiation. We will discuss this effect in more detail in this chapter.

The situation that so few detailed studies have been reported on the structural characterization of the disorder buildup in GaN under ion bombardment is somewhat surprising. Indeed, such studies often give an insight into the important properties of the defects produced by an ion beam. For example, information on the mobility and effective lifetimes of defects, defect clustering efficiency, and the influence of interfaces on mobile defects can often be obtained from an analysis of damage buildup under ion irradiation.

In this chapter, we present our systematic study of the influence of ion species (using

Table 3.2: Implant conditions for which the effect of damage saturation in the crystal bulk has been observed. All implants summarized in this table were done 60° off the surface normal.

Ion	Energy (keV)	Implantation temperature (°C)	Reference
^{16}O	600	−63	[44]
^{16}O	600	−83	[44]
^{197}Au	1000	20	[46]
^{197}Au	3000	20	[45]

a range of ion species from ^{1}H to ^{209}Bi) on the damage buildup behavior. We also discuss chemical effects of implanted species, which have not previously been considered for GaN. Such effects of enhanced damage accumulation and/or stabilization of an amorphous phase by implanted species dominate in the case of light ions, where large ion doses are needed to produce significant lattice disorder to study the damage buildup and amorphization behavior. Analyzing experimental data for ions of different masses and taking chemical effects into account, we give a detailed discussion the effect of the *density of collision cascades* on implantation-produced lattice defects.

3.3 Experimental

Implantation experiments presented in this chapter were carried out over a wide dose range under conditions indicated in Table 3.3. After implantation, samples were taken from the implanter chamber and characterized *ex-situ* at RT by RBS/C with 1.8 MeV ^{4}He^{+} ions incident along the [0001] direction and backscattered into a detector at 98° relative to the incident beam direction. This 8° glancing-angle detector geometry was used to provide enhanced depth resolution for examining near-surface damage accumulation. Selected samples were also studied by XTEM.

It should be noted that, in the case of low-temperature implantation experiments presented here, some thermal annealing of ion-beam-produced lattice damage may have occurred during warming the low-temperature-implanted samples up to RT before the subsequent RBS/C or XTEM analysis. For example, such an effective RT annealing of

Table 3.3: Implant conditions used in this study of structural disorder in GaN. Calculated values of the average number of lattice vacancies produced by one ion (N_{vac}^{tot}) and the number of vacancies in the maximum of the nuclear energy deposition profile (N_{vac}^{max}) are also given. Ballistic calculations were done with the TRIM code [22].

Ion	Energy (keV)	Implantation temperature (°C)	Beam flux (10^{12} cm^{-2} s^{-1})	N_{vac}^{tot}	N_{vac}^{max} (vac/ion/Å)
$^{1}H^{-}$	10	–196	11	5	1.7×10^{-3}
$^{12}C^{-}$	40	–196, 20	14	236	0.23
$^{16}O^{-}$	50	–196, 20	19	338	0.36
$^{28}Si^{-}$	60	–196, 20	16	479	0.88
$^{63}Cu^{-}$	130	–196, 20	9.4	1240	2.18
$^{107}Ag^{+}$	200	–196, 20	0.6	1976	3.4
$^{197}Au^{+}$	300	–196	3.1	2956	5.7
$^{197}Au^{+}$	300	20	4.4	2956	5.7
$^{209}Bi^{+}$	500	–196, 20	∼0.1	4646	5.9

lattice damage produced by low-temperature bombardment has been found to occur in SiC (see, for example, Ref. [53]). However, in contrast to this situation in SiC, one might not expect a pronounced thermal annealing at RT of implantation-produced disorder in GaN. Indeed, due to very efficient dynamic annealing, which occurs in GaN even at LN_2, a large part of ion-beam-generated point defects exhibits annihilation, and only more stable (energetically favorable) defect structures form in the lattice and effectively accumulate with increasing ion dose. Moreover, our assumption in this work that the complex defect structures produced by ion bombardment at low temperatures will be thermally stable during annealing up to RT is supported by previous *in-situ* RBS/C studies by Jiang et al. [44–46]. These authors have shown that no detectable recovery of damage produced in GaN by bombardment with ^{16}O or ^{197}Au ions at ~ -90 °C occurs as a result of prolonged annealing at RT. However, additional experimental work (such as *in-situ* RBS/C studies) is clearly desirable to study a possible RT thermal recovery of damage produced in GaN by ion bombardment at LN_2.

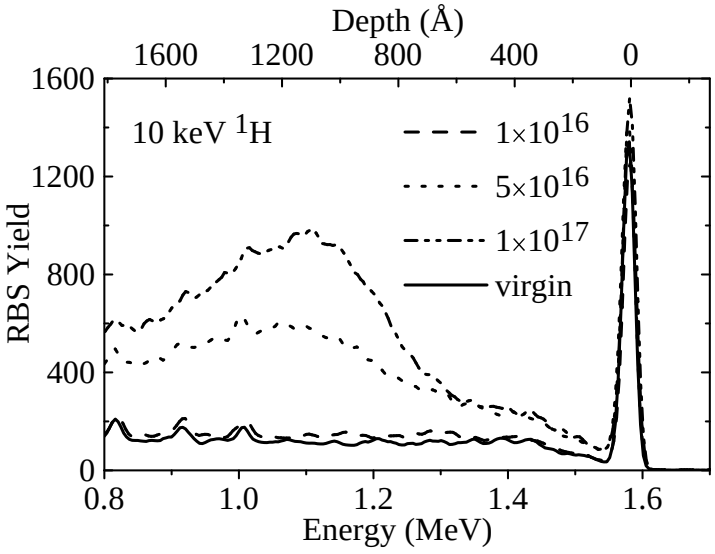

Figure 3.1: RBS/C spectra showing the damage buildup for 10 keV H ion bombardment of GaN at LN_2 with a beam flux of 1.1×10^{13} cm^{-2} s^{-1}. Implantation doses (in cm^{-2}) are indicated in the figure. The random yield corresponds to $\sim$ 5200 counts.

3.4 Results

In order to understand the evolution of implantation-produced defect structures in GaN, we have studied the influence of implant conditions on the damage buildup. Results presented below show that the damage buildup behavior in GaN strongly depends on ion species. Hence, we present data for each species separately.

3.4.1 Hydrogen

For completeness, we discuss the damage buildup in GaN starting with results for the lightest possible ions — hydrogen ions. However, as shown below, due to extremely efficient dynamic annealing processes in GaN, damage accumulation studies using RBS/C are difficult in this case of very light ions because extremely large H doses are required to produce disorder levels detectable by RBS/C.

Indeed, Fig. 3.1 shows that the accumulation of implantation-produced lattice disorder in GaN during bombardment with 10 keV H ions at -196 °C becomes evident from RBS/C spectra only for rather large ion doses ($\geq 1\times10^{16}$ cm^{-2}). This is a direct consequence of very efficient dynamic annealing processes in GaN. However, for such large doses of chemically active species which can also form gas bubbles, the small direct scattering

peak seen in Fig. 3.1 for doses of 5×10^{16} and 1×10^{17} cm^{-2} may have a contribution from chemical effects of implanted H atoms as well as from a band of H_2 gas bubbles,[1] in addition to implantation-produced lattice defects. In favor of such a scenario is the fact that the maximum of the bulk RBS/C peak seen in Fig. 3.1 is at $\sim$ 1100 Å. This is closer to the projected range of 10 keV ^{1}H ions ($\sim$ 1000 Å) rather than the maximum of the nuclear energy loss profile of these ions ($\sim$ 910 Å).[2] It is also seen from Fig. 3.1 that even the largest dose bombardment (1×10^{17} cm^{-2} of 10 keV H ions) results in only a slight increase in the magnitude of the surface defect peak, which reflects surface disordering. Hence, in the case of very light ^{1}H ions, damage accumulation studies using RBS/C are not possible in GaN bombarded even at LN_2 and with low ion energies (such as 10 keV) because extremely large ion doses are needed to produce lattice disorder to levels detectable by RBS/C. For such large ion doses, the chemical effects of H and the formation of H_2 gas bubbles hinder studies of lattice disorder. Therefore, we will not further discuss data from Fig. 3.1 in the following analysis of the damage buildup in GaN.

3.4.2 Carbon

Figure 3.2 shows RBS/C spectra that illustrate the damage buildup in GaN with increasing dose of 40 keV C ions implanted with a beam flux of 1.4×10^{13} cm^{-2} s^{-1} at LN_2 [Fig. 3.2(a)] and RT [Fig. 3.2(b)]. A number of features of these spectra, which show damage in the Ga sublattice, are of interest. First, the distorted shape of the RBS/C spectra for GaN implanted to high doses ($> 2 \times 10^{16}$ cm^{-2}) is a result of excessively high C accumulation that may lead to the formation of a $C_xGa_yN_z$ alloy with increasing dose of C ions [12]. This effect is also illustrated in Fig. 3.3, which shows that, with increasing ion dose, the aligned RBS/C spectra exhibit a complex behavior with a general trend of a *reduction* in the yield for high doses ($> 5 \times 10^{16}$ cm^{-2}). It is interesting that, relative to the energy scale, the

[1] For studies on the formation of hydrogen gas bubbles in H-implanted GaN, see, for example, Refs. [43, 54].

[2] It should be noted that the difference in the depth scales of random and aligned spectra (i.e., the difference in the energy loss of analyzing alpha-particles for random and channeling directions) can not be the reason for such a shift in the position of the bulk RBS/C peak relative to the maximum of the nuclear energy loss profile. Indeed, such a difference in the depth scales results in an apparent shift of the RBS/C peaks closer to the surface (i.e., to higher energies). This is just the opposite direction of the shift observed in Fig. 3.1.

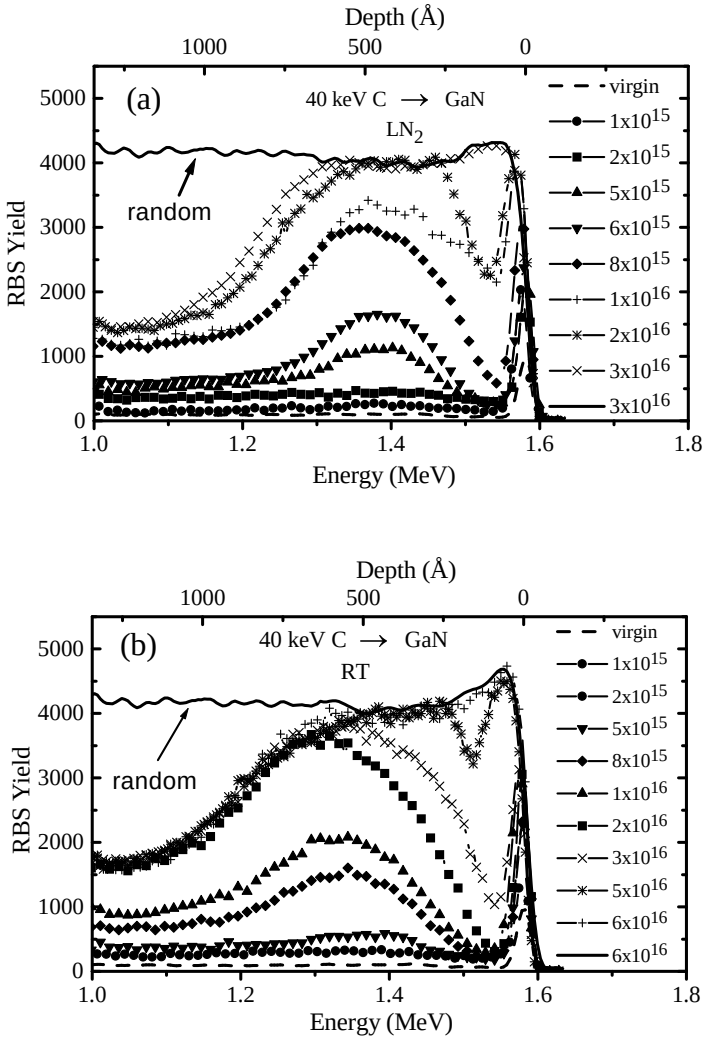

Figure 3.2: RBS/C spectra showing the damage buildup for 40 keV C ion bombardment of GaN at LN_2 (a) and RT (b) with a beam flux of 1.4×10^{13} cm^{-2} s^{-1}. Implantation doses (in cm^{-2}) are indicated in the figure.

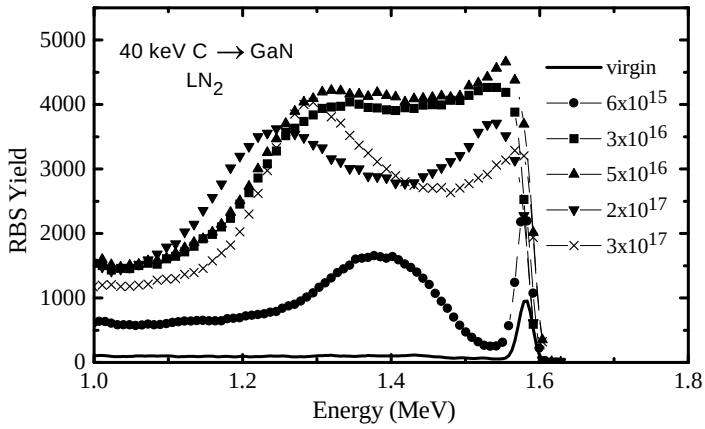

Figure 3.3: RBS/C spectra of GaN implanted to high doses with 40 keV C ions at LN_2 with a beam flux of 1.4×10^{13} cm^{-2} s^{-1}. Implantation doses (in cm^{-2}) are indicated in the figure.

depth scale also changes with increasing dose due to the changes in the energy loss of the analyzing 1.8 MeV He^+ ions. Such a complex behavior is a result of introduction into the GaN lattice of a high concentration of ^{12}C atoms, which are much lighter than ^{70}Ga. As will be discussed below, the preferential loss of nitrogen during high dose ion bombardment also influences the RBS/C yield in the near-surface region. Figure 3.3 clearly illustrates a potential difficulty of studying amorphization in GaN under light-ion bombardment when very high doses are required for amorphization.

Also seen from Fig. 3.2 is an apparent small shift of the maximum of the bulk defect peak to lower backscattering energies with increasing level of lattice disorder. This shift has been attributed to the difference in the energy loss of analyzing 1.8 MeV He^+ ions incident along channeling and random directions [55]. It should be noted that the depth scales in the RBS/C spectra presented in this thesis have been calculated with the stopping powers of Ga and N in an amorphous matrix. Therefore, the depth scales should be more accurate for the spectra with high damage levels, where the error resulting from the different stopping power in a channeling direction should be small. This has been discussed in more detail elsewhere [55].

Another feature seen from Fig. 3.2 is that an increase in implantation temperature from LN_2 to RT appreciably reduces implantation damage. Although this trend is not

unexpected, the magnitude of the temperature effect on postimplantation damage is of more interest. The results from Fig. 3.2 do not indicate a very strong effect of temperature on the gross amount of postimplantation disorder in GaN under irradiation with 40 keV C ions.

The next important feature from Fig. 3.2 is that the shape of the damage profiles measured significantly departs from a Gaussian-like defect profile expected based on ballistic calculations such as the TRIM code [22] (see Fig. 2.1). Two peaks in the experimental damage distribution are clearly seen, corresponding to surface and bulk peaks of disorder. The bulk peak close to the depth of the maximum nuclear energy loss ($\sim$ 500 Å) is not unexpected. However, an unusually strong surface peak of disorder in GaN bombarded with 40 keV C ions is somewhat surprising. This effect is discussed in more detail in Sect. 3.5.5.

Figure 3.4 shows dark-field XTEM images taken from GaN implanted with 40 keV C ions with a beam flux of 1.4×10^{13} cm^{-2} s^{-1} to a dose of 8×10^{15} cm^{-2} at LN_2. The RBS/C spectrum of the same sample is shown by diamonds in Fig. 3.2(a). The XTEM micrograph shown in Fig. 3.4(a) ($\mathbf{g} = 0002^*$) indicates the presence of point defect clusters in the implanted region (up to $\sim$ 900 Å from the GaN surface). In addition, the image with $\mathbf{g} = 1\bar{1}00^*$ shown in Fig. 3.4(b) reveals some planar defects present in the bulk defect peak region. These planar defects are parallel to the basal plane of the GaN film. Although the region between bulk and surface defect peaks is relatively free from planar defects [see Fig. 3.4(b)], a small concentration of point defect clusters is present in this region, as indicated by Fig. 3.4(a). Therefore, this XTEM data is in good agreement with the damage depth profile measured by RBS/C [Fig. 3.2(a)].

Selected samples have been studied by XTEM with the electron beam precisely parallel to the GaN surface to eliminate edge effects on the contrast of the near-surface region. Figure 3.5(a) shows such a bright-field image of the same sample depicted in Fig. 3.4. A thin layer of amorphous material on the GaN surface is clearly seen. This layer has a different contrast to that of the glue (on the sample surface) and of crystalline GaN. Our XTEM investigation by switching between bright-field imaging and dark-field imaging indicates that this layer is amorphous. This finding is also consistent with the RBS/C yield reaching the random level at the surface, as measured with the glancing-angle detector geometry. For comparison, Fig. 3.5(b) shows a bright-field micrograph of a sample implanted with

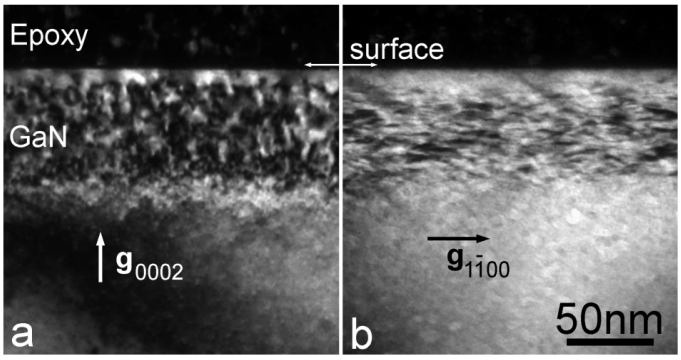

Figure 3.4: Dark-field XTEM images [(a) $\mathbf{g} = 0002^*$ and (b) $\mathbf{g} = 1\bar{1}00^*$] of the GaN epilayers bombarded at LN_2 with 40 keV C ions with a beam flux of 1.4×10^{13} cm^{-2} s^{-1} to a dose of 8×10^{15} cm^{-2}.

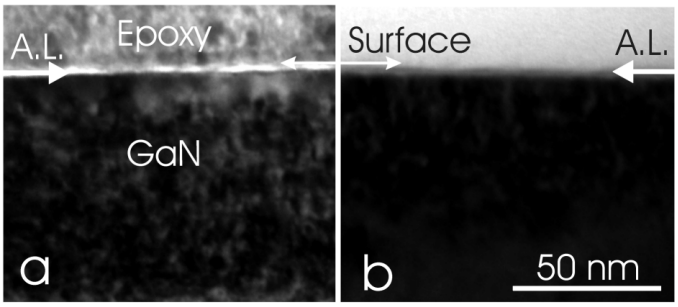

Figure 3.5: (a) Bright-field XTEM image taken from the same GaN sample depicted in Fig. 3.4. (b) Bright-field XTEM image of GaN implanted at LN_2 with 100 keV Au ions with a beam flux of 1.4×10^{13} cm^{-2} s^{-1} to a dose of 3×10^{14} cm^{-2}. Amorphous layers (labeled as A.L.) on the GaN surface are clearly demonstrated.

heavy (Au) ions, which will be discussed in Sect. 3.4.5.

Figure 3.6 shows $\mathbf{g} = 0002^*$ (with $\mathbf{g}/6.1\mathbf{g}$ imaging condition) weak-beam XTEM images taken from samples implanted with 40 keV C ions with a beam flux of $1.4{\times}10^{13}$ cm^{-2} s^{-1} to a dose of 1×10^{15} cm^{-2} at LN_2 [Fig. 3.6(a)] and RT [Fig. 3.6(b)]. Figure 3.6 indicates that, for such a low dose implantation (1×10^{15} cm^{-2}),[3] RT bombardment produces a similar type of residual damage to irradiation at LN_2. In addition, a comparison of RBS/C spectra of these two samples [see Figs. 3.2(a) and 3.2(b)] suggests a higher damage level in the RT implanted sample, whereby the RBS/C yield of the sample implanted at RT is higher than that of the sample bombarded at LN_2 to the same dose of 1×10^{15} cm^{-2}. This interesting result may be qualitatively explained based on the fact that an increase in implantation

[3]Note that we consider the value of ion dose to be low or high based on the level of lattice disorder produced.

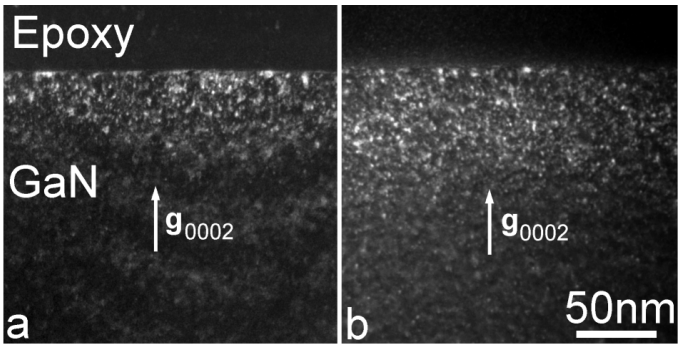

Figure 3.6: Weak-beam XTEM images ($\mathbf{g} = 0002^*$ with $\mathbf{g}/6.1\mathbf{g}$ imaging condition) of the GaN epilayers bombarded with 40 keV C ions with a beam flux of 1.4×10^{13} cm^{-2} s^{-1} to a dose of 1×10^{15} cm^{-2} at LN_2 (a) and RT (b).

temperature leads to an increase in the rate of all thermally activated point defect processes (defect diffusion, direct and indirect annihilation, formation of complexes, trapping of free defects by defect complexes and impurities, etc.). The nature of stable defect complexes formed at RT during dynamic annealing may, as a consequence, result in a higher level of residual disorder. However, at present, further experimental work is necessary to identify the most plausible mechanism for the this somewhat odd temperature-dependent effect.

Figure 3.7 shows the magnitudes of the surface and bulk defect peaks, taken from Fig. 3.2, as a function of the dose of 40 keV C ions implanted at LN_2 and RT. The peak levels have been normalized to the random level for each dose to take into account the effect of high dose implantation on the random yield. It is clearly seen from Fig. 3.7 that the damage buildup in GaN is highly sigmodal for the case of light-ion bombardment. This behavior is consistent with previous results of LN_2 bombardment of GaN with light ions (O [44]), intermediate-mass ions (Si [32, 33], Ar [37], and Ca [37]), and heavy ions (^{197}Au [46]). Such a sigmodality represents a characteristic feature of a nucleation-limited damage buildup, as discussed in more detail below.

A confirmation of amorphization suggested by RBS/C in the case of C ions is given by the bright-field XTEM image shown in Fig. 3.8(a), which reveals the presence of two amorphous layers (buried and surface layers labeled as "X") in GaN bombarded at LN_2 with 40 keV C ions to a dose of 2×10^{16} cm^{-2}. In addition, Fig. 3.8(b) shows a bright-field image of GaN bombarded at RT with 40 keV C ions to a dose of 5×10^{16} cm^{-2}. It is seen from Fig. 3.8(b) that both bulk and surface amorphization (with the formation of surface

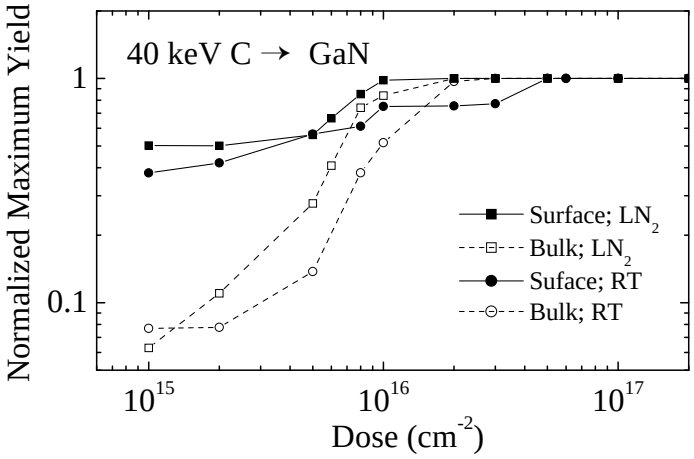

Figure 3.7: Dose dependence of the magnitudes of the bulk and surface defect peaks for 40 keV C ion bombardment at LN_2 and RT with a beam flux of 1.4×10^{13} cm^{-2} s^{-1}. The peak levels have been normalized to the random level.

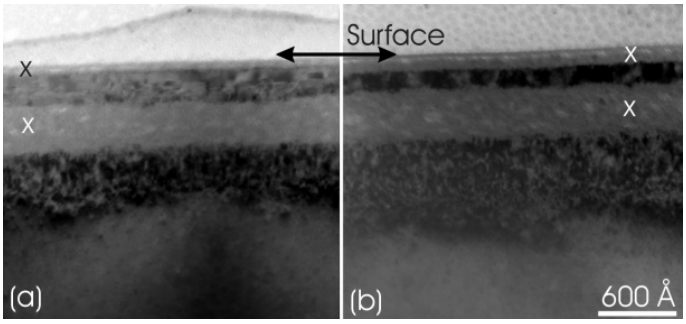

Figure 3.8: Bright-field XTEM images of GaN bombarded with 40 keV C ions with a beam flux of $\sim 1.4 \times 10^{13}$ cm^{-2} s^{-1} at LN_2 (a) and RT (b) to doses of 2×10^{16} (a) and 5×10^{16} cm^{-2} (b). Images (a) and (b) are of the same magnification. The formation of buried and surface amorphous layers (labeled as "X") is demonstrated.

and buried amorphous layers labeled as "X") also occurs in GaN bombarded with C ions at RT.

A comparison of Fig. 3.2(a) and 3.2(b) also reveals an increased (presumably trap-limited) defect mobility in GaN at RT compared to LN_2, resulting in an apparent shift of the maximum of the bulk defect peak (to greater depths) with increasing implantation temperature. For example, the damage peak at LN_2 for a dose of 8×10^{15} cm^{-2} is close to $\sim$ 470 Å, but the depth of the damage peak for a dose of 2×10^{16} cm^{-2} at RT is near $\sim$ 620

Å, as shown in Figs. 3.2(a) and 3.2(b). Such a behavior has previously been observed for elevated temperature bombardment of Si, where disorder is found to buildup beyond the maximum of the nuclear energy deposition distribution at so-called end-of-range defects (see, for example, Ref. [56]). These end-of-range defects in Si consist of interstitial-based clusters and small loops which arise from the well known spatial separation of vacancies and interstitials in a collision cascade, with an interstitial excess at the ion end-of-range and a vacancy excess closer to the surface. In Si, under strong dynamic annealing conditions (i.e., at elevated temperatures), mobile defects are preferentially trapped at the surface or in the end-of-range region where the interstitial excess coalesces. A somewhat similar explanation might be proposed for the RT behavior observed in GaN. Strong defect annihilation and increased defect mobility may lead to a dominant trapping of defects both at the surface and at the end-of-range for 40 keV C ions implanted into GaN. However, we cannot exclude the role of carbon (i.e., trapping of point defects by carbon atoms) in this process since the carbon dose is very high during damage buildup at RT. Such chemical effects of C and other species will be discussed in detail in Sect. 3.5.6.

3.4.3 Oxygen

Figure 3.9(a) shows that the main features of the damage buildup behavior during bombardment of GaN with 50 keV O ions at -196 °C are similar to those for bombardment with 40 keV C ions discussed in the previous section. Indeed, as is seen from Fig. 3.9(a), damage accumulation at -196 °C is bimodal with a strong surface defect peak in addition to the bulk peak of disorder close to the maximum of the nuclear energy loss profile. In this case, the damage buildup is sigmodal with ion dose, again consistent with results for C-implantation (Sect. 3.4.2), where an amorphous phase nucleates both at the surface and in the bulk. Such a structure with surface and bulk amorphous layers is shown in Fig. 3.10, illustrating the formation of a buried amorphous layer (labeled as "X") in GaN bombarded at LN_2 with 50 keV O ions to a dose of 6×10^{16} cm^{-2}, as also confirmed by our XTEM investigation by switching between bright-field and dark-field imaging. Hence, RBS/C data on amorphization is in good agreement with XTEM results. With increasing ion dose, these two amorphous layers (in the bulk and at the surface) expand until they meet each other, resulting in a relatively thick, continuous surface layer of an amorphous material. Also note that the $\mathbf{g} = 1\bar{1}00^*$ XTEM image shown in Fig. 3.10(b) illustrates the

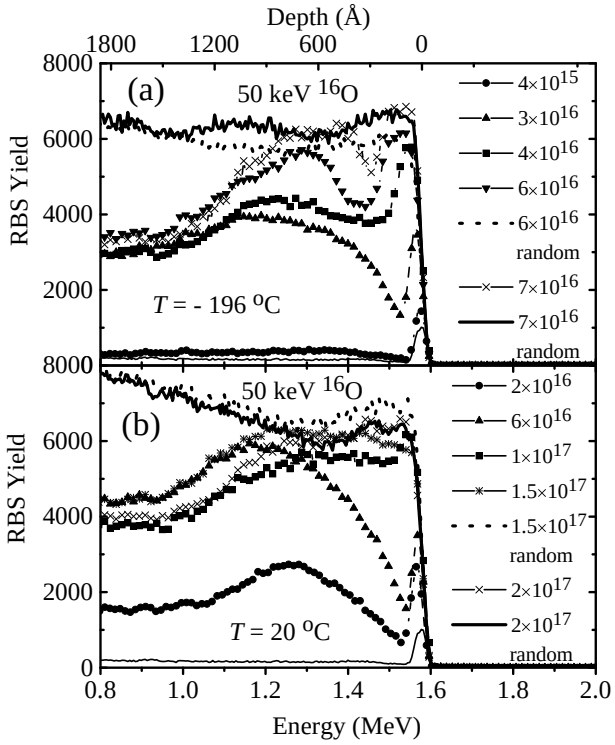

Figure 3.9: RBS/C spectra showing the damage buildup for 50 keV O ion bombardment of GaN at LN_2 (a) and RT (b) with a beam flux of 1.9×10^{13} cm^{-2} s^{-1}. Implantation doses (in cm^{-2}) are indicated in the figure. A virgin spectrum is also shown for comparison.

formation of extended (planar) defects in GaN bombarded to high ion doses, which will be discussed in more detail in Sect. 3.5.3.

Figure 3.9(b) illustrates the damage buildup for bombardment of GaN with 50 keV O ions at 20 °C. It is seen that, again similar to the situation for ^{12}C discussed above, damage accumulation is bimodal. However, in contrast to the case of 40 keV C ion bombardment at RT [see Fig. 3.2(b)], implantation with O ions at 20 °C does not appear to result in bulk amorphization. Instead, bulk disorder saturates at a level ($\sim$ 85% of random) which is, however, much higher than the saturation level for the case of bombardment with heavier ions discussed in the following sections.

Similar to the situation for ^{1}H and and ^{12}C (discussed above), the study of the damage buildup in GaN exposed to implantation with ^{16}O ions is complicated by the fact that ion doses necessary to amorphize GaN with these ions are extremely large even in the case of bombardment at LN_2. This is clearly illustrated in Figs. 3.9(a) and 3.9(b), where, for large

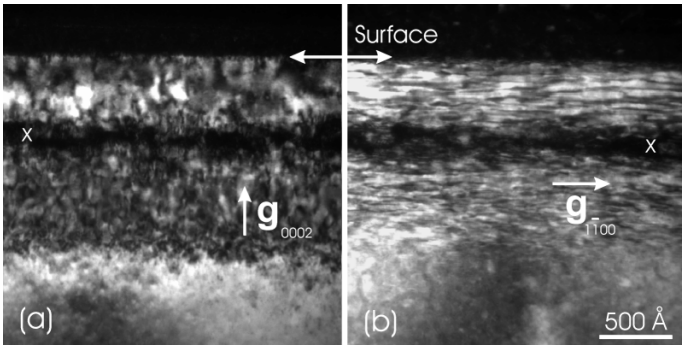

Figure 3.10: Dark-field XTEM images [(a) $\mathbf{g} = 0002^*$ and (b) $\mathbf{g} = 1\bar{1}00^*$] of GaN bombarded at LN_2 with 50 keV O ions with a beam flux of 1.9×10^{13} cm^{-2} s^{-1} to a dose of 6×10^{16} cm^{-2}. Images (a) and (b) are of the same magnification. The formation of a buried amorphous layer (labeled as "X") is demonstrated.

ion doses, both channeling and random spectra are given. It is seen from Figs. 3.9(a) and 3.9(b) that the height (and the shape) of random spectra changes with increasing ion dose above $\sim 5 \times 10^{16}$ cm^{-2}, which corresponds to several at.% of O atoms implanted into the GaN matrix. Moreover, relative to the energy scale, the depth scale in RBS/C spectra also changes with increasing ion dose due to the changes in the energy losses of the analyzing alpha-particles as oxygen concentration increases. In the case of such high ion doses, a quantitative estimation of the concentration vs depth profiles of implantation-produced lattice disorder from RBS/C spectra becomes a rather challenging problem.

3.4.4 Intermediate-mass ions: ^{28}Si, ^{63}Cu, and ^{107}Ag

Shown in Figs. 3.11 – 3.14 are RBS/C spectra illustrating the buildup of lattice disorder in GaN implanted with 60 keV ^{28}Si, 60 keV ^{63}Cu, and 200 keV ^{107}Ag ions at LN_2 [Fig. 3.11] and RT (Figs. 3.12, 3.13, and 3.14). It is seen that, for all these cases of intermediate-mass ions both at LN_2 and RT, the behavior of damage buildup with increasing ion dose is qualitatively similar to that observed by Jiang et al. [46] for heavy-ion (^{197}Au) bombardment at RT. Indeed, Figs. 3.11 – 3.14 illustrate a bimodal damage buildup with evidence for defect saturation rather than amorphization in the crystal bulk for high ion doses. In this case, amorphization proceeds layer-by-layer only from the surface with increasing ion dose, as confirmed by XTEM. It is interesting that, similar to bombardment with ^{16}O ions discussed above, the bulk damage level attained at high doses of ^{28}Si ions

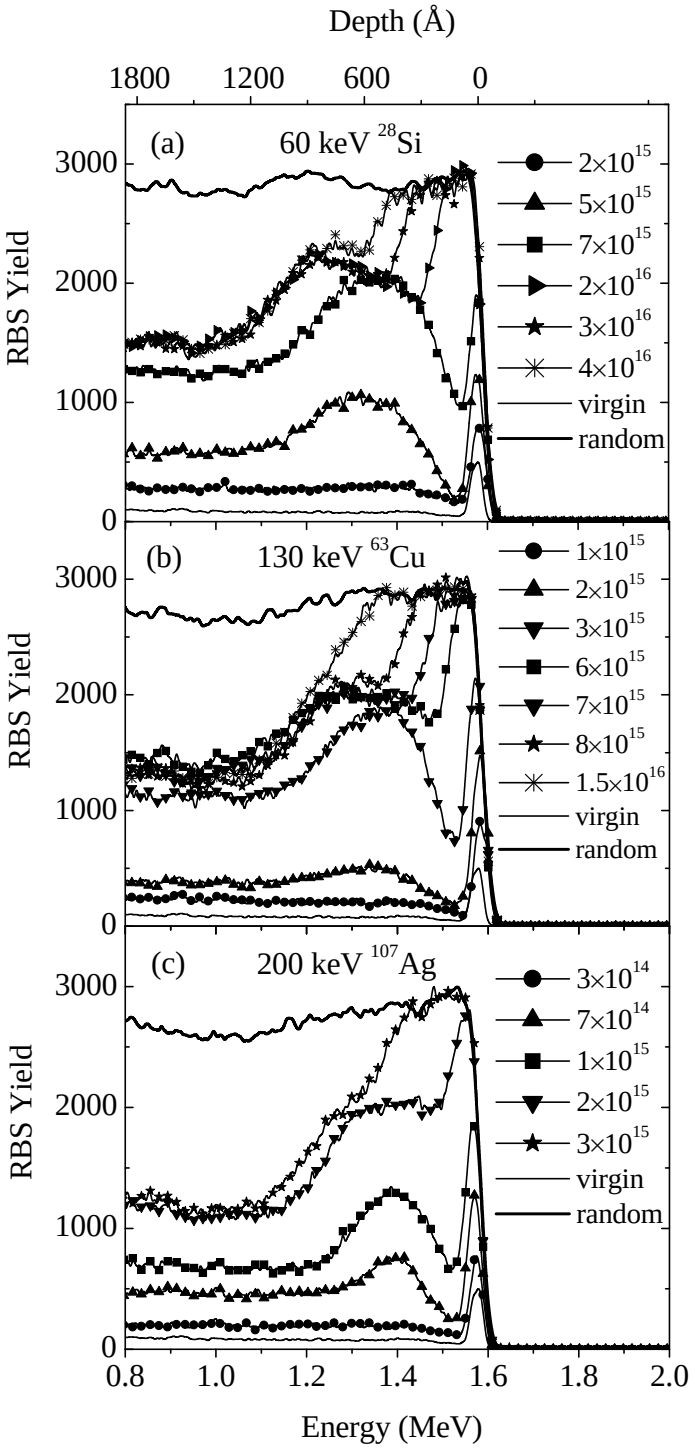

Figure 3.11: RBS/C spectra showing the damage buildup in GaN bombarded at LN_2 with 60 keV Si ions with a beam flux of 1.6×10^{13} cm^{-2} s^{-1} (a), with 130 keV Cu ions with a beam flux of 9.4×10^{12} cm^{-2} s^{-1} (b), and with 200 keV Ag ions with a beam flux of $\sim 6\times10^{11}$ cm^{-2} s^{-1} (c). Implantation doses (in cm^{-2}) are indicated in the figure.

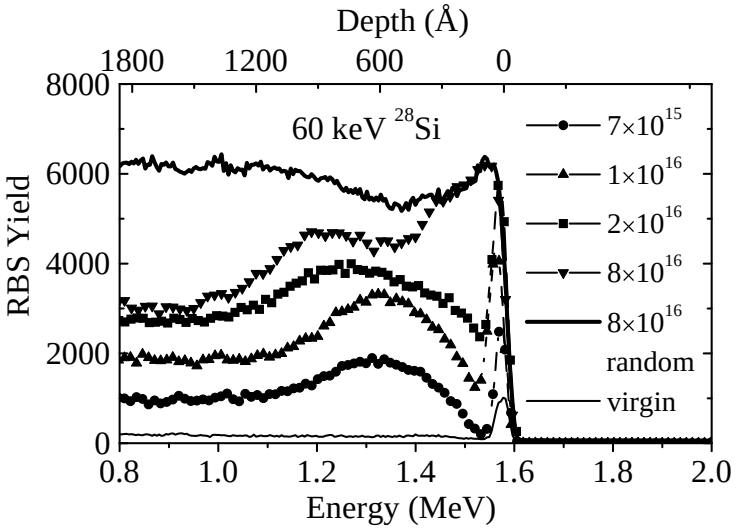

Figure 3.12: RBS/C spectra showing the damage buildup for 60 keV Si ion bombardment of GaN at RT with a beam flux of 1.6×10^{13} cm^{-2} s^{-1}. Implantation doses (in cm^{-2}) are indicated in the figure.

[see Figs. 3.12 and 3.11(a)] is larger than the saturation level of damage in the case of irradiation with Cu and Ag ions, as well as with Au ions discussed in Ref. [46] and below. In addition, due to the fact that relatively large Si ion doses are required for amorphization of GaN even at LN_2 ($\geq 5 \times 10^{16}$ cm^{-2}), the chemical effects of implanted Si atoms may also affect the damage buildup, as will be discussed more fully in Sect. 3.5.6. Such a large concentration of implanted Si atoms (with, presumably, precipitation of Si) is also responsible for a large dip in the RBS/C random spectrum (around $\sim$ 500 Å) shown in Fig. 3.12 in the case of a dose of 8×10^{16} cm^{-2} at RT.

Figure 3.15 shows dark-field images of GaN bombarded at RT with 60 keV Si ions to a dose of 2×10^{16} cm^{-2}. These images indicate the presence of point defect clusters [see the $\mathbf{g} = 0002^*$ image in Fig. 3.15(a)] and planar defects [see the $\mathbf{g} = 1\bar{1}00^*$ image in Fig. 3.15(b)] in the near-surface region damaged by ion bombardment ($\sim$ 1500 Å from the GaN surface). The sample from Fig. 3.15 (bombarded with Si ions) has also been studied by XTEM with the electron beam precisely parallel to the GaN surface to minimize edge effects on the contrast of the near-surface region. This study reveals the presence of a thin surface amorphous layer that is $\sim$ 40-Å-thick, which is consistent with the strong surface defect peak seen from the RBS/C spectrum shown in Fig. 3.12. We will discuss the formation of such surface amorphous layers in more detail in Sects. 3.5.5.

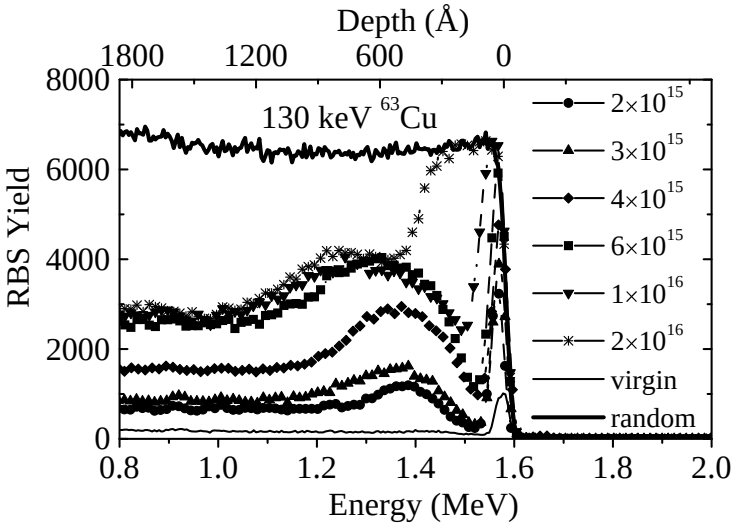

Figure 3.13: RBS/C spectra showing the damage buildup for 130 keV Cu ion bombardment of GaN at RT with a beam flux of 9.4 × 10^{12} cm^{-2} s^{-1}. Implantation doses (in cm^{-2}) are indicated in the figure.

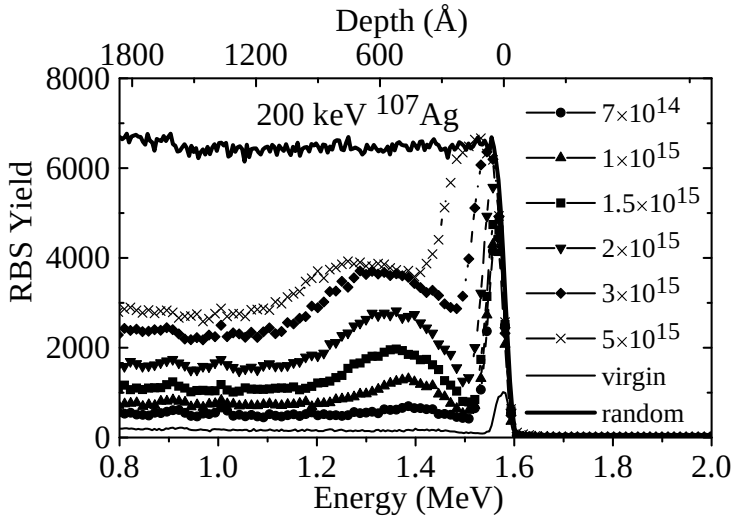

Figure 3.14: RBS/C spectra showing the damage buildup for 200 keV Ag ion bombardment of GaN at RT with a beam flux of 6 × 10^{11} cm^{-2} s^{-1}. Implantation doses (in cm^{-2}) are indicated in the figure.

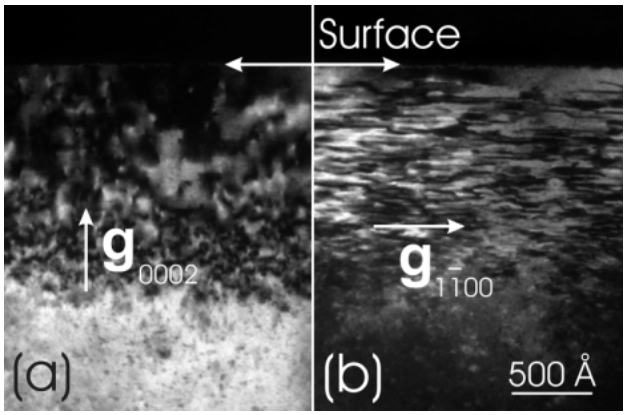

Figure 3.15: Dark-field XTEM images [(a) $\mathbf{g} = 0002^*$ and (b) $\mathbf{g} = 1\bar{1}00^*$] of the GaN epilayers bombarded at RT with 60 keV Si ions with a beam flux of 1.6×10^{13} cm^{-2} s^{-1} to a dose of 2×10^{16} cm^{-2}.

3.4.5 Heavy ions: ^{197}Au and ^{209}Bi

In this section, we discuss the damage buildup behavior in GaN under heavy-ion bombardment. Although a rather detailed discussion is given for the case of Au ions, the main features of the damage accumulation behavior are similar for both cases of Au and Bi ion bombardment regimes.

Bombardment with 100 keV Au ions

Figure 3.16 shows RBS/C spectra that illustrate the damage buildup in GaN with increasing dose of 100 keV Au ions implanted with a beam flux of 1.4×10^{13} cm^{-2} s^{-1} at LN_2 [Fig. 3.16(a)] and RT [Fig. 3.16(b)]. A comparison of Figs. 3.16(a) and 3.16(b) reveals quite different damage buildup behavior with increasing the dose of 100 keV Au ions for LN_2 and RT bombardment regimes. Indeed, for LN_2 irradiation, for doses up to $\sim 2 \times 10^{14}$ cm^{-2}, Fig. 3.16(a) shows accumulation of damage preferentially at the GaN surface, away from the maximum of the nuclear energy loss profile. Then, in the dose range from $\sim 2 \times 10^{14}$ to 4×10^{14} cm^{-2}, damage in the GaN bulk region ($\sim$ 150 Å from the GaN surface) exhibits a very rapid increase from a very low level to apparent amorphization, as indicated by the RBS/C yield reaching the random level. This rapid disorder buildup results in a strong sigmodality of the damage–dose function, as discussed in more detail below. In contrast to LN_2, bombardment at RT does not result in such a fast growth of damage in the bulk region with increasing ion dose [see Fig. 3.16(b)]. Instead, damage in

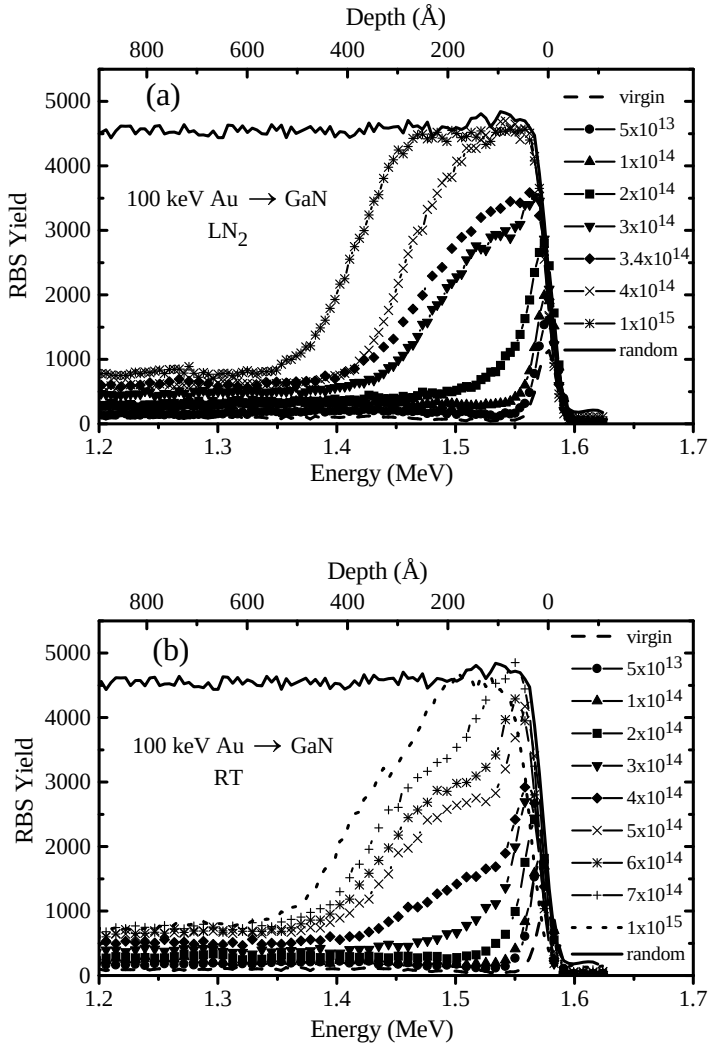

Figure 3.16: RBS/C spectra showing the damage buildup for 100 keV Au ion bombardment of GaN at LN_2 (a) and RT (b) with a beam flux of 1.4×10^{13} cm^{-2} s^{-1}. Implantation doses (in cm^{-2}) are indicated in the figure.

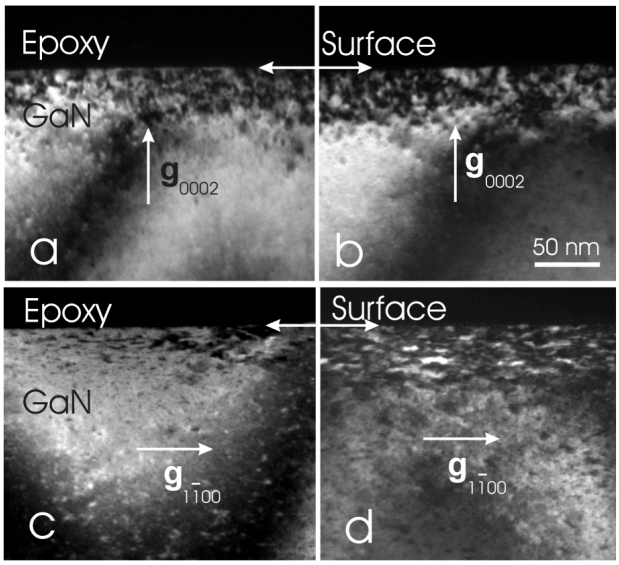

Figure 3.17: Dark-field XTEM images [(a,b) $\mathbf{g} = 0002^*$ and (c,d) $\mathbf{g} = 1\bar{1}00^*$] of the GaN epilayers bombarded with 100 keV Au ions with a beam flux of 1.4×10^{13} cm^{-2} s^{-1} to doses of 2×10^{14} cm^{-2} (a,c) and 3×10^{14} cm^{-2} (b,d) at LN_2.

the bulk region saturates below the random level, and amorphization appears to proceed layer-by-layer from the GaN surface, as indicated by RBS/C spectra shown in Fig. 3.16(b). Hence, the damage buildup behavior of GaN under RT heavy ion bombardment is similar to that during irradiation with intermediate-mass ions (Si, Cu, and Ag) at LN_2 and RT, discussed in detail in Sect. 3.4.4.

Figure 3.17 shows dark-field XTEM images taken from GaN implanted with 100 keV Au ions with a beam flux of 1.4×10^{13} cm^{-2} s^{-1} to doses of 2×10^{14} [Figs. 3.17(a,c)] and 3×10^{14} cm^{-2} [Figs. 3.17(b,d)] at LN_2. Images taken under the $\mathbf{g} = 0002^*$ condition [Figs. 3.17(a,b)] indicate the presence of point defect clusters in the implanted regions (up to $\sim$ 300 Å from the GaN surface), while images taken under the $\mathbf{g} = 1\bar{1}00^*$ condition [Figs. 3.17(c,d)] reveal some planar defects. The concentration of these planar defects, which are parallel to the basal plane of the GaN film, increases with increasing ion dose, as seen from a comparison of Figs. 3.17(c) and 3.17(d). A similar band of planar defects has been observed in GaN bombarded with light C, O, and Si ions discussed in previous sections.

Shown previously in Fig. 3.5(b) is a bright-field XTEM image taken from the GaN sample shown in Figs. 3.17(b,d). This image was taken under the same conditions as

the image from Fig. 3.5(a). The similarity between these two images for light and heavy ions is clear. Both exhibit thin surface amorphous layers and defect clusters in the bulk. This result suggests that ion bombardment with both light and heavy ions leads to the formation of a thin amorphous layer on the GaN surface. However, for 100 keV Au ion bombardment, the entire damage profile is too shallow for the bulk defect peak and a thin amorphous layer to be separated in the RBS/C spectra, even for the glancing-angle detector geometry used in this study. Therefore, a higher energy of gold ions has been used, as presented below.

Bombardment with 300 keV Au ions

Shown in Fig. 3.18 are RBS/C spectra illustrating damage accumulation in GaN with a dose of 300 keV Au ions implanted at LN_2 [Fig. 3.18(a)] and at RT [Fig. 3.18(b)]. Compared to 100 keV Au bombardment, in this case the RBS/C depth resolution is sufficient for the bulk and surface peaks of disorder to be separated in the spectra. A comparison of Figs. 3.16 and 3.18 shows that the main features of damage buildup behavior do not change upon increasing the energy of Au ions from 100 to 300 keV. One can see the same highly sigmodal damage buildup for LN_2 bombardment [Fig. 3.18(a)] and a pronounced effect of damage saturation in the bulk region for implantation at RT [Fig. 3.18(b)]. These effects are also illustrated in Fig. 3.19, which shows the magnitudes of the surface and bulk defect peaks (taken from Fig. 3.18) as a function of the dose of 300 keV Au ions implanted at LN_2 and RT.

It should be noted that the magnitudes of the surface defect peaks relative to the random level depend on the geometry of RBS/C measurements. For example, it is seen from Fig. 3.18(a), which shows RBS/C spectra measured with 8° glancing-angle detector geometry, that the surface peak of a sample implanted with 300 keV Au ions at LN_2 to a dose of 3×10^{14} cm^{-2} is below the random level. However, the surface peak of the same sample reaches the random level when measured by RBS/C with about 3° glancing-angle detector geometry (not shown here) to provide a better depth resolution in the near-surface region. This result (obtained also for other selected samples) as well as XTEM data (see Fig. 3.5) suggests that the strong surface peak in RBS/C spectra arises from a thin amorphous layer on the GaN surface.

Figure 3.20 shows XTEM images [(a,c,e) $\mathbf{g} = 0002^*$ and (b,d,f) $\mathbf{g} = 1\bar{1}00^*$] taken

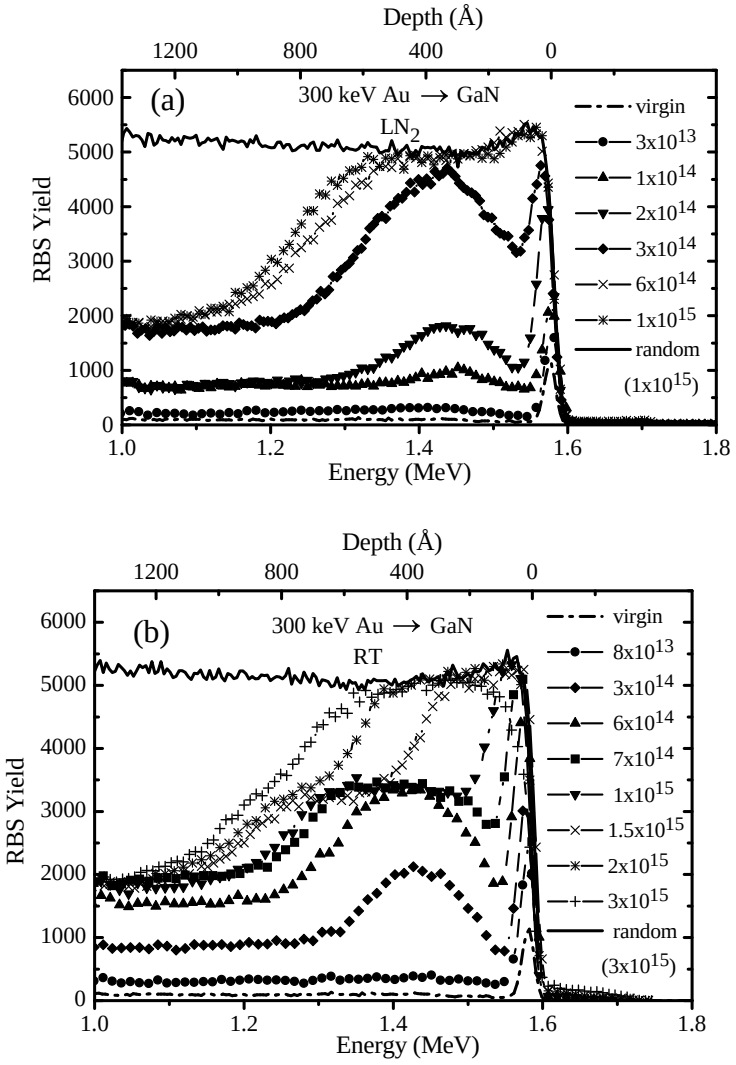

Figure 3.18: RBS/C spectra showing the damage buildup for 300 keV Au ion bombardment of GaN at LN_2 with a beam flux of 3.1×10^{12} cm^{-2} s^{-1} (a) and at RT with a beam flux of 4.4×10^{12} cm^{-2} s^{-1} (b). Implantation doses (in cm^{-2}) are indicated in the figure.

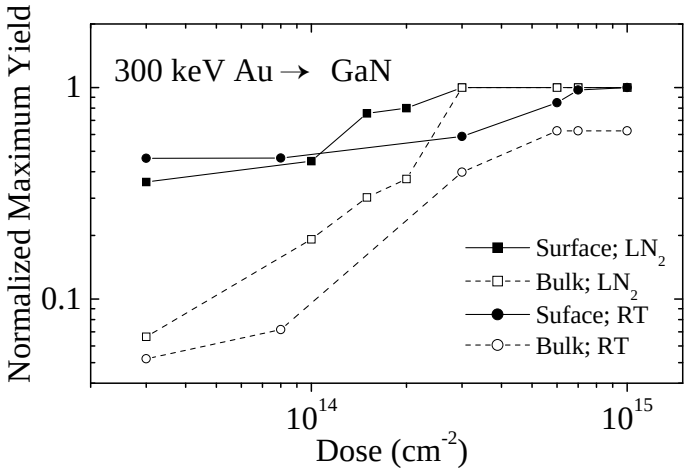

Figure 3.19: Dose dependence of the magnitudes of the bulk and surface defect peaks for 300 keV Au ion bombardment at LN_2 with a beam flux of 3.1×10^{12} cm^{-2} s^{-1} and at RT with a beam flux of 4.4×10^{12} cm^{-2} s^{-1}. The peak levels have been normalized to the random level.

from GaN implanted at RT with 300 keV Au ions to doses of 8×10^{13} [Figs. 3.20(a,b)], 7×10^{14} [Figs. 3.20(c,d)], and 1.5×10^{15} cm^{-2} [Figs. 3.20(e,f)]. Although some defect clusters are seen in the implanted region of the sample bombarded to a dose of 8×10^{13} cm^{-2} [Fig. 3.20(a)], no planar defects have been revealed by XTEM after such a low dose implantation [Fig. 3.20(b)]. Again, a strong surface defect peak in the RBS/C spectrum of this sample [Fig. 3.18(b)] appears to arise from a thin amorphous layer at the GaN surface, as suggested by the bright-field XTEM image [see Fig. 3.21(a)] taken under the same imaging conditions as the images from Fig. 3.5.

XTEM images from the samples implanted to higher doses (7×10^{14} and 1.5×10^{15} cm^{-2}) clearly illustrate point defect clusters [Fig. 3.20(c,e)] and a band of large planar defects [Fig. 3.20(d,f)] produced by heavy ion bombardment. It is also seen from Fig. 3.20(d) that the region between the surface and the bulk defect peaks is relatively free from planar defects. Additional XTEM investigation reveals an amorphous layer on the GaN surface of this sample (a dose of 7×10^{14} cm^{-2}), as shown in Fig. 3.21(b). As expected, the thickness of the surface amorphous layer in this sample (a dose of 7×10^{14} cm^{-2}) is larger than the amorphous layer thickness in the sample implanted to a lower dose of 8×10^{13} cm^{-2}, as seen from Figs. 3.21(a) and 3.21(b). Figures 3.20(e,f) illustrate a relatively thick surface amorphous layer (~ 400 Å thick) in the sample implanted to a dose of 1.5×10^{15}

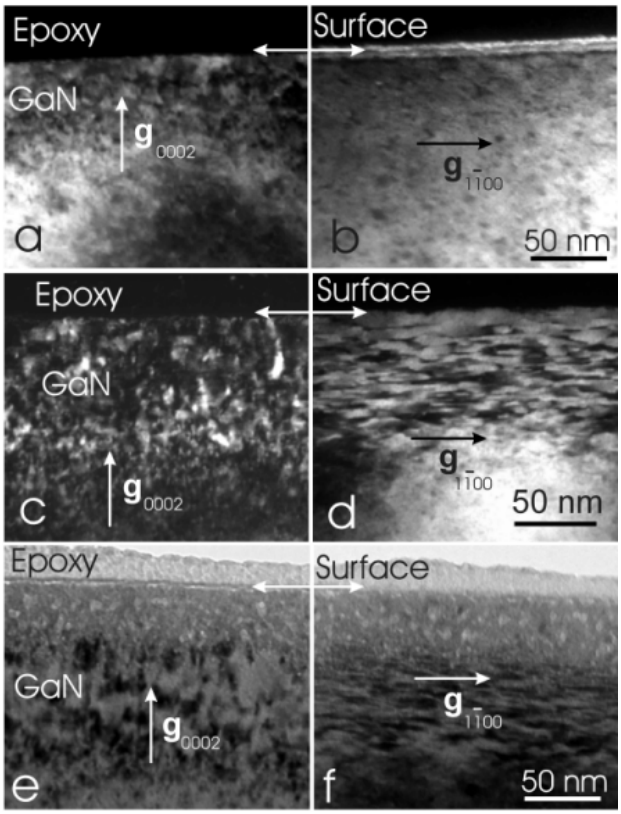

Figure 3.20: Dark-field (a-d) and bright-field (e,f) XTEM images [(a,c,e) $\mathbf{g} = 0002^*$ and (b,d,f) $\mathbf{g} = 1\bar{1}00^*$] of the GaN epilayers bombarded at RT with 300 keV Au ions with a beam flux of 4.4×10^{12} cm^{-2} s^{-1} to doses of 8×10^{13} cm^{-2} (a,b), 7×10^{14} cm^{-2} (c,d), and 1.5×10^{15} cm^{-2} (e,f).

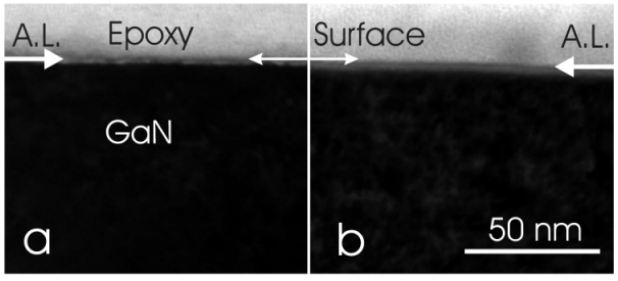

Figure 3.21: Bright-field XTEM images of GaN implanted with 300 keV Au ions at RT with a beam flux of 4.4×10^{12} cm^{-2} s^{-1} to doses of 8×10^{13} (a) and 7×10^{14} cm^{-2} (b). Amorphous layers (labeled as A.L.) on the GaN surface are clearly demonstrated. The thickness of the surface amorphous layer increases with increasing ion dose.

cm^{-2}. This result supports the RBS/C data from Fig. 3.18(b) that, with increasing ion dose, amorphization proceeds layer-by-layer from the surface. Figure 3.20(f) also shows that, in the saturation regime, the damage in the bulk consists of large planar defects in addition to some defect complexes revealed by Fig. 3.20(e) taken under different diffraction conditions.

Another interesting feature evident from Fig. 3.18 is that, for high dose implantation, when the GaN is amorphous, N-deficiency becomes evident even from RBS/C spectra, although the RBS technique is not very sensitive to the stoichiometry. Random spectra shown in Fig. 3.18 represent typical spectra of GaN amorphized by ion bombardment. We assume that an observed increase in the RBS random yield in the near-surface region with increasing ion dose reflects the loss of N from the surface during bombardment. Moreover, N loss has recently been observed by Auger electron spectroscopy after plasma induced etching of the GaN near-surface region [57, 58], attributed to the well-know effect of preferential sputtering,[4] which may significantly change the composition of the near-surface region of a compound semiconductor. Such a loss of N is also supported by our observation of complete decomposition of the GaN near-surface layer and the formation of Ga droplets on the surface of pre-amorphized GaN after annealing in a nitrogen atmosphere at temperatures above about 400 °C. These results, discussed in more detail in Chapter 4, strongly suggest that surface disordering (and amorphization) under ion bombardment stimulates N loss. Furthermore, after irradiation, N loss is much enhanced during annealing.

Bombardment with 450 keV Au ions of GaN capped with SiO_x or Si_xN_y

The formation of an amorphous layer observed at the GaN surface may be due to the effect of preferential loss of nitrogen during ion implantation. To clarify this point, prior to ion bombardment, silicon oxide (SiO_x) or silicon nitride (Si_xN_y) cap layers ($\sim$ 300 Å thick) were deposited on the GaN surface in order to inhibit decomposition of GaN during ion bombardment. RBS/C spectra shown in Figs. 3.22(a) and 3.22(b) illustrate the damage buildup in GaN with a SiO_x layer on the GaN surface bombarded at LN_2 [Fig. 3.22(a)] and RT [Fig. 3.22(b)] with 450 keV Au ions. Figure 3.22(c) shows the RBS/C spectra of GaN with a Si_xN_y cap layer on the GaN surface after bombardment with 450 keV Au ions at RT. The Au ion energy of 450 keV was chosen so that, after traveling through

[4] See, for example, Refs. [23] and [59].

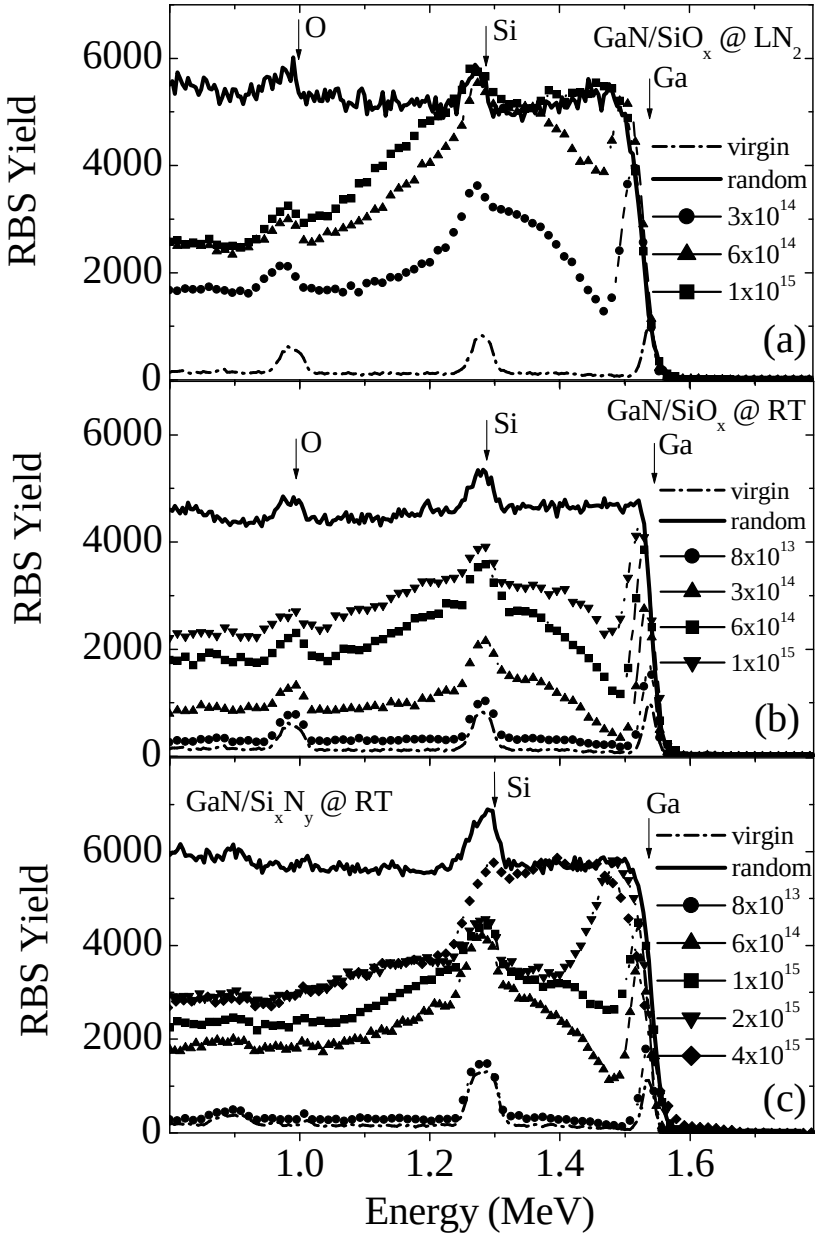

Figure 3.22: RBS/C spectra showing the damage buildup in GaN capped with a SiO_x (a,b) or Si_xN_y (c) layer $\sim$ 300 Å thick. Implantation was carried out with 450 keV Au ions at LN_2 with a beam flux of 3.1×10^{12} cm^{-2} s^{-1} (a) and at RT with a beam flux of 4.4×10^{12} cm^{-2} s^{-1} (b,c). Implantation doses (in cm^{-2}) are indicated in the figure. The positions of surface peaks of Ga, Si, and O are denoted by arrows.

an $\sim$ 300 Å cap layer, the average energy of ions passing through the SiO_x/GaN or Si_xN_y/GaN interface was close to 300 keV. In this case, we can roughly compare this data with the results of 300 keV Au bombardment of GaN without pre-implantation capping (Fig. 3.18).

It is worth noting that, in order to study the effect of capping on surface disordering, a cap layer should not be removed before the RBS/C analysis because we have found that a near-surface layer of GaN which is amorphized by an ion beam is easily removed by HF at RT in contrast to the etching rate of virgin, undamaged GaN. Dry etching of the cap layers, on the other hand, will introduce additional disorder in the near-surface region and, thus, complicate interpretation. In addition, Fig. 3.22 shows that surface peaks of Ga, Si, and O (denoted by arrows) are well separated in RBS/C spectra. Hence, the presence of SiO_x or Si_xN_y cap layers does not interfere with a study of surface disordering in GaN by RBS/C.

It is clearly seen from Fig. 3.22 that capping with either SiO_x or Si_xN_y layers does not eliminate strong surface disordering for both LN_2 and RT bombardment regimes. Therefore, loss of N from the GaN surface during ion irradiation appears to be not the main reason for preferential disordering in the near-surface region of GaN and for the formation of a surface amorphous layer. The formation mechanism of such surface amorphous layers is revealed more fully by the flux behavior, which is discussed below.

Flux effect for bombardment with 300 keV Au ions

Figure 3.23 shows RBS/C spectra illustrating the effect of the beam flux on damage produced by 300 keV Au ion bombardment of GaN at LN_2 [Fig. 3.23(a)] and RT [Fig. 3.23(b)]. It is seen that, with increasing beam flux, the magnitude of the bulk defect peak also increases for both LN_2 and RT implantation regimes. However, Fig. 3.23(b) also shows that, for RT irradiation, the surface defect peak *decreases* in magnitude with increasing beam flux. This so-called *reverse flux effect* [60], is observed also in the case of light ion bombardment of GaN at LN_2 (see Ref. [52]). As discussed more fully below, this would appear to support the important role of mobile point defects in the formation and growth of a surface amorphous layer in GaN under ion bombardment at RT. However, Fig. 3.23(a) shows a normal flux effect (i.e., damage level increases upon increasing beam flux) for the surface defect peak in GaN under irradiation at LN_2. We will discuss the mechanism of

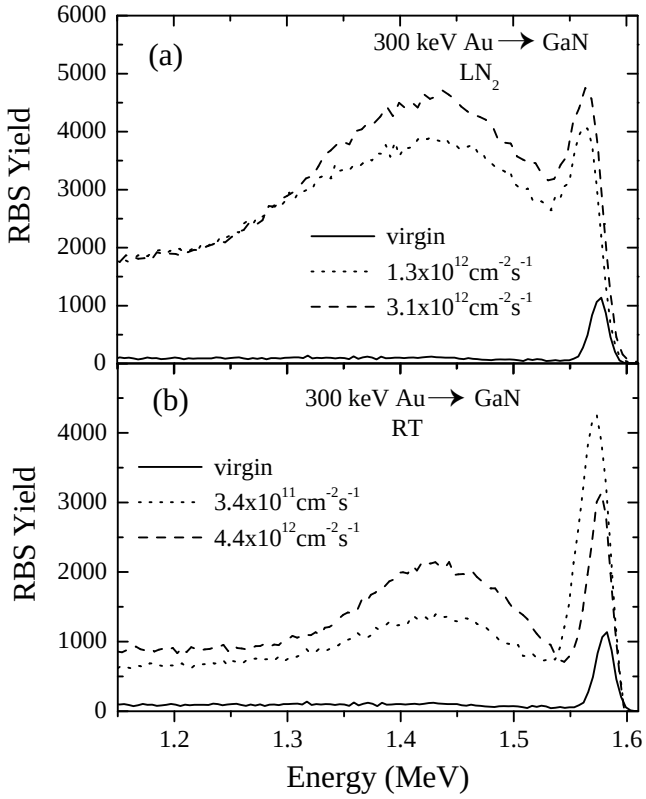

Figure 3.23: RBS/C spectra of GaN implanted with 300 keV Au ions to a dose of 3×10^{14} cm^{-2} at LN_2 (a) and RT (b). The values of beam flux are indicated in the figure. The figure illustrates the reverse and normal flux effects.

the flux effect in detail in Sect. 3.5 as well as in Chapter 8.

Bombardment with Bi ions

Damage buildup for 500 keV Bi ions is illustrated in Fig. 3.24, which shows a quite similar behavior of damage accumulation to that discussed above for the case of irradiation with Au ions for both LN_2 and RT regimes. Indeed, heavy-ion bombardment of GaN at 20 °C results in amorphization which proceeds layer-by-layer from the surface, while disorder in the bulk saturates at some level which is below the random level. For implantation at LN_2, bulk amorphization occurs for both Bi and Au ion bombardment regimes.

It should be noted that, in contrast to lighter ions, the doses required to study the amorphization behavior in GaN during bombardment with heavy ions at LN_2 and RT are relatively low. In this case, when maximum concentrations of implanted species are

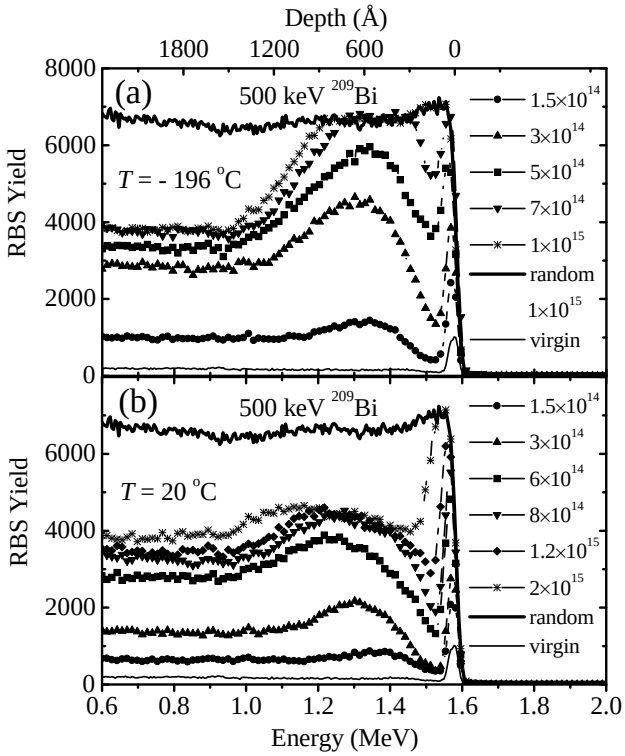

Figure 3.24: RBS/C spectra showing the damage buildup for 500 keV Bi ion bombardment of GaN at LN_2 (a) and RT (b) with a beam flux of $\sim 1 \times 10^{11}$ cm^{-2} s^{-1}. Implantation doses (in cm^{-2}) are indicated in the figure.

≤ 1 at.%, the chemical effects of implanted atoms appear to be negligible at least for the heavy ion species used in this study, as will be shown below. Hence, an analysis of the damage buildup behavior for these ions can assist an understanding of the effects of the density of collision cascades on implantation-produced lattice disorder in GaN. Such an analysis is presented in the following sections.

3.5 Discussion

Results from Sect. 3.4 have revealed that GaN exhibits a rather complex and intriguing damage buildup behavior under ion bombardment. Below, we present a detailed discussion of ion-beam processes in GaN based on our experimental data. Emphasis will be given to an understanding of fundamental aspects of ion-beam damage processes such as the effect of the density of collision cascades, chemical effects of implanted species, the influence of

the sample surface and interfaces on the damage buildup, the formation of extended defects during irradiation as a result of dynamic annealing, and ion-beam-induced stoichiometric imbalance and associated material decomposition. Finally, in Sect. 3.6, we will give a brief comparison of the damage buildup behavior in GaN with that in other materials.

3.5.1 Effect of ion species

To better understand the effect of ion species on the damage buildup behavior in GaN, all RBS/C spectra presented in this chapter have been analyzed using one of the conventional algorithms [61] for extracting depth-profiles of the effective number of scattering centers. For brevity, the number of scattering centers extracted from RBS/C data, normalized to the atomic concentration of GaN, will be referred to below as "relative disorder."

The effect of ion species on the damage buildup behavior in GaN is illustrated in Fig. 3.25, which shows the dose dependence of maximum relative disorder in the bulk for several ion species (extracted from RBS/C spectra) at LN_2 [Fig. 3.25(a)] and RT [Fig. 3.25(b)]. It is seen from Fig. 3.25(a) that GaN exhibits bulk amorphization at LN_2 (with the formation of buried amorphous layers) only for very heavy ions (such as ^{197}Au and ^{209}Bi) and for light ^{12}C and ^{16}O ions. However, in the case of bombardment with intermediate-mass ions studied (^{28}Si, ^{63}Cu, and ^{107}Ag), Fig. 3.25 shows that the damage level in the bulk saturates, and amorphization proceeds only from the surface for both LN_2 and RT bombardment regimes. Hence, ion mass affects not only the level of implantation-produced lattice disorder but also the main features of the damage buildup behavior in GaN.

To better illustrate the effects of ion species on the level of pre-amorphous disorder in GaN, Fig. 3.26 (the left axis) shows the ion mass dependence of the ion doses required to produce 30% relative disorder, $\Phi_{0.3}$, at LN_2 [Fig. 3.26(a)] and RT [Fig. 3.26(b)]. Such ion doses, $\Phi_{0.3}$, have been found by interpolation of damage buildup curves from Fig. 3.25. The level of relative disorder of 0.3 has been chosen since (i) the analysis used to extract relative disorder [61] is not valid for very low levels of implantation-produced damage and (ii) this level is below the saturation level of damage for all ions used. It is seen from Fig. 3.26 (the left axis) that $\Phi_{0.3}$ generally decreases with increasing ion mass. This qualitative trend is expected since the number of ion-beam-generated atomic displacements increases with ion mass. To support this assertion, the last two columns of Table 3.3 give results of TRIM

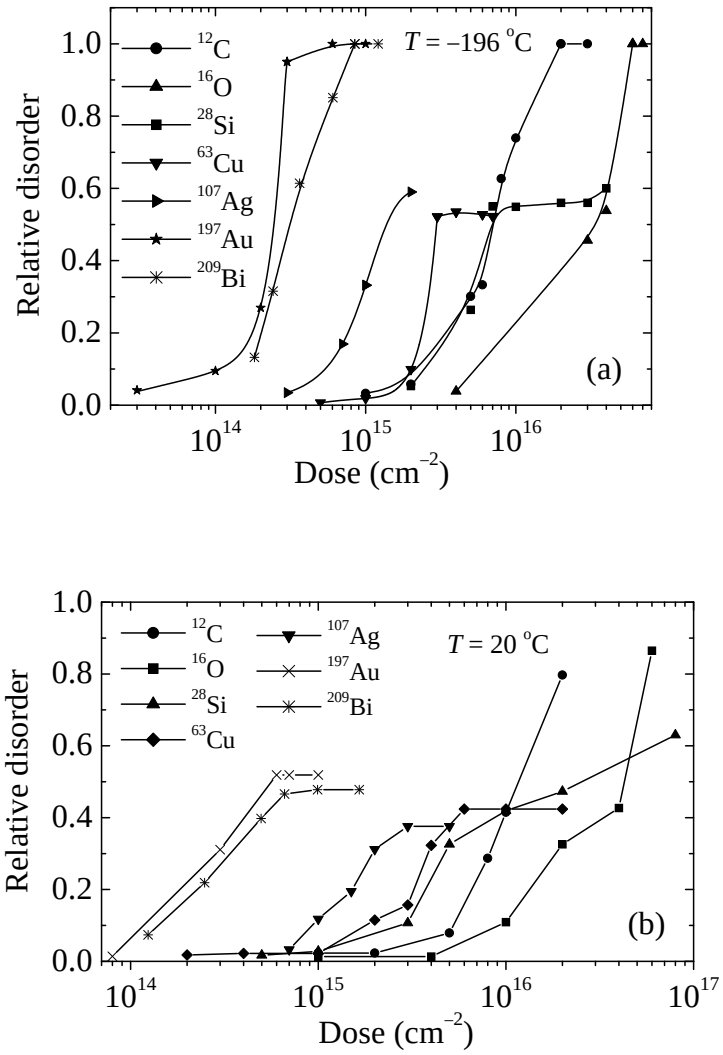

Figure 3.25: Maximum relative disorder (extracted from RBS/C spectra) in the bulk defect peak as a function of dose for 40 keV C, 50 keV O, 60 keV Si, 130 keV Cu, 200 keV Ag, 300 keV Au, and 500 keV Bi ions implanted at LN_2 (a) and RT (b), as indicated in the legend. See Table 3.3 for the details of implant conditions.

calculations [22] of the number of lattice vacancies produced in GaN by the ion species used in this study.

However, two deviations from the trend expected are clearly seen in Fig. 3.26 for the cases of ^{12}C and ^{209}Bi ions for both LN_2 and RT bombardment regimes. For example, $\Phi_{0.3}$ for ^{12}C ions is about two times smaller than $\Phi_{0.3}$ for ^{16}O ions for both LN_2 and RT, despite the fact that ^{16}O ions produce ~ 1.6 times more vacancies than ^{12}C ions in the maximum of the nuclear energy loss profile (see Table 3.3). This is a somewhat extreme example of chemical effects of implanted species, consistent with the data for C shown in Fig. 3.25, as will be discussed in more detail in Sect. 3.5.6. In addition to ^{12}C, irradiation with ^{209}Bi ions produced less stable lattice damage than bombardment with ^{197}Au ions, although ^{209}Bi ions generate a larger number of atomic displacements than ^{197}Au ions. However, this result may be attributed to the lower beam flux value in the case of Bi ions compared with the beam flux value of Au ions (see Table 3.3). Results from Sect. 3.4.5 showed that the level of implantation-produced lattice disorder in GaN depended on ion beam flux. Indeed, with increasing beam flux, an increase in the density of ion-beam-generated point defects enhances interactions between such mobile point defects. This aids the process of the formation of stable defect complexes. Hence, in addition to chemical effects and the effects of the density of collision cascades discussed below, beam flux values must be taken into account for a correct interpretation of the influence of ion species on damage buildup.

Table 3.3 shows that, with an exception of Ag and Bi implants where much lower beam flux values were used, the values of beam flux of different ion species were comparable with each other. Hence, given that the flux effect in GaN is not very strong (see Sect. 3.4.5), we can neglect the influence of the difference in beam flux for different ions (except extreme cases of Ag and Bi) in the analysis of chemical effects and the effects of cascade density on the buildup of implantation-produced damage in GaN presented in this chapter.

A further insight into the effect of ion mass on implantation-produced lattice disorder in GaN is given in Fig. 3.26 (the right axis), which shows the ion mass dependence of ξ_{M_1}, the ratio of the level of lattice disorder of 0.3 (as measured by RBS/C) to the damage level predicted based on ballistic calculations $\Phi_{0.3}N_{vac}^{max}/n_{at}$, where N_{vac}^{max} is the number of lattice vacancies in the maximum of the nuclear energy loss profile (see Table 3.3), and n_{at} is the atomic concentration of GaN. In the first approximation, the parameter ξ_{M_1} reflects the effectiveness of the production of stable lattice disorder (N^{def}) by ion bombardment

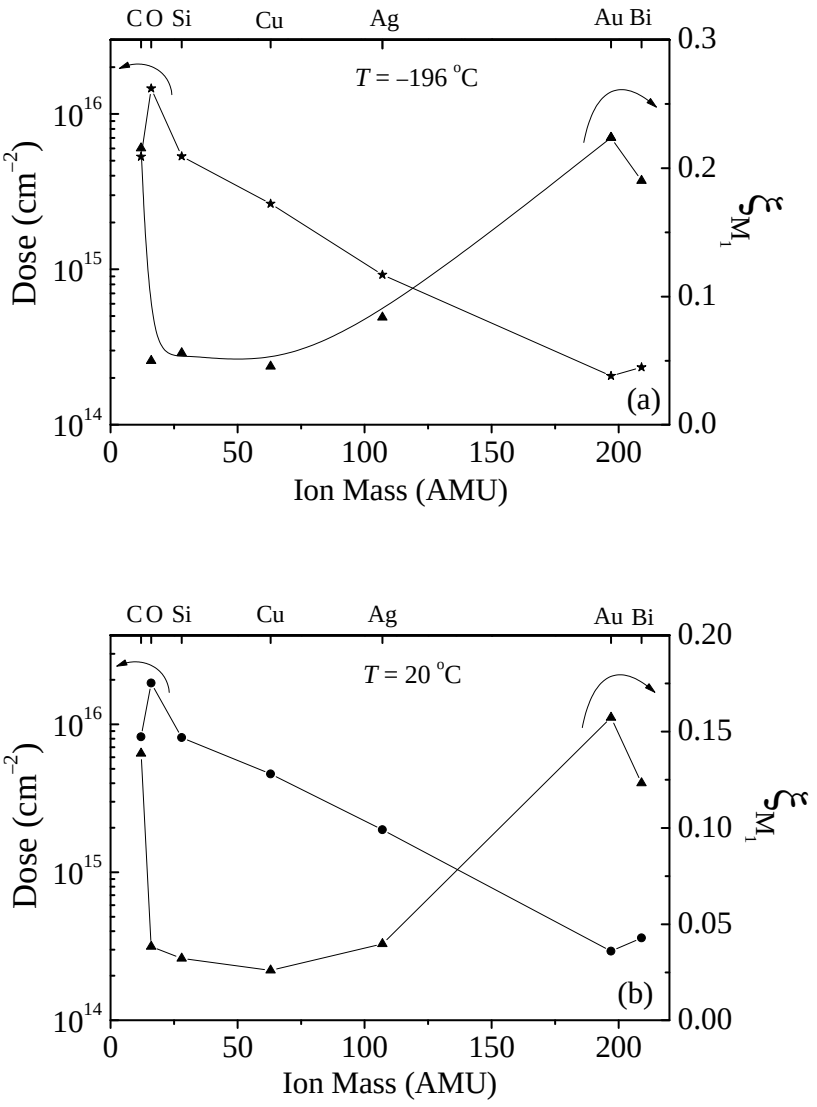

Figure 3.26: Left axis: the ion mass dependence of the ion dose necessary to produce relative disorder of 0.3 (as measured by RBS/C) by implantation at LN_2 (a) and RT (b). Right axis: the dependence of ξ_{M_1} (ξ_{M_1} = the ratio of the level of lattice disorder measured experimentally to the damage level predicted based on ballistic calculations) on ion mass. See Table 3.3 for the details of implant conditions.

under particular implant conditions: $N^{def} = \xi_{M_1} \Phi N_{vac}^{max}$ for relatively low levels of lattice disorder, where Φ is ion dose. If postimplantation stable lattice damage were the same as the one predicted based on ballistic calculations [22], ξ_{M_1} would be equal to unity and independent of ion mass.

In contrast to such expectations, Fig. 3.26 (the right axis) shows a rather complex dependence of ξ_{M_1} on ion mass for both LN_2 and RT bombardment regimes. First of all, for all ion species used, ξ_{M_1} is significantly below unity. This is a direct consequence of strong dynamic annealing processes when a large fraction of ion-beam-generated point defects experiences annihilation even at LN_2. It is also seen from Fig. 3.26 (the right axis) that, with increasing ion mass from ^{12}C to ^{63}Cu, ξ_{M_1} decreases. For ions heavier than ^{63}Cu, ξ_{M_1} shows an increase with increasing ion mass.[5] Interestingly, a comparison of Figs. 3.26(a) and 3.26(b) reveals very similar dependencies for both RT and LN_2 bombardment regimes. However, as compared to the LN_2 case, chemical effects of O and Si ions seem to be even more pronounced at RT, presumably due to larger ion doses $\Phi_{0.3}$ (i.e., the ion doses required to produce 30% relative disorder) in the RT case. It is also somewhat surprising that the main features of ion mass dependencies of $\Phi_{0.3}$ and ξ_{M_1} shown in Figs. 3.26(a) and 3.26(b) for bombardment at LN_2 and RT are similar. Indeed, the rate of thermally-activated defect interaction processes is reduced at LN_2 as compared to the RT case, and a different behavior of $\Phi_{0.3}$ and ξ_{M_1} can be expected at different implantation temperatures. An explanation for such an interesting behavior of ξ_{M_1} is given in the following sections.

3.5.2 Scenario for defect interaction processes

The above extensive experimental data indicates very strong recovery of ion-beam-generated defects in GaN during ion bombardment even at LN_2. In contrast to Si or GaAs, GaN is extremely difficult to amorphize by ion bombardment. For example, amorphous layers in Si or GaAs can be created by keV heavy-ion bombardment at RT to doses of the order of 10^{14} cm^{-2}, while GaN remains crystalline to much higher ion doses [see, for example, Figs. 3.16(b) and 3.18(b)]. This is a direct consequence of very efficient dynamic annealing processes in GaN during ion bombardment. However, dynamic annealing is not perfect. With increasing ion dose, GaN exhibits layer-by-layer amorphization proceeding from the

[5] A legitimate explanation for a low value of ξ_{M_1} in the case of ^{209}Bi ion bombardment (see Fig. 3.26) is the effect of beam flux discussed above.

surface as well as the nucleation and growth of a band of extended defects in the bulk.

A very similar behavior has been observed during elevated temperature ion bombardment of Si or GaAs (see, for example, Refs. [25,62]). In fact, at elevated temperatures, Si and GaAs exhibit strong (but also not perfect) dynamic annealing which leads to eventual buildup of radiation damage in the form of extended defects and, ultimately, depending on sample temperature, to amorphization. During elevated temperature ion bombardment of Si or GaAs, amorphization also often proceeds from the surface.

Although ion beam processes in GaN at LN_2 and RT have some similarity with those in Si and GaAs during elevated temperature bombardment, the damage buildup in GaN appears to be even more complex. Below, we examine a number of defect processes which are plausible in GaN during ion irradiation. In Sect. 3.6, we will briefly return to compare proposed processes in GaN with those discussed in the literature for Si, GaAs, and other materials.

Defect production and dynamic annealing

An energetic ion penetrating through a GaN crystal generates a collision cascade which consists of vacancies in the gallium and nitrogen sublattices (V_{Ga} and V_N), gallium and nitrogen interstitials (Ga_i and N_i),[6] and, presumably, an *amorphous zone* in the cascade core in the case of heavy ions. Such an amorphous zone is expected to form when the damage level in the collision (sub)cascade volume exceeds some threshold value.[7] However, the damage buildup behavior in GaN under heavy-ion bombardment, discussed in Sect. 3.4.5, strongly suggests that amorphous zones generated by heavy ions are not stable in GaN during ion bombardment at LN_2 and above.

Indeed, if amorphous zones were stable, the gross damage level would be a monotonic function of ion dose due to a gradual accumulation of such amorphous zones until complete amorphization of the implanted region.[8] This is in contrast to the highly sigmodal damage buildup experimentally observed even in the case of heavy-ion bombardment (see, for

[6]In our simple scenario, we do not distinguish between interstitials of different symmetry.

[7]For a detailed discussion of amorphous zone formation in semiconductors, see, for example, Refs. [63, 64].

[8]For a brief discussion of the models for damage accumulation in non-metallic solids, see, for example, Ref. [65].

example, Fig. 3.19). The RBS/C damage–depth profiles (which have two peaks) and pronounced dynamic annealing during heavy-ion bombardment of GaN even at LN_2 also support the fact that the disorder buildup is not governed by accumulation of amorphous zones. On the quenching of very dense collision cascades generated by keV heavy ions (such as ^{197}Au or ^{209}Bi), these zones appear to be unstable and anneal via, presumably, both direct thermal and ion-beam-assisted processes [63, 64]. However, the possible formation and dynamic annealing of amorphous zones in GaN under different conditions of ion bombardment deserve additional systematic studies (as, for example, has been recently done for GaAs [66, 67]).

Ion generated simple point defects (V_{Ga}, V_N, Ga_i, and N_i), which survive after quenching of collisional cascades, therefore, appear to dominate damage buildup during both light and heavy-ion bombardment. These defects seem to be mobile even at LN_2, and most of them experience annihilation. This conclusion directly follows from the fact that the experimentally measured amount of lattice disorder is much less than that predicted by calculations (such as the TRIM code [22]), which take into account only collisional processes and neglect defect diffusion and annihilation. Such a substantial annihilation may indicate a high rate of the direct recombination processes: $V_{Ga} + Ga_i \rightarrow 0$, $V_N + N_i \rightarrow 0$. Nevertheless, indirect annihilation processes (recombination of a vacancy [interstitial] via trapping at an interstitial [vacancy] complex) cannot be excluded. Dynamic annealing may also result in the formation of antisite defects ($V_{Ga} + N_i \rightarrow N_{Ga}$; $V_N + Ga_i \rightarrow Ga_N$).

The initial sluggish growth of the gross damage for low ion doses, discussed in Sect. 3.4, is, therefore, due to a considerable recombination of ion-generated point defects. However, defect annihilation is not perfect, and point defect clusters (presumably, complexes of vacancies and/or interstitials, as well as defect-impurity complexes) appear with further increasing ion dose, as indicated by XTEM and RBS/C data presented in Sect. 3.4. It is also reasonable to expect dynamic annealing of these complexes via interaction with ion-generated mobile point defects. For example, a vacancy cluster is expected to anneal via trapping of mobile interstitials. This process, on the other hand, represents an example of a two-step (indirect) annihilation of a Frenkel pair: first, trapping of a vacancy (interstitial) at a complex; second, recombination of this quiescent vacancy (interstitial) with a mobile interstitial (vacancy).

Ion-beam-induced stoichiometric imbalance

The well-known effect of local material stoichiometric imbalance in the collision cascade volume (see, for example, Ref. [68]) may also affect damage accumulation and annealing. Indeed, in the case of a compound semiconductor, an excess concentration of the heavier element exists at shallow depth, while the region at greater depth is enriched with atoms of the lighter element. Calculations show that such stoichiometric disturbances are greatest when the mass ratio of the constituent elements of the semiconductor is high, and when the ion mass is large [68]. Therefore, for the case of implantation of ^{197}Au or ^{209}Bi ions into GaN — a material with a large difference in the masses of constituent elements (^{70}Ga and ^{14}N) — the effect of ion-beam-induced local stoichiometric imbalance should be taken into account.

However, the final local stoichiometry after ion bombardment depends not only on the ballistic collisional processes but also on defect migration and interaction processes. The stoichiometric disturbances may be effectively repaired via defect diffusion and dynamic annealing, processes which are rather effective in GaN at LN_2 and above. Such local stoichiometric imbalance of GaN could significantly affect disorder removal during postimplantation annealing. A spectacular example of the effect of ion-beam-induced stoichiometric imbalance will be given in Chapter 4.

The effect of local stoichiometric imbalance may account for the distorted shape of the RBS/C channeling and random spectra illustrated in Figs. 3.18 and 3.24 for GaN heavily damaged by Au or Bi ions. For example, Fig. 3.18(a) shows that both channeling and random spectra of the sample implanted with 300 keV Au ions to a dose of 1×10^{15} cm^{-2} at LN_2 have a "shoulder" with a decreased RBS/C yield in the ion end-of-range region and an increased yield near the GaN surface. This indicates that the near-surface region of GaN is enriched with Ga atoms, while the region at greater depth has a Ga deficiency. Compared to LN_2, the spectra of GaN implanted with 300 keV Au ions at RT have a less pronounced distortion, as indicated in Fig. 3.18(b).

It should be noted that such a distortion in RBS/C spectra does not seem to be a result of the introduction of a high concentration of Au atoms into the GaN lattice because of relatively small ion doses used ($\sim 1 \times 10^{15}$ cm^{-2}), where Au concentration is ≤ 1 at.%. This conclusion is also supported by the facts that (i) the magnitude of such a distortion does not change with increasing ion dose from 6×10^{14} to 1×10^{15} cm^{-2} for LN_2

bombardment [see Fig. 3.18(a)] and (ii) this distortion is larger for LN_2 implantation than for irradiation at RT although ion doses for RT are larger [see Figs. 3.18(a) and 3.18(b)]. Thus, with increasing implantation temperature, stoichiometric disturbances are more effectively repaired, owing to enhanced defect diffusion and dynamic annealing processes. We will discuss this effect of ion-beam-induced local stoichiometric imbalance in more detail in Chapter 4.

Spatial separation of vacancies and interstitials

A further important mechanism which may significantly affect dynamic annealing and, hence, the damage buildup in GaN is worth mentioning. Indeed, it is well known that vacancies and interstitials are spatially separated in a collision cascade (see, for example, Ref. [23]), with an interstitial excess at the ion end-of-range and a vacancy excess closer to the surface. The effect of such a spatial separation of vacancies and interstitials for each collision cascade is expected to become more pronounced with increasing ion dose. As a result, this effect could also be important in controlling damage accumulation in GaN, given the high ion doses required for amorphization of GaN.

Perspectives for developing a quantitative model

Finally, a comment should be made on the possibility of developing a quantitative model for the damage buildup in GaN. It is clear that all "traditional" quantitative models (see, for example, Refs. [65, 69] and references therein) can be applied only when the rate of dynamic annealing is considerably lower than the defect production rate, which is not the case even for heavy-ion bombardment of GaN at LN_2. At present, the development of a model which takes into account elemental defect processes and dynamic annealing in GaN during ion bombardment appears to be a rather difficult task due to a very limited understanding of these processes. It is clear that additional studies are necessary before a satisfactory quantitative model for damage buildup in GaN can be developed.

3.5.3 Formation of extended defects and their influence on amorphization

Our XTEM investigation presented in Sect. 3.4 has revealed that defect recombination and the formation of point defect complexes are not the only processes taking place in GaN during ion bombardment. Interestingly, *during* ion bombardment, a band of planar defects in the crystal bulk also nucleates with increasing ion dose for all implant conditions studied (such as different ion masses and different irradiation temperatures). Hence, these planar defects, which are parallel to the basal plane of the nitride film, are defect structures characteristic for ion-bombarded GaN. They are a result of point defect agglomeration processes during imperfect dynamic annealing.

With a further increase in ion dose, in cases of implantation with C, O, Au, or Bi ions at LN_2, the damage in the GaN bulk exhibits a very rapid growth from a low level to amorphization, as discussed in Sect. 3.4. This rapid damage buildup (or a strong sigmodality of the damage–dose function) is a characteristic feature of nucleation limited amorphization, where the initial stage of ion bombardment results in the formation of "nucleation sites" for amorphization. When such "nucleation sites" are formed, subsequent irradiation of a predamaged crystal leads to a very fast increase in the damage level with increasing ion dose.

A correlation between RBS/C and XTEM data indicates that the onset of the fast growth of damage with increasing dose of C, Au, or Bi ions at LN_2 (as observed by RBS/C) coincides with the formation of the planar defects (as observed by XTEM). This fact may *suggest* that the planar defects are plausible candidates for the "nucleation sites" of amorphization at LN_2. When these planar defects form, an increase in ion dose results in very fast damage accumulation.

3.5.4 Saturation of bulk disorder

Results presented in Sect. 3.4 have shown that, for irradiation with keV intermediate-mass ions (Si, Cu, and Ag) at LN_2 and RT and with heavy ions (Au and Bi) at RT, with increasing ion dose, the damage level (as measured by RBS/C) in the GaN bulk region saturates below the random level, and layer-by-layer amorphization proceeds only from the GaN surface. For this saturation regime, the disorder in the bulk consists of some

point defect complexes and a band of planar defects as revealed by XTEM. Results from Sect. 3.4 show that the band of planar defects broadens with further increasing dose. This band of planar defects does not amorphize independently of the surface amorphous layer (as has been observed for C and O ions) but, rather, is consumed by the advancing surface amorphous layer.

The above effect of bulk damage saturation represents an interesting example when the processes of defect production and removal are balanced in some region of a crystal. It should be noted that the existence of such a saturation regime does not necessarily require that all point defects generated by an ion beam in some region of a sample exhibit perfect annihilation. Indeed, point defects produced by ion irradiation in the region with planar defects might not increase the density of such extended defects but, rather, lead to the expansion of the planar defect band. At present, it is difficult to propose an unequivocal microscopic mechanism to account for the existence of the saturation regime and the extension of the band of planar defects. However, this effect may be attributed to (i) the enhanced annihilation of point defects within the region containing a saturation density of planar defects and/or to (ii) energetically favorable processes (possibly stress-induced) related to defect annihilation and/or agglomeration after the nucleation of a band of planar defects.

3.5.5 Surface amorphization

In this section, we discuss the main features of ion-beam-induced amorphization which proceeds layer-by-layer from the GaN surface. Results from Sect. 3.4 have shown that the defect processes during ion bombardment of GaN are complicated by the influence of the GaN surface (or the GaN/capping layer interface). Indeed, the GaN surface appears to represent an effective sink for migrating point defects. The flux behavior (see Fig. 3.23) suggests that mobile point defects play an important role in the formation and growth of the surface amorphous layer. Indeed, a normal flux effect (i.e., with increasing beam flux, the damage level also increases) is observed for the bulk peak of damage (see Fig. 3.23). This is consistent with the current understanding of implantation damage buildup in semiconductors under implantation conditions when substantial dynamic annealing of radiation defects takes place (see, for example, Refs. [25, 62, 69]). An increase in beam flux decreases the average time interval between collision cascades which spatially

overlap. Such an increase in the generation rate of point defects with increasing beam flux enhances the rate of interactions between mobile defects and, therefore, enhances the formation of defect complexes. However, Fig. 3.23(b) also shows that the surface defect peak decreases in magnitude with increasing beam flux. This reverse flux effect can be qualitatively explained in terms of the competition between defect trapping and migration processes. Indeed, an increase in the beam flux enhances the formation of defect complexes in the crystal bulk. As a result, fewer point defects generated in this region can reach the surface.

The influence of the surface on the point defects generated in the crystal bulk is determined by the effective mobility of defects and, of course, by the distance between the surface and the region where these defects are generated. For example, a comparison of Figs. 3.16 and 3.18 shows that the main features of damage buildup remain the same upon increasing the energy of Au ions from 100 keV to 300 keV. The effect of ion energy on implantation disorder in GaN is better illustrated in Fig. 3.27. This figure shows that the main features of damage buildup do not change upon increasing the energy of Au ions from 100 keV to 2000 keV. One can see the same highly sigmodal damage buildup and the nucleation of two amorphous layers (surface and buried) for all three ion energies. In all three cases, the two amorphous layers — at the surface and in the bulk — nucleate and grow via a layer-by-layer amorphization process with increasing ion dose, as has also been confirmed by XTEM. Ultimately, with further increasing dose, these two layers meet, resulting in a thick surface layer of an amorphous material.

It is also interesting to note that, for low ion doses, the surface defect peak for RT 300 keV Au ion bombardment is larger than that for irradiation at LN_2, as indicated in Fig. 3.19. This fact, as well as the reverse flux effect on the surface defect peak [see Fig. 3.23(b)], might suggest that, during relatively low dose 300 keV Au ion bombardment at RT, point defects generated in the whole implantation region (up to ~ 900 Å from the GaN surface) contribute to the formation of the surface amorphous layer. In contrast, the normal flux effect (i.e., the damage level increases upon increasing beam flux) for the surface defect peak for 300 keV Au ion bombardment at LN_2 [Fig. 3.23(a)] may be attributed to smaller effective diffusion lengths of point defects, as compared to ion irradiation at RT.

A thin surface amorphous layer has been observed in GaN implanted to a relatively

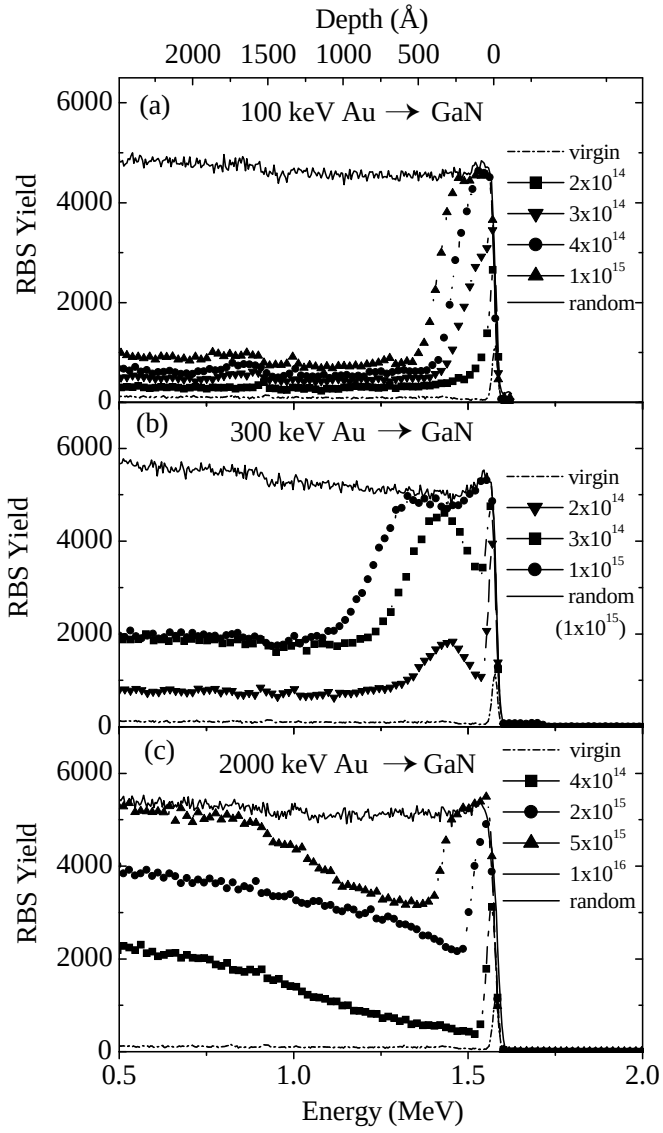

Figure 3.27: RBS/C spectra illustrating the damage buildup in GaN bombarded at LN_2 (a) with 100 keV Au ions with a beam flux of 1.4×10^{13} cm^{-2} s^{-1}, (b) by 300 keV Au ions with a beam flux of 3.1×10^{12} cm^{-2} s^{-1}, and by 2000 keV Au ions with a beam flux of 5×10^{12} cm^{-2} s^{-1}. Implantation doses (in cm^{-2}) are indicated in the figure.

low dose of 300 keV Au ions at LN_2, as shown in Fig. 3.21(a). In addition, Fig. 3.5(a) clearly indicates the presence of a surface amorphous layer for a relatively high dose (8×10^{15} cm^{-2}) of 40 keV C ions implanted at LN_2. Nevertheless, it is interesting to ascertain whether or not the surface defect peak measured by RBS/C for lower doses results from an amorphous layer. Our XTEM investigation on samples implanted with 40 keV C ions with a beam flux of 1.4×10^{13} cm^{-2} s^{-1} to a dose of 1×10^{15} cm^{-2} at LN_2 and RT did not reveal any amorphous layer on the GaN surface. Therefore, the strong surface peak in RBS/C spectra of low dose irradiated GaN samples seems to arise from the lattice reconstruction of the first several monoatomic layers on the GaN surface due to, presumably, (i) the accumulation of point defects at the GaN surface, (ii) ion-produced preferential loss of N, and/or (iii) recoil implantation of the impurities from a thin layer of surface contamination. Such a very thin near-surface layer of reconstructed lattice may act as a precursor for a surface amorphous layer which appears with increasing ion dose.

It also is worth mentioning that the surface peak of disorder produced by ion bombardment of semiconductors is not a new effect. This effect was studied in the 1970's by different experimental techniques (such as RBS/C, electron diffraction, electron paramagnetic resonance, and electron backscattering) for the case of ion implantation into Si (see, for example, a discussion in Ref. [60] and references therein). In addition, the nucleation of amorphous layers in Si preferentially at the surface has been observed during elevated temperature bombardment. The surface peak of damage has also been studied in Ge and GaAs, and, very recently, ion-bombardment-induced anomalous surface disordering in Si has received new interest due to important applications of low energy ion beams for the formation of very shallow junctions in Si (see a discussion in Ref. [60]).

The results of previous studies on Si, Ge, and GaAs also suggest that the origin of the surface defect peak can be attributed to an amorphous layer at the semiconductor surface, presumably, formed due to trapping of migrating point defects by the surface. In the case of GaN, the data presented in this thesis shows that the strong surface peak of disorder also often arises from an amorphous layer on the GaN surface, as indicated by XTEM. In addition, the flux behavior of damage strongly supports the fact that the surface defect peak in GaN may be attributed to trapping of mobile point defects by the GaN surface.

To better understand the mechanism of surface amorphization, Fig. 3.28 illustrates the dose dependence of the thickness of surface amorphous layers in GaN bombarded with 130

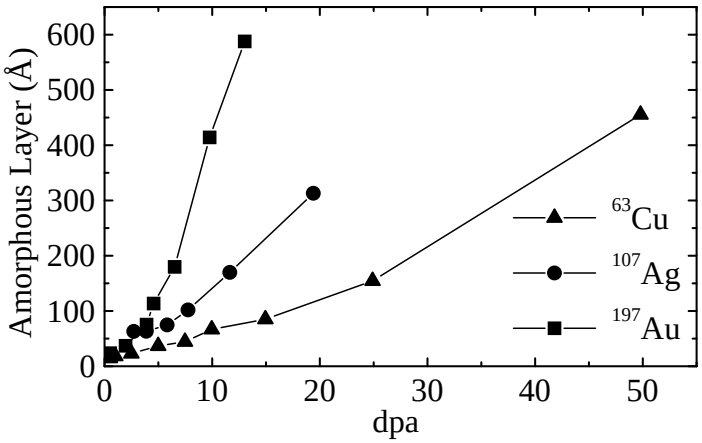

Figure 3.28: Dependence of the thickness of surface amorphous layers on dpa for bombardment of GaN with 130 keV Cu, 200 keV Ag, and 300 keV Au ions at RT. See Table 3.3 for the details of implant conditions.

keV Cu, 200 keV Ag, and 300 keV Au ions at 20 °C. In order to compare results obtained for different ion species, ion doses in Fig. 3.28 were multiplied by N_{vac}^{max}/n_{at}, and the product is shown as dpa (displacements per atom).[9] The thickness of surface amorphous layers shown in Fig. 3.28 has been determined from RBS/C spectra. An assumption was made in cases where the RBS/C surface peaks did not reach the random level, namely that they originate from a completely disordered material at the surface. As discussed earlier in this thesis, such an assumption has been supported by XTEM studies, especially in the case of heavy-ion bombardment and relatively thick surface amorphous layers as shown in Fig. 3.28. The thickness of amorphous layers determined using this method is consistent with amorphous layer thickness determined for some samples using XTEM or directly from RBS/C spectra in the case of thick surface amorphous layers.

[9]It should be noted that, although the number of vacancies generated in the maximum of the nuclear energy loss profile (N_{vac}^{max}) is larger than the number of vacancies generated at the GaN surface, Fig. 3.28 still can be used to ascertain the influence of ion mass on the rate of surface amorphization. Indeed, the ratio of N_{vac}^{max} to that value at the surface is compatible for all three ions shown in Fig. 3.28. A somewhat more accurate analysis would require integration of defect generation profiles over some distance from the surface or the amorphous/crystalline interface. However, such integration would require knowledge of the parameters describing defect migration and interactions. Unfortunately, at present, not only the numerical values for such parameters but also the dominant defect interaction processes in GaN are unknown.

Figure 3.28 shows that the rate of planar amorphization (normalized to dpa) proceeding from the GaN surface increases with increasing ion mass. This may result from cascade density effects, whereby defect clustering rather than annihilation is effectively enhanced, as will be discussed more fully in the following section. Interestingly, such a discussion will help us to better understand the influence of the density of collision cascades on ion beam damage in GaN.

Figure 3.28 also shows that the thickness of surface amorphous layers superlinearly depends on ion dose. This effect can be attributed to the fact that, with increasing ion dose, the amorphous/crystalline interface moves into a region with a larger level of defect generation by the ion beam. Alternatively, the fact that the amorphous/crystalline interface moves into a region with a larger level of implantation-produced lattice damage may also result in a superlinear dependence of the thickness of surface amorphous layers on ion dose if stable defects near the amorphous/crystalline interface aid the process of layer-by-layer amorphization.

Our results also show that the amorphization rate increases with decreasing implantation temperature from 20 to -196 °C. This is a typical behavior for ion-beam-induced epitaxial amorphization which occurs in different semiconductors under certain implant conditions (see, for example, Refs. [70, 71]) However, at present, the micro-mechanism of layer-by-layer amorphization is still unknown. Even for Si, for which such a non-equilibrium phase transition has been studied most extensively [70,71] an adequate model for ion-beam-induced epitaxial amorphization has not been developed, partly due to the complexity of this problem.

3.5.6 Chemical effects

We attribute a decrease in ξ_{M_1} [i.e., the ratio of the level of lattice disorder of 0.3 (as measured by RBS/C) to the damage level predicted based on ballistic calculations] with increasing ion mass for light ions (from ^{12}C to ^{63}Cu) both at LN_2 and RT, as well as the occurrence of bulk amorphization for bombardment with C and O ions, to dominating chemical effects due to relatively high concentrations of implanted species. Although the scale of such chemical effects depends on the particular ion species used, Figs. 3.25 and 3.26 indicate that all light ions used in this study (C, O, and Si) effectively enhance the buildup of implantation disorder both at LN_2 and RT. However, carbon exhibits the largest effect,

as clearly shown in Figs. 3.25 and 3.26.

A chemical enhancement of damage buildup, as observed by RBS/C, can be due to (i) the trapping of ion-beam-generated migrating point defects by implanted impurity atoms, (ii) second phase formation and associated lattice distortion, and/or (iii) enhanced stability of irradiation-induced defects in GaN containing a high concentration of C, O, or Si. Indeed, trapping of migrating defects at impurity atoms may result in stable defect clusters which are observed as enhanced scattering centers in RBS/C or directly by XTEM. At high concentrations (above a few atomic percent), precipitation of a second phase involving the implanted atoms is increasingly likely, thus leading to disordering of the surrounding GaN matrix. Alternatively, large concentrations of implanted atoms may enhance the stability of an amorphous phase in GaN by defect trapping and/or influencing energy barriers for defect migration and interactions. Additional studies would be desirable to ascertain the contributions to the chemical effect from each of the above three processes.

3.5.7 Role of collision cascade density

In this section, we discuss the effect of the density of collision cascades on implantation-produced lattice disorder in GaN. The buildup of damage in the bulk, as characterized by the parameter ξ_{M_1}, is treated first.

Effect on bulk disorder

Figure 3.26 shows that ξ_{M_1} increases with increasing ion mass for relatively heavy ions (^{63}Cu, ^{107}Ag, and ^{197}Au) both at LN_2 and RT. Amorphization studies in GaN bombarded with these heavier ions require relatively low ion doses. Hence, the chemical effects of implanted species appear to be negligible, and the ion mass dependence of ξ_{M_1} should mainly reflect the effect of the density of collision cascades. Data from Figs. 3.25 and 3.26 shows that an increase in the density of collision cascades strongly enhances the level of implantation-produced stable lattice disorder in GaN both at LN_2 and RT.[10] This effect can be attributed to an increase in the efficiency of clustering of mobile point defects into stable defect complexes with increasing density of ion-beam-generated point defects.

[10]A strong effect of the density of collision cascades on stable implantation damage in GaN discussed here is also supported by our recent molecular effect studies, the details of which can be found in Ref. [72].

Such an explanation is supported by the flux effect observed in GaN during heavy-ion bombardment (see Sect. 3.4.5). Both cases, the cascade effect and the flux effect, may indicate that defect clustering efficiency increases with the rate of defect generation. It should be noted that an increase in the density of collision cascades should enhance the formation of stable defects even for implant conditions when the flux effect is weak. This is due to the fact that interaction processes between mobile point defects from the same collision cascade may occur in much shorter time intervals than migration and interaction of defects produced in different collision cascades.

An additional explanation for the strong dependence of implantation-produced stable lattice disorder in GaN on the density of collision cascades (revealed in Fig. 3.26) is a superlinear dependence of the concentration of ion-beam-produced point defects, which survive cascade quenching, on the density of collision cascades. This effect may be attributed to collective energy spike processes which take place in dense collision cascades formed by heavy ions within very short time intervals of ~ 10 ps. These nonlinear energy spike processes (such as displacement and/or thermal spikes) are well accepted in the literature in the case of Si [63], the most extensively studied semiconductor, to explain the superlinear dependence of ion-beam-generated lattice disorder on cascade density.

Alternatively, the mass-dependent damage buildup may be due to a decrease in the effective displacement energy of atoms in the GaN matrix with increasing density of collision cascades. This effect may result from either the breaking of a large number of atomic bonds within a relatively small volume of a collision cascade or the reduced displacement energy of atoms with missing nearest neighbors which arises due to a very high displacement density [63]. There may also be local material decomposition occurring within dense collision cascades, as will be discussed in more detail in Chapter 4. Both these effects would also be expected to result in a superlinear dependence of ion-beam-generated defects on the density of collision cascades.

Effect on surface amorphization

A superlinear dependence of the concentration of ion-beam-produced defects on cascade density discussed above appears to be supported by results from Fig. 3.28 (discussed in Sect. 3.5.5), which shows that the rate of planar amorphization proceeding from the GaN surface also increases with increasing density of collision cascades. However, the process

of surface amorphization is rather complex. For example, the observed surface amorphization behavior can be attributed to complex nonlinear disordering processes which favor clustering of ion-beam-generated defects at the amorphous/crystalline interface with increasing density of collision cascades. If such nonlinear defect accumulation at the amorphous/crystalline interface takes place, an increase in cascade density will also result in an increased rate of surface amorphization. Alternatively, an increase in the rate of surface amorphization with increasing density of collision cascades may be due to a decreased degree of lattice reordering during quenching of very dense collision cascades produced by heavy ions. Indeed, in contrast to the situation in the crystal bulk, where cascades are surrounded by the crystal on all sides, the presence of an amorphous/crystalline interface may hinder the process of lattice reordering during cascade quenching. For example, if a dense collision cascade behaves like a thermal spike, quenching and subsequent recrystallization of the resultant molten zone may be inhibited by the presence of an amorphous/crystalline interface. This effect might be expected to be enhanced as cascade density increases. As a result, this may lead to an increase in the rate of surface amorphization with increasing density of collision cascades.

It should also be noted that the above cascade density effects, as revealed in Fig. 3.28, cannot be explained by a possible increase in the flux of point defects migrating from the bulk toward the surface or amorphous/crystalline interface. Indeed, although layer-by-layer amorphization is generally attributed to the trapping of such migrating point defects by the surface or amorphous/crystalline interface, an increase in the defect clustering efficiency in the bulk, with increasing density of collision cascades, results in a decrease in the flux of point defects migrating from the bulk toward the surface and, hence, cannot account for the experimental data shown in Fig. 3.28. Moreover, such a long-range migration of point defects in GaN during ion irradiation appears to occur only for rather low ion doses (i.e., low levels of lattice disorder in the crystal). Indeed, an increased rate of surface amorphization in the case of ion bombardment using low beam fluxes (as illustrated in Figs. 3.14 and 3.28 in the case of Ag ion bombardment) occurs only for rather low ion doses. With increasing ion dose and, hence, the level of implantation-produced lattice disorder, effective diffusion lengths of point defects seem to decrease, presumably due to an increase in the probability of defect interactions and local clustering. However, it is clear that, at present, further studies are desirable to better understand the mech-

anism of planar amorphization and the physical processes responsible for the increase in implantation-produced stable lattice damage with increasing cascade density observed in this study.

3.6 Comparison with other materials

Finally, we make a brief comparison of the implantation disorder buildup in GaN with that in other crystalline materials. As alluded to earlier, some features of the damage buildup in GaN at LN_2 resemble those occurring in Si or GaAs during elevated temperature ion bombardment. Indeed, during elevated temperature ion bombardment of these latter materials, when dynamic annealing of ion-generated defects is strong, damage accumulation proceeds via the formation of an array of extended defects, as has been reviewed elsewhere [25]. These extended defects in Si or GaAs are usually tangles of dislocations, and their density increases with increasing ion dose. This causes a continuous rise in the total energy of the system until the system collapses into the energetically more preferable amorphous state [25]. In addition, in Si or GaAs bombarded at elevated temperatures, layer-by-layer amorphization can proceed from the surface. In this case, the surface acts as a "nucleation site" for amorphization.

The scenario for amorphization in GaN under ion bombardment at LN_2 appears to be qualitatively similar to that in Si or GaAs at elevated implant temperatures. Indeed, damage evolution in GaN proceeds via the formation of a band of extended defects. The surface of GaN also acts as a "nucleation site" for amorphization. However, the ion-produced extended defects in GaN consist of a regular array of planar defects, not dislocation tangles as in Si or GaAs. Moreover, the presence of a saturation regime during RT bombardment of GaN with heavy ions may suggest that the process of amorphization in GaN is more complex than that in Si or GaAs during elevated temperature bombardment. Indeed, in addition to chemical effects of implanted atoms, amorphization of GaN seems to be stimulated by the processes of local stoichiometric imbalance which should become pronounced for high ion doses. This may explain why amorphous zones presumably generated in dense collisional cascades produced by heavy ions appear to be unstable in GaN, whereas surface and buried amorphous layers can be nucleated for very high ion doses.

It should also be noted that chemical enhancement of damage buildup discussed in

this chapter is, in fact, not new and has previously been found in both semiconductors and metals (see, for example, Refs. [73–78]). Indeed, chemical effects often dominate the damage buildup behavior in an implantation regime with strong dynamic annealing when large ion doses are needed to observe significant disorder. Such strong dynamic annealing, which occurs in GaN even during heavy-ion bombardment at LN_2, is somewhat similar to the situation for most metals [73] or even for mature semiconductors (such as Si and GaAs) during ion irradiation at elevated temperatures [74,75] as well as for most of (ionic) ceramic materials [76–78]. For example, in the case of implantation-produced damage in metals, it has been recognized that chemical effects of ion species implanted to large ion doses result in a reduced level of dynamic annealing and stabilization of an amorphous phase [73]. Most metals, particularly elemental metals, are impossible to amorphize even by heavy-ion bombardment at low temperatures without such a chemical stabilization of the amorphous phase. This experimental fact has previously been attributed to extremely efficient dynamic annealing processes in metals [73] which is somewhat similar to the situation in GaN.

In the case of Si, bombardment with ^{12}C ions at RT has previously been shown to result in an enhanced damage accumulation compared to the case of irradiation with other light ion species such as ^{11}B. This effect has been attributed to the formation of stable complexes of Si self-interstitials with C atoms [74, 75]. Finally, a discussion of chemical effects of implanted species on the damage accumulation in various ceramics (such as Al_2O_3, $MgAl_2O_4$, MgO, Si_3N_4, and SiC) can be found in Ref. [78].

3.7 Summary

Structural disorder in GaN bombarded with keV H, C, O, Si, Cu, Ag, Au, and Bi ions at LN_2 and RT has been studied by a combination of RBS/C and XTEM. Results have shown that strong dynamic annealing processes lead to a complex dependence of the damage buildup behavior in GaN on ion species, including preferential surface disordering. Such preferential surface disordering is due to the formation of surface amorphous layers and attributed to the trapping of mobile point defects by the GaN surface or the amorphous/crystalline interface. In addition to the formation of point defect clusters, the damage buildup in GaN at LN_2 and above proceeds via the formation of planar defects

which are parallel to the basal plane of the GaN film. For some irradiation regimes, bulk disorder saturates below the amorphization level, and, with increasing ion dose, amorphization proceeds layer-by-layer only from the GaN surface. In the case of light ions, chemical effects of implanted species can strongly affect damage buildup. Such implanted atoms appear to stabilize an amorphous phase in GaN and/or to act as effective traps for ion-beam-generated mobile point defects and enhance damage accumulation. For heavier ions, an increase in the density of collision cascades strongly increases the level of stable implantation-produced lattice disorder in the bulk as well as the rate of layer-by-layer amorphization proceeding from the surface. Physical mechanisms of surface and bulk amorphization and various defect interaction processes in GaN have been discussed.

In addition to fundamental interest, results presented in this chapter have important technological implications. Indeed, all technological steps involving ion-beam processing create lattice defects. An unexpected and complex behavior, revealed in this study, such as lattice amorphization, local stoichiometric imbalance and associated material decomposition, preferential surface disordering and N loss, and the formation of extended defects should be taken into account if potential applications of ion implantation for the fabrication of GaN-based devices are to be fully exploited. Finally, results of this chapter will clearly stimulate further research both to probe some of the mechanisms for unusual ion-induced effects and also to develop processes to avoid or repair unwanted structural damage produced by ion bombardment.

Chapter 4

Ion-beam-induced porosity of GaN

4.1 Introduction

As has been shown in Chapter 3, GaN can be rendered amorphous by high-dose light or heavy-ion bombardment. In the present chapter, we discuss the structure of GaN amorphized by ion implantation. Our results show that GaN layers amorphized by heavy-ion ($^{197}Au^{+}$) bombardment are porous. The formation of a porous structure causes large material swelling and increased surface roughness. Our results also strongly suggest that porous GaN consists of a highly N-deficient amorphous GaN matrix with N_2 gas bubbles (and Ga-rich regions) embedded. This intriguing phenomenon appears to be a result of ion-beam-induced stoichiometric disturbances causing decomposition of GaN.

4.2 Experimental

The $\sim$ 2 μm thick wurtzite undoped GaN epilayers used in this study were grown on *c*-plane sapphire substrates by MOCVD. Implantation with 2 MeV $^{197}Au^{+}$ ions was done at liquid nitrogen temperature (LN_2) with a beam flux of 5×10^{12} cm^{-2} s^{-1} over the dose range from 1×10^{14} to 5×10^{16} cm^{-2}. During implantation, samples were tilted by $\sim 7^{\circ}$ relative to the incident ion beam to avoid channeling. After implantation, samples were studied by Rutherford backscattering/channeling (RBS/C) spectrometry. Selected samples were also studied by cross-sectional transmission electron microscopy (XTEM). The surface morphology of all implanted samples was studied by tapping-mode atomic force microscopy (AFM).

4.3 Swelling and porosity

An AFM image in Fig. 4.1 illustrates the border between implanted (on the left) and unimplanted (on the right) areas of a GaN sample bombarded with 2 MeV Au ions at LN_2 to a dose of 1×10^{16} cm^{-2}. As clearly seen, ion implantation has caused pronounced material swelling with a step height as large as $\sim$ 1700 Å. In addition, the implanted area exhibits large-scale roughness.

Shown in Fig. 4.2 is the dose dependence of the step height between implanted and unimplanted regions of 2 MeV Au ion bombarded GaN, as measured by AFM. It is seen that a rapid step height increase occurs for ion doses above $\sim 3 \times 10^{15}$ cm^{-2}. Figure

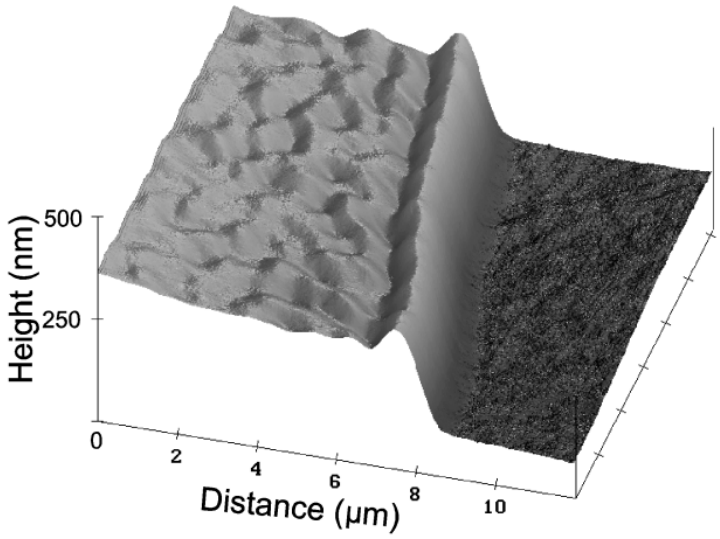

Figure 4.1: Tapping-mode AFM image illustrating the border between implanted (on the left) and unimplanted (on the right) areas of a GaN sample bombarded with 2 MeV Au ions at LN_2 to a dose of 1×10^{16} cm^{-2} with a beam flux of 5×10^{12} cm^{-2} s^{-1}.

4.3(a) shows a (low magnification) XTEM image of GaN bombarded with 2 MeV Au ions at LN_2 to a dose of 1×10^{16} cm^{-2}. This XTEM image illustrates an $\sim$ 5500 Å thick, completely amorphous surface layer bounded by an $\sim$ 1000 Å thick band of defect complexes and planar defects, which has been confirmed by detailed XTEM and electron diffraction measurements. An enlarged image of the near-surface part of the same sample is shown in Fig. 4.3(b). It is seen that the amorphous GaN layer has voids or gas bubbles which are close-to-spherical in shape. The average radius of the voids/bubbles depends on the depth and seems to scale with the nuclear energy loss profile of Au ions.

A combination of RBS/C, XTEM, and AFM data shows that the onset of the large step height, with increasing ion dose, coincides with the nucleation of a buried amorphous layer in the region of the maximum nuclear energy loss. Moreover, a rapid step height increase in the dose range from $\sim 3 \times 10^{15}$ to $\sim 7 \times 10^{15}$ cm^{-2} (see Fig. 4.2) corresponds to the dose interval in which buried and surface amorphous layers extend until they meet, resulting in a thick continuous layer of an amorphous material. These results indicate that ion-beam-induced porosity and concomitant material swelling are effects observed only in *amorphous* GaN. Relatively small material expansion (see Fig. 4.2) for ion doses before

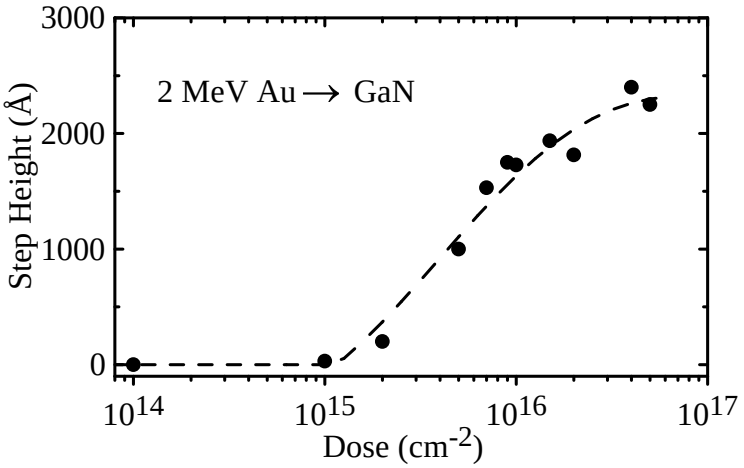

Figure 4.2: Dose dependence of the step height between implanted and unimplanted regions of GaN films bombarded with 2 MeV Au ions at LN_2 with a beam flux of 5×10^{12} cm^{-2} s^{-1}.

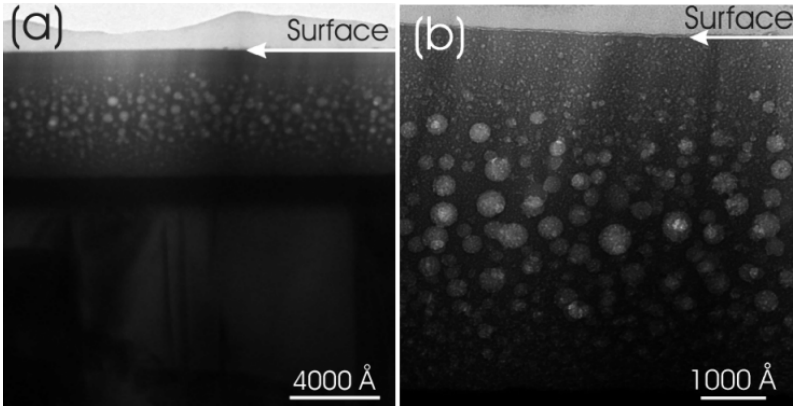

Figure 4.3: Bright-field XTEM images of the GaN epilayer bombarded with 2 MeV Au ions at LN_2 to a dose of 1×10^{16} cm^{-2} with a beam flux of 5×10^{12} cm^{-2} s^{-1}. Images (a) and (b) have been taken using different magnification.

those required for amorphization in the GaN bulk may be partly attributed to the swelling caused by the formation of a thin surface amorphous layer. As discussed in Chapter 3, the origin of this thin surface amorphous layer, observed by XTEM and RBS/C, is attributed to the trapping of migrating point defects by the GaN surface or amorphous/crystalline interface.

With increasing ion dose, implantation causes large-scale surface roughness only when buried and surface amorphous layers [as illustrated in Fig. 4.5(a)] meet each other, resulting in a continuous, thick layer of an amorphous material [as shown in Figs. 4.5(b) and 4.5(c)]. Further ion bombardment to doses above $\sim 3.5 \times 10^{16}$ cm^{-2} results in the formation of craters on the sample surface. Such an evolution of surface morphology in GaN under high-dose ion implantation is illustrated in Fig. 4.4. This figure shows AFM images of virgin GaN [Fig. 4.4(a)] and of GaN bombarded with 2 MeV Au ions at LN_2 to doses of 1×10^{16} [Fig. 4.4(b)] and 4×10^{16} cm^{-2} [Fig. 4.4(c)]. It is seen from this figure that high-dose heavy-ion bombardment dramatically changes the surface roughness of GaN.

The above evolution of the surface morphology with increasing ion dose may be explained as follows. Material swelling in the direction perpendicular to the sample surface is a direct consequence of ion-beam-induced porosity of amorphous GaN, while large-scale surface roughness (see Figs. 4.1 and 4.4) reflects the relief of stress associated with lateral expansion of the amorphized GaN film. In the case when two amorphous layers are formed [as illustrated in Fig. 4.5(a)], a stiff layer of crystalline GaN separating these two amorphous layers prevents film deformation and, therefore, prevents the appearance of large-scale surface roughness. Finally, surface craters observed on samples implanted to high ion doses ($\geq 3.5 \times 10^{16}$ cm^{-2}), as shown in Fig. 4.4(c), may be formed when voids/bubbles increase in size and intersect the surface.

It should be noted that similar porous structures have also been observed in GaN films amorphized by 300 keV Au ion bombardment. However, in this latter case of keV heavy-ion bombardment, the ion penetration depth is significantly smaller than that in the case of MeV ion irradiation, which makes the material swelling less pronounced. A combination of XTEM, RBS/C, and AFM data shows that ion-beam-induced volume expansion of amorphous GaN is close to 50%.

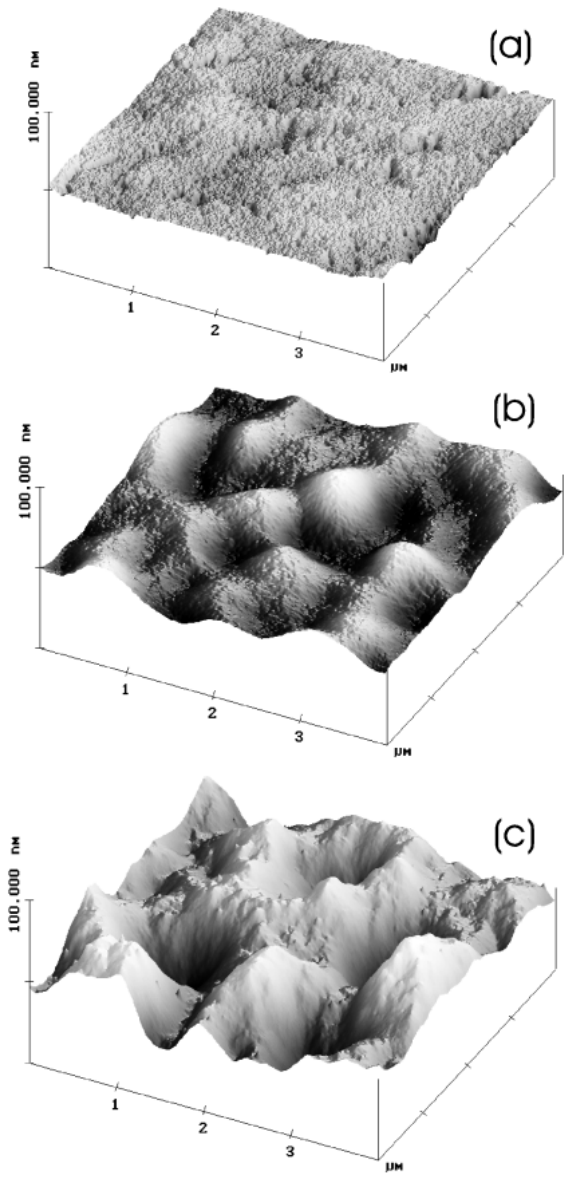

Figure 4.4: Height-mode AFM images of virgin GaN (a) and of GaN bombarded with 2 MeV Au ions at LN_2 with a beam flux of 5×10^{12} $cm^{-2}s^{-1}$ to doses of 1×10^{16} (b) and 4×10^{16} cm^{-2} (c).

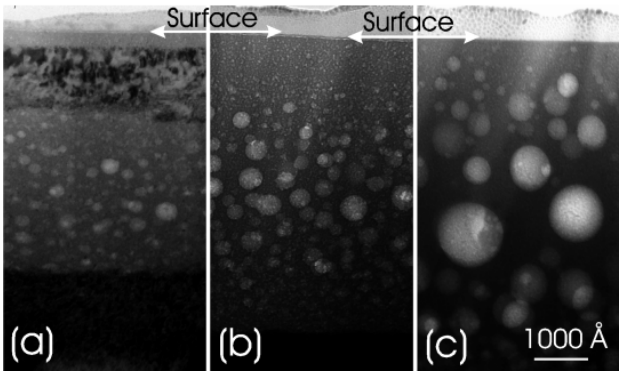

Figure 4.5: Bright-field XTEM images of GaN bombarded with 2 MeV Au ions at LN_2 with a beam flux of 5×10^{12} cm^{-2}s^{-1} to doses of 5×10^{15} (a), 1×10^{16} (b), and 3×10^{16} cm^{-2} (c). All three images are of the same magnification.

4.4 Voids or gas bubbles?

The effects of ion-beam-induced porosity and concomitant material expansion shown above are, in fact, not new. Similar effects have been observed in some other semiconductors, such as Ge [79,80], InSb [81], and GaSb [82]. In general, amorphousness is not necessarily the final state of a semiconductor exposed to ion bombardment. Although studied in some detail (particularly in the case of Ge [80]), ion-beam-induced formation and evolution of porous structures in amorphous materials are not well understood. One of the possible explanations for this effect is energetically favorable agglomeration of vacancy-like defects, generated by an ion beam in an amorphous matrix, resulting in the formation of voids [79, 80, 83]. However, in the case of GaN, the porosity revealed in this study may be also stimulated by ion-beam-induced material decomposition with the formation of N_2 gas bubbles in a Ga-rich matrix, a process which is discussed in more detail below.

Shown in Fig. 4.5 are bright-field XTEM images of GaN bombarded with 2 MeV Au ions at LN_2 to three different doses. Note that all three images were taken with the same magnification. The XTEM image from Fig. 4.5(a) (a dose of 5×10^{15} cm^{-2}) clearly shows two amorphous layers — surface and buried amorphous layers — separated by a layer of a heavily damaged but still crystalline material. The images from Figs. 4.5(b) and 4.5(c), which are for higher ion doses (doses of 1×10^{16} and 3×10^{16} cm^{-2}, respectively), reveal that ion bombardment to these doses results in the formation of continuous thick (surface) amorphous layers. Our detailed XTEM and electron diffraction investigation shows that

these layers are completely amorphous. A comparison of Figs. 4.5(a), 4.5(b), and 4.5(c) indicates that, with increasing ion dose, the size of the voids/bubbles also increases. In addition, these voids/bubbles remain close-to-spherical in shape. Figure 4.5 also suggests that small voids/bubbles agglomerate into larger ones with increasing ion dose.

The evolution of the porous structure with increasing ion dose, as studied by XTEM (see Fig. 4.5), suggests that this phenomenon may be attributed to the formation of gas bubbles in an amorphous GaN matrix. Indeed, as studied in the cases of ion-beam-induced porosity of Ge, InSb, and GaSb [80–82], the evolution of *voids,* with increasing ion dose, proceeds via the formation of a sponge-like structure with voids having an elongated, irregular shape. For example, the voids in Ge appear to repel each other as they increase in size [80]. In our case of GaN, the voids/bubbles are spherical in shape for a wide range of ion doses (see Fig. 4.5), which is typical for the case of the formation of gas bubbles.

The conclusion that the porous structure of amorphous GaN is a result of the formation of gas bubbles (not voids) is also supported by the annealing behavior of porous GaN. Figure 4.6(a) shows a typical top-view AFM image of GaN amorphized with 2 MeV Au ions (a dose of 1.2×10^{16} cm^{-2}) at LN_2 and subsequently annealed for 10 minutes at 450 °C in a N_2 atmosphere. This AFM image illustrates the formation of large craters on the surface as a result of decomposition of porous GaN. These craters are $\sim 2.0 - 2.5$ μm in diameter and ~ 0.2 μm deep. As expected, the depth of the craters is within the thickness of the GaN layer amorphized by ion implantation. This thermally-induced decomposition of GaN amorphized by heavy-ion bombardment occurs at annealing temperatures above about 400 °C. We attribute the formation of such craters to thermally-induced agglomeration of implantation-produced gas bubbles into larger bubbles with subsequent surface exfoliation.

Evidence for the formation of gas bubbles (not voids) is also given by our RBS/C data shown in Chapter 3. Indeed, RBS spectra taken from GaN amorphized by heavy ions [see, for example, Figs. 3.18(a), 3.24(a), and 3.27] have a "shoulder" with a decreased RBS yield in the ion end-of-range region (a region with large bubbles) and an increased yield near the GaN surface (presumably, a Ga-rich region). If a porous layer had voids (not bubbles), no "shoulder" in the RBS spectra would be expected [12].

Finally, Fig. 4.6(b) shows a *typical* bright-field XTEM image of a GaN sample preamorphized with 0.9 MeV $^{197}Au^+$ ions implanted at LN_2 to a dose of 2×10^{15} cm^{-2} with a beam flux of 1.3×10^{13} cm^{-2}s^{-1} and then with 0.45 MeV $^{197}Au^+$ ions at 0 °C to a dose

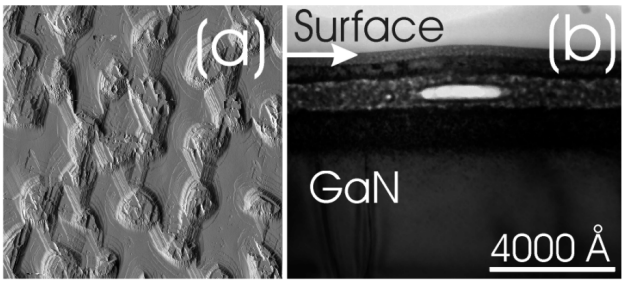

Figure 4.6: (a) Typical top-view amplitude-mode AFM image of GaN bombarded with 2 MeV Au ions at LN_2 to a dose of 1.2×10^{16} cm^{-2} with a beam flux of 5×10^{12} $cm^{-2}s^{-1}$ and subsequently annealed for 10 minutes at 450 °C in a N_2 atmosphere (horizontal field width is 15 μm). (b) Typical bright-field XTEM image of the GaN sample with surface and buried amorphous layers annealed in vacuum at 500 °C for $\sim$ 2 hours.

of 2×10^{15} cm^{-2} with a beam flux of 6.3×10^{12} $cm^{-2}s^{-1}$ to produce surface and buried amorphous layers separated by a layer of a heavily damaged but still crystalline material. Subsequently, this sample was annealed in vacuum at 500 °C for $\sim$ 2 hours. The XTEM image from Fig. 4.6(b) illustrates thermally-induced formation of a large gas bubble inside a preamorphized GaN layer. Note that this gas bubble makes the GaN surface convex, which strongly suggests that this is not a void. In the case illustrated in Fig. 4.6(b), surface exfoliation and the formation of craters are suppressed by a stiff layer of crystalline GaN separating the surface and buried amorphous layers.

The above data strongly suggests that the porosity of GaN amorphized by heavy-ion ($^{197}Au^{+}$) bombardment is due to the formation of N_2 gas bubbles in an amorphous GaN matrix. We also expect the formation of Ga-rich regions. However, our XTEM study has not revealed any direct evidence of Ga precipitation.

4.5 Stoichiometric imbalance

The formation of N_2 gas bubbles may be explained by the well-known effect of ion-beam-induced stoichiometric imbalance (see, for example, Ref. [68]). Indeed, local stoichiometric imbalance in the collision cascade volume may produce an excess concentration of the heavier element at shallow depth, while the region at greater depth is enriched with atoms of the lighter element. This effect is greatest when the mass ratio of the constituent elements of the semiconductor is high, and when ion mass is large [68]. Therefore, for

the case of 2 MeV ^{197}Au ion bombardment of GaN — a material with a large difference in the masses of constituent elements (^{70}Ga and ^{14}N) — the effect of local stoichiometric imbalance can readily account for the formation of N_2 gas bubbles in a highly N-deficient GaN matrix.

However, the final stoichiometry after ion bombardment also depends on defect migration, not only on the ballistic collisional processes. The above data suggests that, before amorphization, stoichiometric disturbances in crystalline GaN are very effectively repaired via defect diffusion and dynamic annealing processes. Such a dynamic annealing has been shown to be extremely efficient in crystalline GaN (see Chapter 3). Ion-beam-induced stoichiometric disturbances become evident only after GaN is amorphized [see Fig. 4.5(a)].

4.6 Summary

In summary, structural studies reveal that heavy-ion bombardment of GaN causes amorphization and anomalous swelling of the implanted region as a result of the formation of a porous structure. Results strongly suggest that such a porous structure consists of N_2 gas bubbles embedded into a highly N-deficient amorphous GaN matrix. The evolution of the porous structure in amorphous GaN appears to be a result of stoichiometric imbalance where N- and Ga-rich regions are produced by ion bombardment. Prior to amorphization, ion bombardment does not produce a porous structure due to very efficient dynamic annealing processes in the crystalline phase. Finally, our results show that GaN amorphized by ion bombardment is thermally unstable and decomposes at temperatures above ~ 400 °C. An important implication of this study for the fabrication of GaN-based devices is that amorphization of GaN should be avoided during ion implantation.

Chapter 5

Effect of In and Al content on damage buildup in III-nitrides

5.1 Introduction

Ion-beam-damage processes in GaN have been discussed in detail in Chapter 3. In the present chapter, a study of the effect of In and Al content (x) on the buildup of structural damage in $In_xGa_{1-x}N$ and $Al_xGa_{1-x}N$ epilayers is presented. These materials ($In_xGa_{1-x}N$ and $Al_xGa_{1-x}N$) are of great importance for III-nitride technology because of their role as both active and cladding layers in optoelectronic devices [1–7]. A study of ion-beam-damage processes in III-nitrides as a function of In and Al content is crucial for the estimation and control of implantation-produced lattice disorder in InGaN/GaN and AlGaN/GaN heterostructures. Interestingly, our results show that an increase in x suppresses dynamic annealing processes and enhances the accumulation of stable lattice damage in $In_xGa_{1-x}N$ during ion bombardment. In contrast, an increase in Al concentration strongly enhances dynamic annealing processes and, hence, suppresses the production of stable lattice disorder in AlGaN under ion bombardment. Finally, in Sect. 5.5, we present a study of structural characteristics of single-crystal AlN epilayers, which is the limiting case of AlGaN with large Al content. Results show that, due to extremely strong dynamic annealing processes, the AlN lattice cannot be rendered amorphous even for very large doses of keV heavy ions implanted at liquid nitrogen temperature (LN_2). For clarity, in this chapter, we combine results and discussion in each particular section.

5.2 Experimental

In this study, we used (i) $\sim$ 0.14-μm-thick single-crystal $In_xGa_{1-x}N$ films (x = 0.00, 0.03, 0.07, 0.12, 0.16, 0.18, and 0.20, with $\Delta x = 0.01$) on the top of $\sim$ 2-μm-thick wurtzite undoped GaN epilayers grown on c-plane sapphire substrates, (ii) $\sim$ 0.5-μm-thick $Al_xGa_{1-x}N$ films (x = 0.00, 0.05, 0.08, 0.10, 0.19, 0.40, and 0.60, with $\Delta x = 0.02$) on the top of $\sim$ 1-μm-thick wurtzite undoped GaN epilayers grown on c-plane sapphire substrates, and (iii) $\sim$ 0.2-μm-thick AlN films (with a concentration of Ga impurity of $\leq$ 1 at. % introduced during growth, as assessed by Rutherford backscattering) grown on c-plane sapphire substrates by MOCVD.

All implantation experiments presented in this chapter were carried out over a wide dose range with 300 keV ^{197}Au ions at LN_2 and room temperature (RT). After implantation, InGaN samples were characterized *ex-situ* by Rutherford backscattering/channeling

(RBS/C) spectrometry with 1.8 MeV $^4He^+$ or 3.3 MeV $^4He^+$ ions incident along the [0001] direction and backscattered into detectors at 98° and 110° relative to the incident beam direction. The 8° glancing-angle detector geometry with a 1.8 MeV $^4He^+$ ion beam was again used to provide enhanced depth resolution for examining near-surface damage accumulation, while the 20° glancing-angle detector geometry with 3.3 MeV $^4He^+$ ions was used to separate In and Ga peaks in the RBS/C spectra to study the accumulation of In and Ga displaced atoms separately. RBS/C spectra acquired from InGaN using 3.3 MeV He ions were analyzed using one of the conventional algorithms [61] for extracting depth-profiles of the effective number of scattering centers. For brevity, such a number of scattering centers, normalized to the atomic concentration, will be referred to below as "relative disorder."

After implantation, AlGaN samples were characterized by RBS/C with 1.8 MeV $^4He^+$ ions incident along the [0001] direction and backscattered into detectors at 98°, 115°, and $\sim 168°$ relative to the incident beam direction. The 8° glancing-angle detector geometry was used to provide enhanced depth resolution for examining near-surface damage accumulation. Scattering geometries with larger glancing angles were used to separate Au and Ga peaks in RBS/C spectra in samples implanted up to high Au doses ($\geq 5 \times 10^{15}$ cm^{-2}).

All AlN samples after implantation were characterized by RBS/C with 1.8 MeV $^4He^+$ ions incident along the [0001] direction and backscattered into a detector at 105° relative to the incident beam direction. This 15° glancing-angle detector geometry was used to provide enhanced depth resolution for examining damage accumulation in relatively thin AlN films and also to separate Au and Al peaks in RBS/C spectra in samples implanted up to high Au doses ($\geq 5 \times 10^{15}$ cm^{-2}). All ballistic calculations of ion-beam-produced atomic displacements in AlN, presented in Sect. 5.5, have been done with the TRIM code [22], with an effective threshold energy (E_d) for atomic displacements of 25 eV for both Al and N sublattices. It should be noted that we are not aware of any experimental measurements of E_d for AlN. The value of $E_d = 25$ eV, chosen in this work, is close to the value predicted by semi-empirical calculations of Van Vechten [84]. Quoted dpa values are the number of ion-beam-generated lattice vacancies.

Selected InGaN, AlGaN, and AlN samples were also studied with cross-sectional transmission electron microscopy (XTEM).

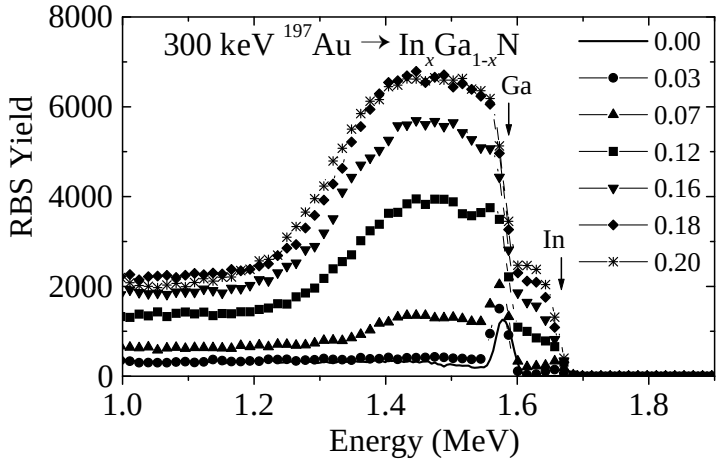

Figure 5.1: RBS/C spectra (acquired using 1.8 MeV He ions) illustrating lattice damage in $In_xGa_{1-x}N$ films bombarded at 20 °C with 300 keV Au ions to a dose of 4×10^{13} cm^{-2} with a beam flux of $\sim 3.1 \times 10^{12}$ cm^{-2} s^{-1}. Indium content (x) in different samples is indicated in the legend. The positions of the surface peaks of In and Ga are shown by arrows.

5.3 Damage in InGaN

Figure 5.1 shows RBS/C spectra illustrating lattice damage in $In_xGa_{1-x}N$ films bombarded at 20 °C with 300 keV Au ions to a dose of 4×10^{13} cm^{-2}. It is clearly seen from Fig. 5.1 that the level of implantation-produced lattice damage increases with increasing In concentration. It should be noted that, for a given dose, an increase in relative disorder with increasing In content is actually larger than that suggested by Fig. 5.1 because the RBS random level of Ga (which is used to normalize damage) decreases with increasing In concentration. Figure 5.1 also shows that the damage buildup in InGaN does not result in a bimodal distribution with a strong surface disorder peak, in contrast to the situation for GaN discussed in Chapter 3. Indeed, even in the sample with the lowest In concentration studied ($In_{0.03}Ga_{0.97}N$), surface disordering is not strong.[1]

[1]It should be noted that somewhat pronounced surface defect peaks observed in RBS/C spectra of $In_{0.03}Ga_{0.97}N$ and $In_{0.07}Ga_{0.93}N$ samples shown in Fig. 5.1 are most likely due to an overlap of ion-beam-produced bulk and intrinsic (i.e., present in as-grown samples) surface RBS/C peaks. Indeed, for larger ion doses and, hence, for higher levels of lattice disorder, no preferential surface disordering has been revealed, and RBS/C spectra are unimodal even for samples with low In content.

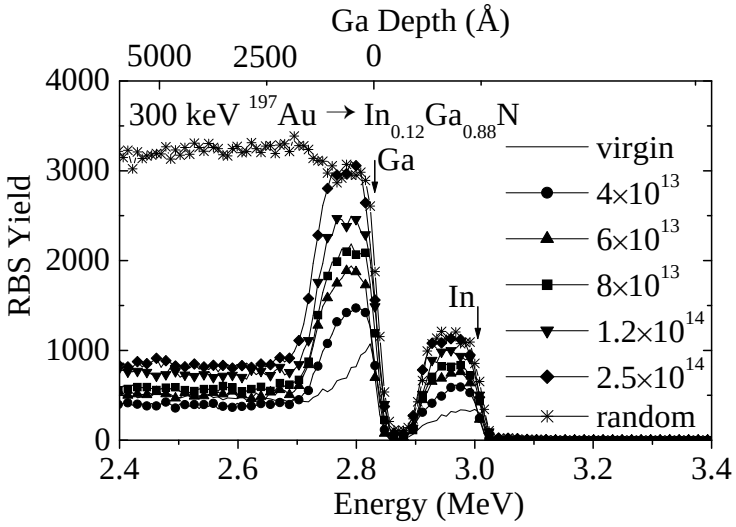

Figure 5.2: RBS/C spectra (acquired using 3.3 MeV He ions) showing the damage buildup for 300 keV Au ion bombardment of $In_{0.12}Ga_{0.88}N$ at 20 °C with a beam flux of $\sim 3.1 \times 10^{12}$ cm^{-2} s^{-1}. Implantation doses (in cm^{-2}) are indicated in the figure. The positions of the surface peaks of In and Ga are shown by arrows.

Typical RBS/C spectra illustrating the buildup of lattice disorder in $In_xGa_{1-x}N$ with increasing dose of 300 keV Au ions at 20 °C are shown in Fig. 5.2 for the case of $x = 0.12$. In these spectra, acquired using 3.3 MeV He ions, the Ga and In peaks are well separated, which allows the accumulation of Ga and In displaced atoms to be monitored separately. Figure 5.2 shows that, with increasing ion dose, the number of In and Ga displaced atoms accumulates at similar rates for both species. Moreover, an analysis of RBS/C data reveals that, in all InGaN samples studied, this accumulation of Ga and In disorder proceeds at essentially the same rate. Indeed, for a given dose, RBS/C yields (normalized to random levels) for Ga and In peaks are the same (within experimental error) in all InGaN samples studied. Hence, the reduced efficiency of dynamic annealing in InGaN appears to be not caused by reduced effective diffusivities of only Ga or In interstitials.

Figure 5.3 summarizes RBS/C data for all samples studied, showing the dose dependence of relative disorder (extracted from RBS/C data for the Ga peak) at depths corresponding to the bulk defect peak region for $In_xGa_{1-x}N$ samples with different x bombarded with 300 keV Au ions at 20 °C. It is clearly seen from Fig. 5.3 that an increase in In concentration strongly enhances implantation-produced disorder. For example, Fig. 5.3 shows that, for a dose of 4×10^{13} cm^{-2}, the level of relative disorder in $In_xGa_{1-x}N$ samples

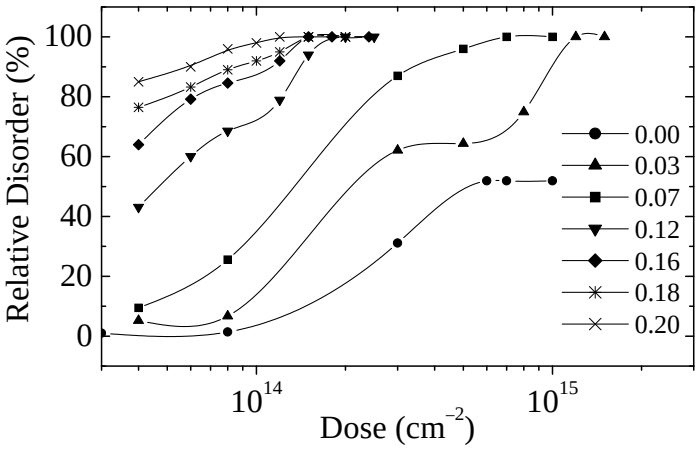

Figure 5.3: Dose dependence of relative disorder (extracted from RBS/C data for the Ga peak) in the bulk defect peak region for $In_xGa_{1-x}N$ samples bombarded with 300 keV Au ions at 20 °C with a beam flux of $\sim 3.1 \times 10^{12}$ cm^{-2} s^{-1}. Indium content (x) in different samples is given in the legend.

dramatically increases from ~ 2 to $\sim 85\%$ with increasing x from 0.0 to 0.2. This behavior is consistent with a previous report comparing the degree of dynamic annealing in different semiconductors, including GaN and InN [25]. In addition, Fig. 5.3 reveals that an increase in In concentration apparently suppresses the effect of damage saturation in the crystal bulk. Such defect saturation is very pronounced in GaN under heavy-ion bombardment at RT (see Chapter 3). Figure 5.3, however, shows that the effect of damage saturation is significantly less pronounced in InGaN samples, with apparent saturation levels increasing with an increase in x.

In selected samples, ion-beam-produced defects have been studied by XTEM. Figures 5.4(a) and 5.4(b) show dark-field XTEM images of $In_{0.16}Ga_{0.84}N$ implanted at 20 °C with 300 keV Au ions to a dose of 4×10^{13} cm^{-2}. These XTEM images reveal that defect structures in ion-implanted InGaN appear to be similar to those in GaN bombarded with heavy ions (see Chapter 3). Indeed, some coarse defect clusters [see Fig. 5.4(a)] and a band of extended (planar) defects [see Fig. 5.4(b)] are observed in ion-implanted InGaN. However, Fig. 5.4(b) shows that, in the case of InGaN, implantation-produced planar defects seem to be coarser and less regular than those in ion implanted GaN, discussed in Chapter 3. This observation is consistent with the fact that, as discussed above, dynamic

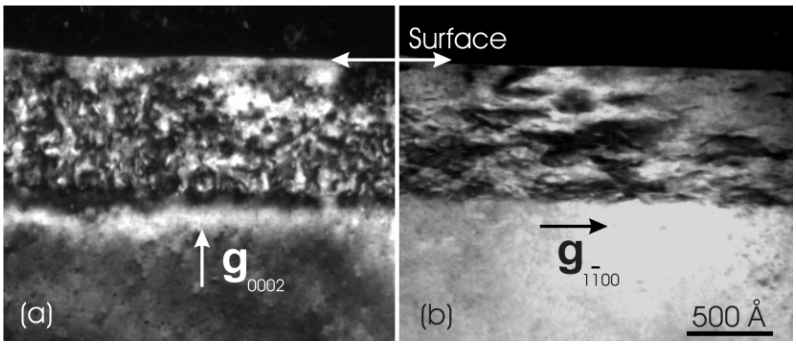

Figure 5.4: Dark-field XTEM images [(a) $\mathbf{g} = 0002^*$ and (b) $\mathbf{g} = 1\bar{1}00^*$] of an $In_{0.16}Ga_{0.84}N$ epilayer bombarded at 20 °C with 300 keV Au ions with a beam flux of $\sim 3.1 \times 10^{12}$ cm^{-2} s^{-1} to a dose of 4×10^{13} cm^{-2}. Images (a) and (b) are of the same magnification.

annealing processes in InGaN are suppressed as compared to those in GaN. Indeed, it is dynamic annealing which is responsible for the formation of extended defects *during* ion bombardment.

It is also interesting that a rather sharp border of implantation-produced damage is seen in Fig. 5.4, where extended defects are observed only within the top InGaN film, while the underlying GaN epilayer is free from such extended defects. This is also consistent with the fact that dynamic annealing processes in GaN are extremely efficient, which results in a considerably lower level of lattice disorder in GaN as compared to that in InGaN.

Finally, Figs. 5.5(a) and 5.5(b) show bright-field and dark-field XTEM images of an $In_{0.18}Ga_{0.82}N$ film implanted at 20 °C with 300 keV Au ions to a dose of 2×10^{14} cm^{-2}. These images clearly illustrate that, even in the case of relatively high dose ion bombardment, when the RBS/C yield reaches the random level (see Fig. 5.3), the implanted InGaN film may not be completely disordered (i.e., amorphous). Rather, XTEM strongly suggests that the $In_{0.18}Ga_{0.82}N$ film shown in Fig. 5.5 consists of amorphous regions embedded into a heavily damaged (but still crystalline) matrix. Hence, under heavy-ion bombardment at RT, the amorphization behavior of InGaN is markedly different from that of GaN. Indeed, in GaN, under RT heavy-ion bombardment, amorphization proceeds layer-by-layer from the surface (see Chapter 3). It should be noted that amorphization which proceeds via the formation of amorphous regions embedded into a heavily damaged crystalline matrix (such as shown in Fig. 5.5) is typical for materials in which dynamic annealing, although being present, is not significant compared with the rate of accumulation of stable lattice disorder (see, for example, Ref. [69]).

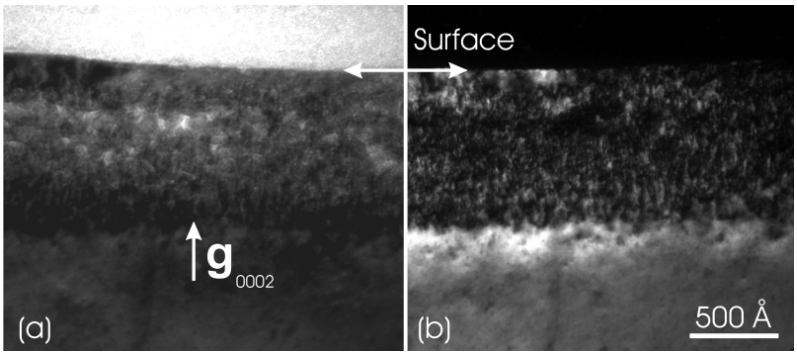

Figure 5.5: Bright-field (a) and dark-field (b) XTEM images ($\mathbf{g} = 0002^*$) of an $In_{0.18}Ga_{0.82}N$ epilayer bombarded at 20 °C with 300 keV Au ions with a beam flux of $\sim 3.1\times10^{12}$ cm^{-2} s^{-1} to a dose of 2×10^{14} cm^{-2}. Images (a) and (b) are of the same magnification.

5.4 Damage in AlGaN

Figure 5.6 shows selected RBS/C spectra illustrating the damage buildup in $Al_{0.08}Ga_{0.92}N$ films bombarded at 20 °C with 300 keV Au ions. It is seen from Fig. 5.6 that, with increasing ion dose up to $\sim 1\times10^{15}$ cm^{-2}, implantation-produced disorder in $Al_{0.08}Ga_{0.92}N$ accumulates mainly in the bulk region, where the nuclear energy loss profile of 300 keV Au ions has the maximum. Interestingly, no preferential surface disordering is observed in Fig. 5.6. For doses from $\sim 1\times10^{15}$ to $\sim 3\times10^{15}$ cm^{-2}, bulk disorder (as monitored by RBS/C) in $Al_{0.08}Ga_{0.92}N$ exhibits saturation, while the damage level in the near-surface region (between the sample surface and the bulk defect peak) grows up to the saturation level. Finally, with increasing ion dose above $\sim 3\times10^{15}$ cm^{-2}, lattice disorder in the $Al_{0.08}Ga_{0.92}N$ bulk rapidly increases to the random level, suggesting amorphization of the lattice.

It should be emphasized that the main features of the damage buildup behavior illustrated in Fig. 5.6 and discussed above for $Al_{0.08}Ga_{0.92}N$ are common for all $Al_xGa_{1-x}N$ wafers studied (with $x = 0.05-0.60$). These features are (i) damage saturation in the bulk, (ii) the *absence* of preferential surface disordering, and (iii) apparent rapid amorphization in the bulk from a saturation damage level above a critical dose.

The absence of preferential surface disordering revealed in AlGaN is somewhat surprising. Indeed, results presented in Chapter 3 have shown that the GaN surface (or the amorphous/crystalline interface) acts as a strong preferential site for amorphization. As a result, during heavy-ion bombardment of GaN at RT, amorphization proceeds layer-

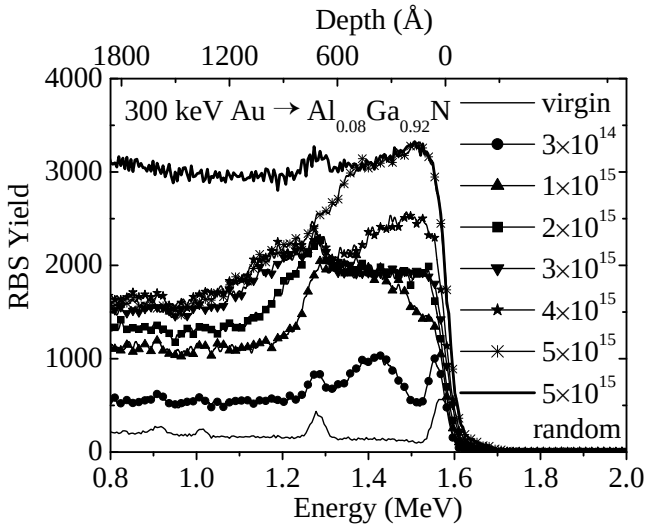

Figure 5.6: RBS/C spectra showing the damage buildup for 300 keV Au ion bombardment of $Al_{0.08}Ga_{0.92}N$ at 20 °C with a beam flux of $\sim 3.1 \times 10^{12}$ cm^{-2} s^{-1}. Implantation doses (in cm^{-2}) are indicated in the figure. Note that the random spectrum is given for an ion dose of 5×10^{15} cm^{-2}.

by-layer only from the GaN surface. In contrast, results presented in this chapter show that amorphization of $Al_xGa_{1-x}N$ (with $x = 0.05 - 0.60$) during heavy-ion bombardment at RT occurs spontaneously in the bulk, rather than proceeding layer-by-layer from the surface as in the case of GaN. Indeed, similar to the situation in GaN, XTEM reveals the formation of buried amorphous layers (rather than surface amorphous layers) in AlGaN above a critical dose, which increases with increasing Al content. This gives a compelling argument that the AlGaN surface is not a preferential nucleation site for amorphization.

To illustrate the influence of Al content on dynamic annealing processes in $Al_xGa_{1-x}N$, Fig. 5.7 summarizes RBS/C data for all samples studied, showing the dose dependence of maximum relative disorder (extracted from RBS/C spectra) at depths corresponding to the bulk defect peak region for $Al_xGa_{1-x}N$ samples bombarded with 300 keV Au ions at 20 °C. It is clearly seen from Fig. 5.7 that an increase in Al concentration dramatically enhances dynamic annealing processes and, hence, reduces implantation-produced disorder. For example, Fig. 5.7 shows that, for a dose of 6×10^{14} cm^{-2}, the level of relative disorder in the bulk in $Al_xGa_{1-x}N$ samples dramatically decreases from $\sim$ 51% (corresponding to the saturation level) to $\sim$ 4% with increasing x from 0.0 to 0.6. This behavior is consistent with a previous report comparing the degree of dynamic annealing in different

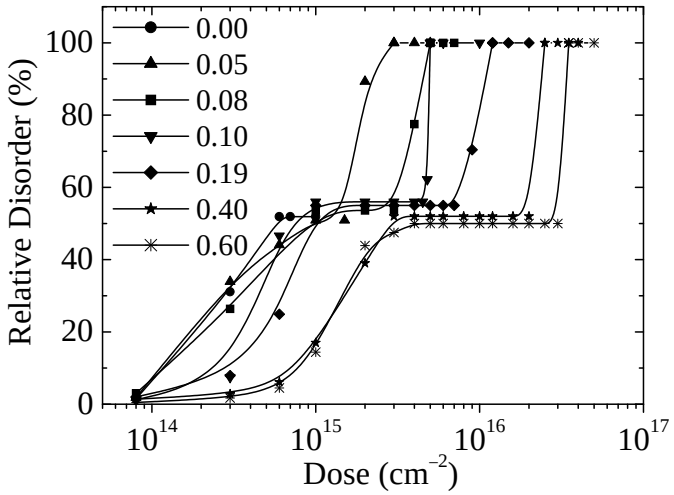

Figure 5.7: The dose dependence of maximum relative disorder (extracted from RBS/C spectra) in the bulk defect peak region for $Al_xGa_{1-x}N$ samples bombarded with 300 keV Au ions at 20 °C with a beam flux of $\sim 3.1 \times 10^{12}$ cm^{-2} s^{-1}. Aluminum content (x) in different samples is given in the legend. Lines are shown to guide the reader's eye.

semiconductors, including GaN, AlN, and InN [25].

Figure 5.7 also shows that all AlGaN wafers studied exhibit damage saturation in the crystal bulk for high ion doses. Interestingly, the disorder level in the saturation regime is essentially independent of Al content (within experimental error). This result may suggest that similar defect structures are present in $Al_xGa_{1-x}N$ crystals (with $x = 0.0 - 0.6$) in the saturation regime when processes of local defect generation and dynamic annealing are balanced.

In selected AlGaN samples, the microstructure of preamorphous lattice disorder has been studied by XTEM. Figures 5.8(a) and 5.8(b) show dark-field XTEM images of $Al_{0.08}Ga_{0.92}N$ implanted at 20 °C with 300 keV Au ions to a dose of 4×10^{15} cm^{-2}. In addition, Figs. 5.8(c) and 5.8(d) show dark-field XTEM images of lattice defects produced in an $Al_{0.19}Ga_{0.81}N$ film bombarded at 20 °C with 300 keV Au ions to a dose of 9×10^{15} cm^{-2}. As is clearly seen from Figs. 5.6 and 5.7, for such doses of 4×10^{15} cm^{-2} (for $Al_{0.08}Ga_{0.92}N$) and 9×10^{15} cm^{-2} (for $Al_{0.19}Ga_{0.81}N$), the damage level in the AlGaN bulk is slightly above the saturation level. XTEM images from Fig. 5.8 reveal that defect structures in ion-implanted AlGaN are similar to those in GaN and InGaN bombarded

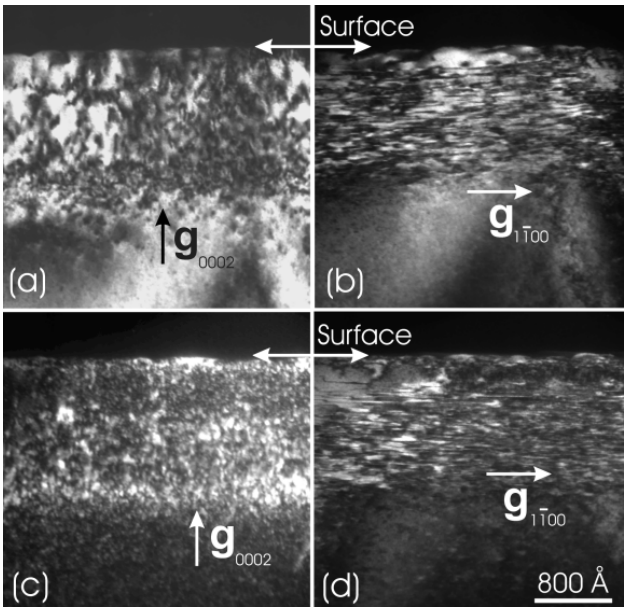

Figure 5.8: Dark-field XTEM images [(a),(c) $\mathbf{g} = 0002^*$ and (b),(d) $\mathbf{g} = 1\bar{1}00^*$] of $Al_{0.08}Ga_{0.92}N$ [(a),(b)] and $Al_{0.19}Ga_{0.81}N$ [(c),(d)] epilayers bombarded at 20 °C with 300 keV Au ions with a beam flux of $\sim 3.1 \times 10^{12}$ cm^{-2} s^{-1} to doses of 4×10^{15} [(a),(b)] and 9×10^{15} cm^{-2} [(c),(d)]. All images are of the same magnification.

with heavy ions, discussed in Chapter 3 and Sect. 5.3, respectively. Indeed, some coarse defect clusters [see Figs. 5.8(a) and 5.8(c)] and a band of extended (planar) defects [see Figs. 5.8(b) and 5.8(d)] are observed in ion-implanted AlGaN, which is similar to the situation in GaN and InGaN.

An analysis of Fig. 5.8 also reveals that, in the near-surface region (around $\sim$ 400 Å from the AlGaN surface) where the RBS/C yield increases above the saturation level, implantation-produced defect structures appear to be denser and less regular. This is due to imperfect dynamic annealing when, despite extremely effective defect annihilation processes in AlGaN, some defects survive annihilation and buildup in the lattice. For high ion doses, the free energy of the ion-beam-damaged lattice can exceed the free energy of the amorphous phase, which makes the process of amorphization energetically favorable. A further increase in ion dose results in a rapid (nucleation-limited) amorphization of the lattice, as clearly illustrated in Fig. 5.7.

5.5 Damage in AlN

5.5.1 Introduction

As has been shown in Sect. 5.4, disordering in $Al_xGa_{1-x}N$ (with $x \leq 0.6$), particularly the profile of structural disorder, is significantly different to that in GaN. Hence, it is important to extend the study to higher Al content, in particular to AlN, to indicate any anomalous disordering behavior that may occur. However, all previous reports on structural characteristics of irradiated AlN have focused on studies of lattice damage produced by bombardment with neutrons or relatively light ions at MeV energies such as 3 MeV Kr ions implanted at RT to a dose of 2×10^{17} cm^{-2} [85], 2 MeV Si ions implanted at -195 and 127 °C to a dose of 4×10^{16} cm^{-2} [86], and neutron bombardment at temperatures from 100 up to 785 °C [87,88]. It has been shown that, for these implant conditions, AlN does not exhibit amorphization even for relatively large ion/neutron doses [such as $\sim$ 320 displacements per atom (dpa) for 2×10^{17} cm^{-2} of 3 MeV Kr ions and $\sim$ 25 dpa for 4×10^{16} cm^{-2} of 2 MeV Si ions in the maximum of the nuclear energy loss profile]. Previous studies [86–88] have also revealed the formation of an aligned network of extended defects on the basal plane of AlN as a result of irradiation.

Studies of ion-beam-damage processes in GaN discussed in Chapter 3 have shown that, for conditions with strong dynamic annealing (as is the case for AlN at temperatures above, at least, LN_2 [85, 86, 88]), the density of collision cascades (determined by ion mass and energy) may strongly influence the damage accumulation behavior. It has also been shown in Chapter 3 that the sample surface can act as a nucleation site for amorphization and, hence, dramatically change the damage buildup behavior during ion irradiation. Furthermore, chemical effects of implanted species can strongly affect the formation of stable defect structures during dynamic annealing (see Sect. 3.5.6). Therefore, in addition to previous structural studies of AlN irradiated with neutrons or MeV (relatively) light ions [85–88], it is important to investigate damage processes and possible crystalline-to-amorphous phase transformations in AlN under bombardment with keV heavy ions, which produce dense collision cascades close to the sample surface. Such bombardment with keV heavy ions at low temperatures represents an irradiation regime when (i) ion-beam-damage-induced lattice amorphization is most plausible (due to very large density of collision cascades) and (ii) chemical effects of implanted species can be

less pronounced in cases of implantation with (relatively) chemically inactive species such as Au (see Sect. 3.5.6).

It should also be noted that all previous studies of irradiation-produced structural lattice damage in AlN have been done on a *polycrystalline* material analyzed by TEM [85–88]. However, in order to quantitatively study damage accumulation up to high levels of lattice disorder, other analytical methods, in addition to TEM, should be applied. RBS/C is a technique ideally suited to quantitatively study implantation-produced lattice disorder with high depth resolution. However, RBS/C typically requires a single-crystal material and, hence, has not been applied in previous studies of radiation effects in polycrystalline AlN ceramics.

Below, we study structural characteristics of single-crystal AlN bombarded with keV heavy ions (300 keV $^{197}Au^{+}$ ions) at RT and LN_2. We study the behavior of damage buildup and the microstructure of ion-beam-produced stable defects in AlN. Results reveal extremely strong dynamic annealing of ion-beam-generated defects in AlN, leading to the situation when lattice amorphization does not occur even for very large doses of keV Au ions at LN_2. Results also show that implantation-produced disorder in AlN is thermally stable up to relatively high temperatures (at least, 1000 °C).

5.5.2 Results and discussion

Figure 5.9 shows selected RBS/C spectra which illustrate the damage buildup (in the Al sublattice) in AlN films bombarded at −196 °C [Fig. 5.9(a)] and 20 °C [Fig. 5.9(b)] with 300 keV Au ions. It is seen from Fig. 5.9 that, with increasing ion dose for both LN_2 and RT bombardment regimes, implantation-produced lattice disorder accumulates mainly in the crystal bulk ($\sim$ 700 Å from the sample surface), close to the region where the nuclear energy loss profile of 300 keV Au ions is maximum. Interestingly, no preferential surface disordering has been observed in this study in AlN bombarded at either −196 °C or 20 °C.[2] This is consistent with results from Sect. 5.4, showing that the AlGaN surface is not a preferential site for amorphization, in contrast to the situation in GaN.

[2]It should be noted that a distorted shape of the RBS random spectra from Fig. 5.9 (i.e., a yield increase near the surface and a dip for larger Al depths) is due to (i) a large concentration of Au atoms implanted into the AlN lattice and (ii) an overlap of Al and Au peaks in the spectra for very large Au ion doses. Note that, for clarity, the Au peak is not shown in Fig. 5.9.

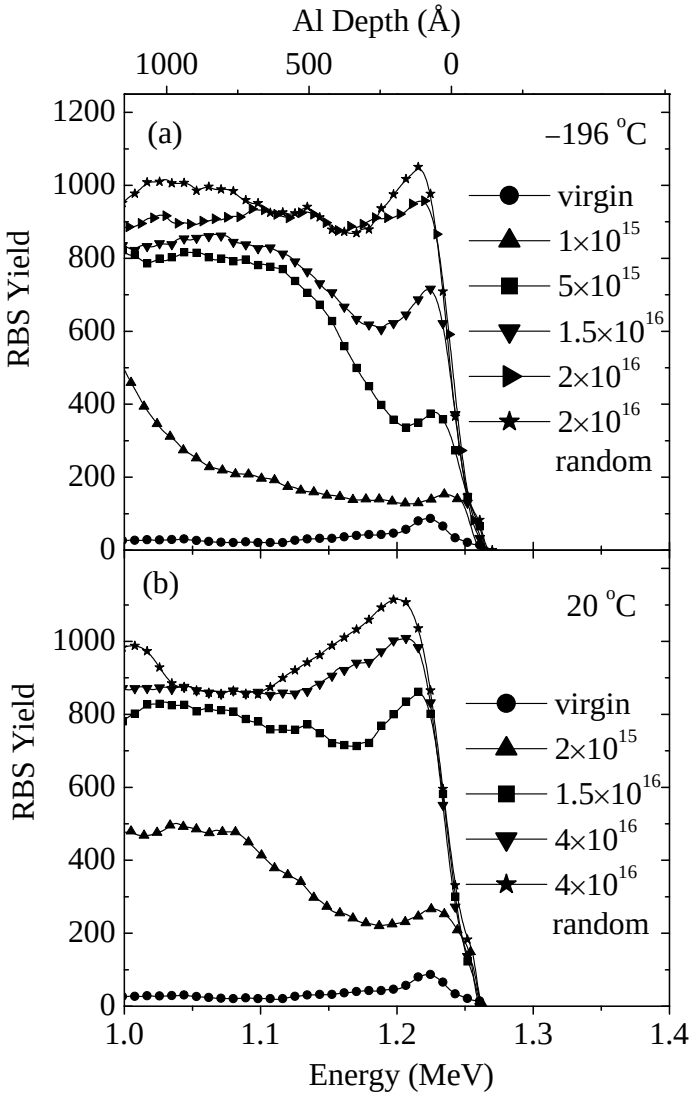

Figure 5.9: RBS/C spectra showing the damage buildup for 300 keV Au ion bombardment of AlN at −196 °C (a) and 20 °C (b) with a beam flux of $\sim 3.1\times10^{12}$ cm^{-2} s^{-1}. Implantation doses (in cm^{-2}) are indicated in the figure. Only the Al part of spectra is shown. Note that random spectra are given for ion doses of 2×10^{16} (a) and 4×10^{16} cm^{-2} (b).

The damage buildup behavior for heavy-ion bombardment at both −196 and 20 °C is better illustrated in Fig. 5.10, which shows the dose dependence of the RBS/C yield (normalized to the random level) in the bulk defect peak region for AlN samples bombarded with 300 keV Au ions. Figure 5.10 shows that bulk disorder in AlN gradually increases with increasing ion dose and approaches the random level (suggesting amorphization of the lattice) for ion doses above $\sim 2 \times 10^{16}$ cm^{-2} for both LN_2 and RT bombardment regimes. Interestingly, Fig. 5.10 shows that an increase in implantation temperature from −196 to 20 °C results in only a slight decrease in the level of stable ion-beam-produced lattice disorder. This result is consistent with previous electron paramagnetic resonance (EPR) studies of the effect of irradiation temperature on the damage accumulation in AlN ceramics bombarded with neutrons [89], where a very weak irradiation-temperature effect has been observed for temperatures from −248 up to −23 °C. Such a weak irradiation-temperature dependence of stable defect formation, revealed in both the present study of structural disorder and a previous report on irradiation-produced paramagnetic centers [89], suggests that the mobility and annihilation of ion-beam-generated Frenkel pairs in AlN is very large even at −196 °C and does not significantly increase upon increasing sample temperature up to 20 °C. However, as has been discussed in detail in Chapter 3, dynamic annealing processes in compound semiconductors may be very complex. At present, more work is needed for a better understanding of complex ion-beam-damage processes (such as defect mobility as well as interaction and annihilation of defects) in AlN.[3]

Another interesting feature illustrated in Fig. 5.10 is that, in contrast to the case of RT heavy-ion bombardment of $Al_xGa_{1-x}N$ with $x \leq 0.6$ discussed in Sect. 5.4, Fig. 5.10 reveals no damage saturation in the crystal bulk. Indeed, for $Al_xGa_{1-x}N$ with $x \leq 0.6$, with increasing ion dose, the level of implantation-produced lattice disorder in the crystal bulk increases up to $\sim$ 50% and then saturates (see Sect. 5.4). During this saturation

[3]Previous optical absorption and EPR studies of neutron-irradiated AlN ceramics [90, 91] have revealed an absorption band at $\sim$ 370 nm and an EPR center with $g = 2.007 \pm 0.001$ with similar annealing behavior. These EPR and optical absorption centers have tentatively been attributed to (isolated) nitrogen vacancies [90, 91]. However, more work is obviously needed to identify the origin of these signals. Indeed, given extremely strong dynamic annealing processes in AlN, the EPR and optical absorption bands observed in Refs. [90] and [91] more likely arise from defect-impurity complexes rather than from isolated vacancies or interstitials.

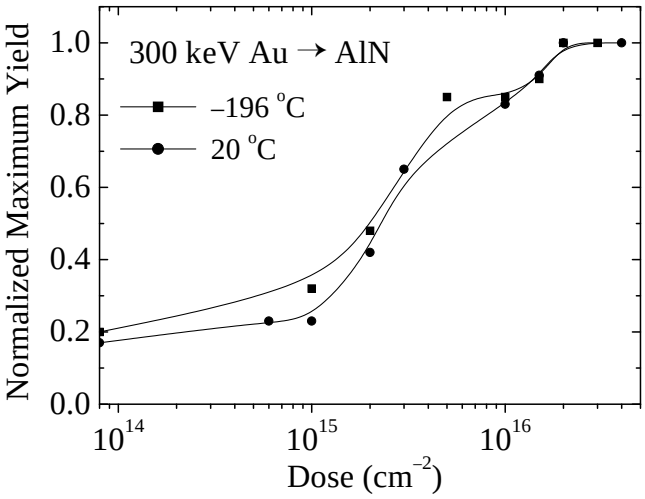

Figure 5.10: Dose dependence of the RBS/C yield (normalized to the random level) in the bulk defect peak region for AlN samples bombarded with 300 keV Au ions with a beam flux of $\sim 3.1 \times 10^{12}$ cm^{-2} s^{-1} at -196 and 20 °C, as indicated in the legend. Lines are shown to guide the reader's eye.

regime and before a catastrophic collapse of the lattice into an amorphous state, the level of lattice disorder in the $Al_xGa_{1-x}N$ bulk ($\sim 50\%$) is essentially independent of ion dose. Figures 5.9 and 5.10 reveal a rather different damage buildup bahavior in AlN.

The absence of such damage saturation in AlN suggests that the damage buildup in AlN proceeds via the formation of different types of lattice defects as compared to the case of AlGaN with lower Al content. Hence, in selected samples, the microstructure of implantation-produced disorder has been studied by XTEM. Figure 5.11 shows dark-field XTEM images of an AlN epilayer implanted at 20 °C with 300 keV Au ions to a dose of 4×10^{16} cm^{-2}. This figure illustrates that, even for a high ion dose when the RBS/C yield reaches the random level in the crystal bulk [see Fig. 5.9(b)], the AlN layer is heavily damaged but not amorphous.[4] Indeed, no evidence for an amorphous phase has been

[4]The fact that the RBS/C yield reaches the random level indicates the presence of a large concentration of lattice defects which effectively suppress ion channeling along the c-axis of the wurtzite structure of AlN. As is often the case in ion-implanted semiconductors, such apparent lattice randomization measured by RBS/C does not necessarily imply complete disordering or amorphization of the material (i.e., complete loss of long-range order), as clearly illustrated by a comparison of Figs. 5.9(b) and 5.11. A confirmation of the presence of an amorphous phase (using, for example, XTEM) is essential in studies of the amorphization behavior in ion-implanted solids.

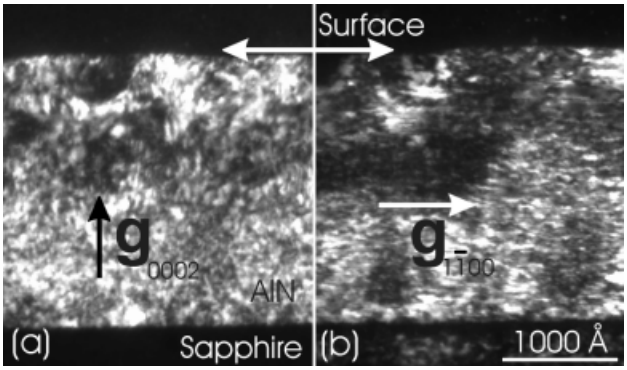

Figure 5.11: Dark-field XTEM images [(a) $\mathbf{g} = 0002^*$ and (b) $\mathbf{g} = 1\bar{1}00^*$] of an AlN epilayer bombarded at 20 °C with 300 keV Au ions with a beam flux of $\sim 3.1 \times 10^{12}$ cm^{-2} s^{-1} to a dose of 4×10^{16} cm^{-2}. Images (a) and (b) are of the same magnification.

revealed in this sample by an electron diffraction analysis. This result indicates extremely high radiation resistance of AlN and a large mobility of ion-beam-generated point defects, consistent with previous studies [25, 85, 86].

Figure 5.12 shows the evolution of microstructural changes in AlN bombarded at −196 °C with 300 keV Au ions to different doses. It is seen from Figs. 5.12(a) and 5.12(b) that, even for a relatively large dose of 5×10^{15} cm^{-2} of heavy ions, in the near-surface region (up to $\sim$ 500 Å from the sample surface), where the nuclear energy loss is relatively small, the density of ion-beam-produced defects is low. For larger depths, a dense band of coarse defects can be seen.[5] For the sample bombarded to a larger ion dose of 3×10^{16} cm^{-2}, Figs. 5.12(c) and 5.12(d) reveal a dense band of coarse lattice defects throughout the entire AlN film, with no evidence for amorphization. Hence, due to extremely large dynamic annealing processes, it appears to be impossible to induce lattice amorphization in AlN by keV ion bombardment at LN_2 and above.[6]

Finally, our results show that ion-beam-produced lattice disorder in AlN is particularly stable during rapid thermal annealing at temperatures as high as 1000 °C. Indeed, 1 min

[5]It should be noted that, in contrast to the case of previous TEM studies of AlN irradiated with MeV (relatively) light ions or neutrons [85–88], a detailed XTEM study of defects produced in AlN by high-dose keV heavy-ion bombardment (as shown in Figs. 5.11 and 5.12) was not feasible in the present work due to a high density of implantation-produced lattice defects. At present, more work is needed to reveal the atomic structure of defects produced in AlN by heavy-ion bombardment.

[6]It should be noted that ion-beam sputtering and chemical effects of implanted species hinder damage buildup and amorphization studies for larger ion doses than the doses used in this study.

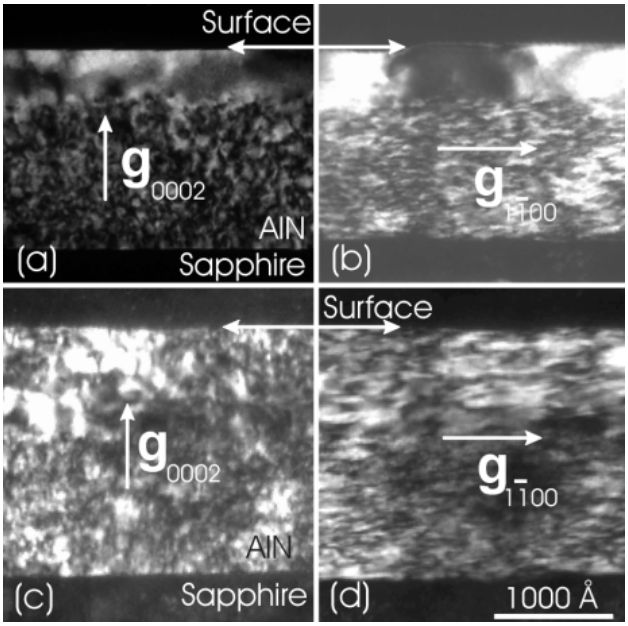

Figure 5.12: Dark-field XTEM images [(a),(c) $\mathbf{g} = 0002^*$ and (b),(d) $\mathbf{g} = 1\bar{1}00^*$] of AlN epilayers bombarded at -196 °C with 300 keV Au ions with a beam flux of $\sim 3.1 \times 10^{12}$ cm^{-2} s^{-1} to doses of 5×10^{15} cm^{-2} [(a) and (b)] and 3×10^{16} cm^{-2} [(c) and (d)]. All images are of the same magnification.

thermal annealing at 1000 °C (in a nitrogen ambient at atmospheric pressure) of samples bombarded with 300 keV Au ions at either -196 or 20 °C to doses $\geq 1 \times 10^{16}$ cm^{-2} results in a negligible ($\sim 5\%$) reduction in the RBS/C yield, indicating that ion-beam-produced disorder in AlN is not appreciably removed during such annealing. This annealing behavior is not unexpected since the extremely efficient dynamic annealing that occurs in AlN even at LN_2 causes ion-beam-generated Frenkel pairs either to efficiently annihilate or to form stable (energetically favorable) defect structures that accumulate with increasing ion dose. In such a case, one can expect that these complex defect structures will be thermally stable up to high temperatures in AlN. Indeed, as a general rule, temperatures of $\sim 2/3$ of the melting point (in K) are required to remove ion-beam-produced extended defects in semiconductors [9], suggesting that temperatures of ≥ 1900 °C may be needed to anneal out implantation-produced damage in AlN (see Table 1.1).

It should also be noted that previous studies of the annealing behavior of neutron-irradiated AlN ceramics by optical absorption [90], EPR [89, 91], and thermal diffusivity measurements [92] have shown that the annealing behavior of irradiated AlN ceramics largely depends on irradiation conditions such as ion dose and temperature. For example,

in AlN irradiated with neutrons to a relatively low dose of $\sim 10^{17}$ cm^{-2}, defects revealed by EPR and optical absorption measurements [90] show a one stage annealing behavior at temperatures around ~ 200 °C, but defects could not be completely removed even by anneals at 500 °C. Moreover, thermal diffusivity and macroscopic length change measurements of AlN irradiated to a larger neutron dose ($\sim 2 \times 10^{20}$ cm^{-2}) have shown that irradiation-produced disorder can not be completely recovered even during 1 hour thermal anneals at temperatures as high as ~ 1400 °C [92]. Hence, previous data also supports the above conclusion that large thermal budgets (with temperatures ≥ 1900 °C) may be necessary to completely remove complex defect structures in AlN crystals implanted to high ion doses.

5.6 Summary

In summary, the structural disorder produced in single-crystal InGaN, AlGaN, and AlN by keV heavy-ion bombardment has been studied by a combination of RBS/C and XTEM. Results show that an increase in In content (i) suppresses dynamic annealing processes, (ii) enhances the accumulation of stable lattice defects, and (iii) weakens the effect of damage saturation in the bulk during RT bombardment. In addition, we have found that, with increasing ion dose, the number of In and Ga displaced atoms accumulates at essentially the same rate (within experimental error).

In contrast to the effect of In, an increase in Al concentration strongly enhances dynamic annealing processes and, hence, suppresses the production of stable lattice disorder in AlGaN under ion bombardment. All AlGaN wafers studied have shown damage saturation in the bulk for high ion doses, with the disorder level in the saturation regime being essentially independent of Al content (within experimental error). The amorphization behavior of AlGaN is somewhat different from that in GaN. In particular, all $Al_xGa_{1-x}N$ wafers studied have exhibited no preferential surface disordering. Rather, a rapid transition from the saturation regime to nucleation-limited amorphization in the crystal bulk has been observed in AlGaN above a critical dose. Finally, XTEM has revealed similar defect structures in ion-implanted InGaN and AlGaN as compared to those in GaN. However, extended defects appear to be coarser and less regular in InGaN than those in GaN, which is consistent with a reduced level of dynamic annealing in InGaN.

Results have also shown that AlN exhibits extremely strong dynamic annealing of ion-beam-generated defects during ion bombardment at LN_2 and above. In particular, the AlN lattice is not rendered amorphous even for very large doses of keV heavy ions implanted at either -196 or 20 °C. Our results have also revealed neither damage saturation in the AlN crystal bulk [typical for $Al_xGa_{1-x}N$ with $x \leq 0.6$ (see Sect. 5.4)] nor preferential disordering at the AlN surface [typical for GaN (see Chapter 3)] for both LN_2 and RT bombardment regimes. Finally, this study also shows that implantation-produced lattice defects in AlN are stable up to high temperatures (at least, 1000 °C).

Chapter 6

Mechanical properties of ion-implanted GaN

6.1 Introduction

There is considerable interest in determining the mechanical properties of semiconductors. Indeed, studies of the processes controlling contact damage, wear, and cracking of semiconductor layers have significant technological importance. An accurate determination of the mechanical properties of semiconductors, however, requires a thorough understanding of the physical processes occurring during deformation. The deformation behavior of solids is determined by complex processes of the generation, propagation, and interaction of deformation-produced lattice defects.

Several studies (including our own) of the mechanical properties of as-grown single-crystal GaN have been reported in the literature (see, for example, Refs. [93, 94] and references therein). However, both elastic and plastic properties of GaN can be affected by the presence of different types of lattice defects. Hence, it is important to establish and understand the influence of pre-existing lattice defects on the deformation behavior of semiconductors.

As discussed in the previous chapters, bombardment with energetic ions inevitably produces lattice defects, which can affect all the properties of the material, including the mechanical properties. It is important to study the influence of implantation-produced lattice defects on the deformation behavior of GaN not only for the estimation of contact-induced damage in ion-beam-processed GaN but also for a better understanding of the evolution of the structural characteristics of GaN under ion bombardment. However, to our knowledge, the effects of implantation damage on the deformation behavior of GaN have not previously been studied. This is not surprising since damage processes in GaN exposed to ion bombardment have still not been well documented in the literature.

In this chapter, we present results on the mechanical properties of (i) crystalline GaN with a relatively high concentration of implantation-produced defects and (ii) GaN amorphized by ion bombardment. To understand the influence of implantation-produced defects on mechanical deformation in GaN, we use a combination of nanoindentation and atomic force microscopy (AFM) techniques. Results show that, unlike the situation for Si [95], implantation damage dramatically changes the deformation behavior of GaN.

Table 6.1: Implant conditions used to prepare the "ion-damaged" sample by multiple-energy bombardment with ^{197}Au ions at 300 °C.

Energy (MeV)	Dose (10^{14} cm^{-2})	Beam flux (10^{12} cm^{-2} s^{-1})
6.60	5	5.2
2.00	7	18
0.45	3	17

6.2 Experimental

All samples used in this study were cut from the same GaN wafer: an $\sim$ 2-μm-thick wurtzite undoped GaN epilayer grown on a *c*-plane sapphire substrate by MOCVD. For this indentation study, two samples were modified by ion bombardment: (i) a GaN sample with implantation-produced defects (referred to below as "ion-damaged" GaN) and (ii) GaN amorphized by ion implantation.

To prepare an amorphous layer, GaN was bombarded with 2 MeV $^{197}Au^{+}$ ions at liquid nitrogen temperature with a beam flux of 5×10^{12} cm^{-2} s^{-1} to a dose of 1.5×10^{16} cm^{-2}. Such implantation results in the formation of an $\sim$ 0.6-μm-thick, completely amorphous surface layer, as discussed in detail in Chapter 4. It should be noted that GaN amorphized by ion bombardment exhibits some degree of porosity (see Chapter 4), which may also affect the deformation behavior, as discussed below.

The "ion-damaged" sample, with a relatively high concentration of implantation-produced defects (but not amorphous), was prepared by multiple-energy bombardment with ^{197}Au ions at 300 °C. The implant conditions used to prepare this sample are given in Table 6.1. Such multiple-energy implantation at an elevated temperature results in the formation of lattice defects, including some planar defects, in the implanted layer (up to $\sim$ 1 μm from the surface). It should be noted that, for the ion doses used in this study, the concentration of implanted Au species (< 0.06 at.%) is expected to have a negligible effect on the mechanical properties of GaN. Rather, the deformation behavior of ion-beam-modified GaN should be determined by implantation-produced lattice disorder and its consequences.

6.3 Results and discussion

Figure 6.1 shows typical continuous load–unload force–displacement curves of as-grown [Fig. 6.1(a)], "ion-damaged" [Fig. 6.1(b)], and amorphized [Fig. 6.1(c)] GaN films. Figure 6.1(a) clearly illustrates a discontinuity (or "pop-in") of the yield response during loading of as-grown GaN. It is well known for other brittle materials that such discontinuities in the load–displacement curves represent the "fingerprints" of important physical processes occurring during deformation such as slip and/or pressure-induced phase transformations (see, for example, Ref. [96]). Interestingly, Fig. 6.1(b) reveals that in "ion-damaged" GaN, the "pop-in" event is still present but is significantly less pronounced than in as-grown GaN. Finally, Fig. 6.1(c) shows no discontinuities in the load–displacement curve of amorphous GaN, in full agreement with the expected deformation behavior of an amorphous solid [95].

Shown in Fig. 6.2 are typical amplitude-mode AFM images of as-grown [Fig. 6.2(a)] and "ion-damaged" [Fig. 6.2(b)] GaN films indented to a maximum load of 100 mN. These AFM images clearly illustrate that slip, which occurs during loading of as-grown GaN [93], is strongly suppressed in "ion-damaged" GaN. A comparison of nanoindentation data [see Figs. 6.1(a) and 6.1(b)] and AFM data (see Fig. 6.2) gives a compelling argument that slip nucleation (rather than a phase transformation) is the physical mechanism responsible for the "pop-in" events observed during loading of GaN.

Shown in Fig. 6.3 are the curves of the average contact pressure [or (Meyer) hardness], H, [Fig. 6.3(a)] and Young's modulus, E, [Fig. 6.3(b)] as a function of indenter penetration below the circle of contact, as determined from partial load–unload data. This figure, showing data for as-grown, "ion-damaged," and amorphized GaN, reveals that ion bombardment dramatically modifies H and E. It is seen that, for shallow penetration depths of the indenter (prior to the "pop-in" event), the H and E values of "ion-damaged" GaN are lower than those of as-grown material. As expected, the value of E is not affected by slip and remains essentially constant for the whole indenter penetration depth.[1] However, slip significantly affects H of as-grown GaN, while in "ion-damaged" GaN slip is strongly suppressed, and, for larger depths of indenter penetration, H becomes larger than that of

[1] A slightly non-constant behavior for E of "ion-damaged" GaN with increasing penetration depth [see Fig. 6.3(b)] may be attributed to a nonuniform distribution of implantation-produced disorder and/or to the influence of the underlying sapphire substrate at high loads.

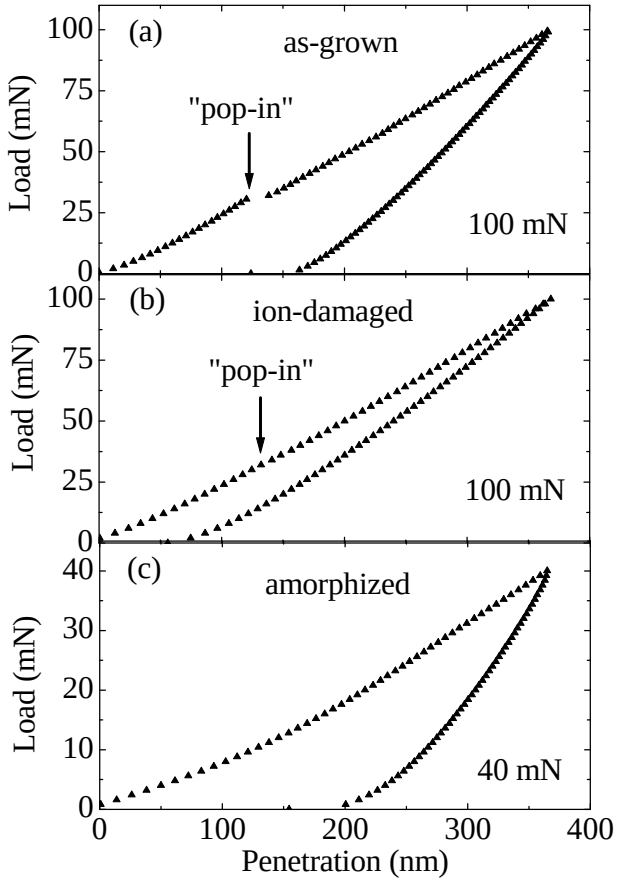

Figure 6.1: Typical continuous load–unload curves of (a) as-grown, (b) "ion-damaged," and (c) amorphized GaN films. Note that the maximum load is 100 mN for (a) and (b) and is 40 mN for (c).

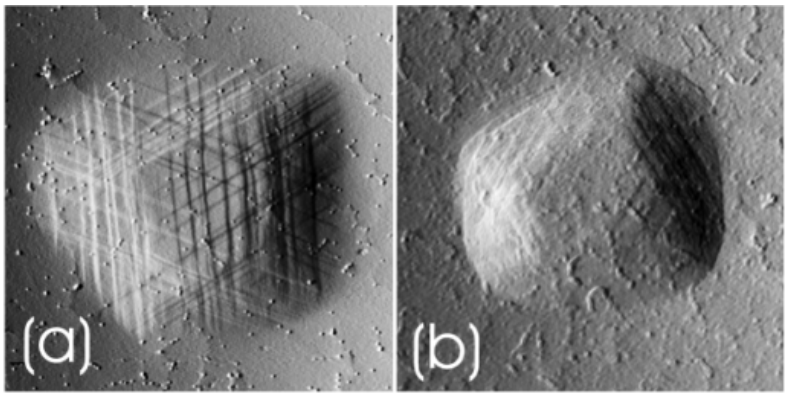

Figure 6.2: Typical amplitude-mode AFM images of (a) as-grown and (b) "ion-damaged" GaN films indented at a maximum load of 100 mN [horizontal field width = 4 μm for both images (a) and (b)].

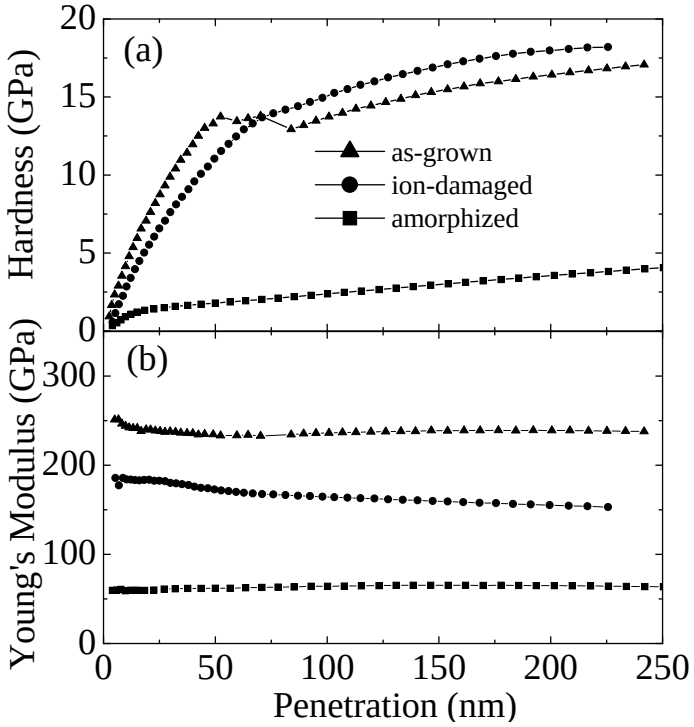

Figure 6.3: Curves of (a) the hardness and (b) Young's modulus as a function of indenter penetration below the circle of contact, as determined from partial load–unload data. Figures show data for as-grown, "ion-damaged," and amorphized GaN, as indicated in the legend in (a).

Table 6.2: Values of hardness, H, and Young's modulus, E, at a plastic penetration depth of 100 nm for the three GaN samples used in this study.

GaN sample	H (GPa)	E (GPa)
as-grown	13.4	233
"ion-damaged"	15.1	164
amorphized	2.4	65

as-grown GaN. Figure 6.3 also shows that the values of H and E of amorphized GaN are significantly lower than those of as-grown and "ion-damaged" GaN; i.e., *amorphous GaN is very soft.* Table 6.2 gives the values of H and E for the three GaN samples used in this study at a plastic penetration depth of 100 nm, a depth where the substrate effects are expected to be small.

Finally, Fig. 6.4 shows partial load–unload curves[2] of as-grown, "ion-damaged," and amorphized GaN films. This figure illustrates that, in "ion-damaged" GaN, the purely elastic regime extends to higher loads and penetration depths than in as-grown GaN. This result indicates that implantation disorder in crystalline GaN suppresses pressure-induced nucleation and/or propagation of extended defects, the processes which are most likely responsible for the plastic deformation of crystalline GaN [93, 94]. This can be explained based on a scenario when implantation defects (including planar defects, discussed in detail in Chapter 3) pin pressure-induced dislocations, thus inhibiting slip.

In contrast to the case of "ion-damaged" GaN, Fig. 6.4 shows that, in amorphized GaN, deformation response is elastic–plastic even for very low loads, and, with increasing load, plastic deformation dominates with pile-up around the impression (as revealed by AFM). Such a difference in the deformation modes of as-grown, "ion-damaged," and amorphized GaN is also reflected by the depths of residual depression (see Figs. 6.1 and 6.2) and the depths of maximum plastic penetration (see Fig. 6.3) of the above three samples.

6.4 Summary

In summary, wurtzite GaN films modified by ion bombardment have been studied by nanoindentation with a spherical indenter. Results show that implantation-produced defects suppress both "pop-in" events and slip during loading. This result suggests that slip nucleation (rather than a phase transformation) is responsible for "pop-in" events. In addition to suppressing slip, implantation disorder in crystalline GaN also suppresses the plastic component of deformation, which may suggest that slip is the major contributor to the plastic component of the deformation of crystalline GaN. The deformation behavior of amorphous GaN is very different from that of as-grown crystalline GaN. In particular, amorphous GaN exhibits plastic flow even for very low loads. In addition, the values of

[2]As discussed in Chapter 2, during partial load–unload indentation measurements, after each load increment, the indenter is partially unloaded (down to 50% of the maximum load at each step). For such a partial load–unload regime, if the deformation process is completely elastic, loading and unloading force–displacement curves overlap, as illustrated in Fig. 6.4 for as-grown and "ion-damaged" GaN for loads below $\sim$ 10 mN. When deformation becomes elastic–plastic (i.e., the material does not recover on unloading as it does in the purely elasic deformation regime), the partial load–unload curve splits into two branches, as illustrated in Fig. 6.4 for loads above $\sim$ 20 mN for all three samples shown.

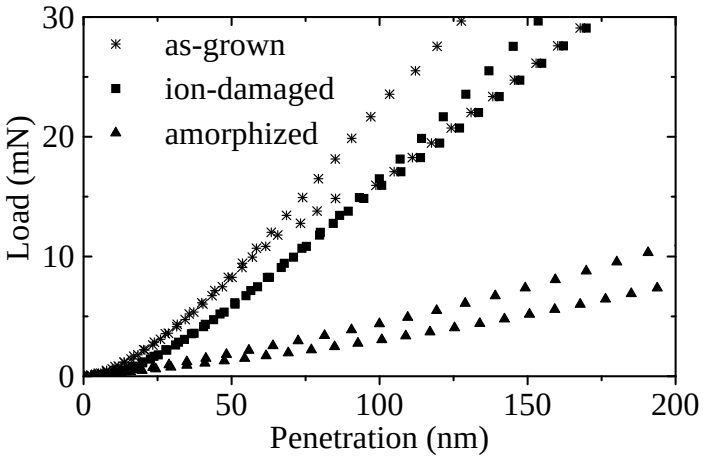

Figure 6.4: Partial load–unload curves of as-grown, "ion-damaged," and amorphized GaN films, as indicated in the legend.

hardness and elastic modulus of amorphous GaN are much lower than those of as-grown GaN, as indicated in Table 6.2. Finally, this study may have significant technological implications for the estimation of contact damage in ion-beam-processed GaN.

Chapter 7

Optical properties of ion-implanted GaN

7.1 Introduction

The luminescence properties of GaN have received extensive attention due to their importance in the fabrication of GaN-based optoelectronic devices. One of the GaN luminescent peaks, which has attracted considerable research interest, is the so-called yellow luminescence (YL) band. This ubiquitous broad luminescent peak centered on ~ 2.2 eV [at room temperature (RT)] has been observed in GaN grown by different techniques and in different laboratories (see, for example, reviews in Refs. [1–7]). In optoelectronic devices, YL is highly undesirable since it represents a competing recombination path which reduces the intensity of near-gap emission.

A large number of studies have been reported in the literature on the origin and properties of YL (see, for example, reviews in Refs. [1–7]). The YL band and related deep states have been studied both theoretically and experimentally by a range of techniques. Experimental data reported in the literature strongly suggests that the YL band can be attributed to a radiative transition between shallow donors (or the conduction band) and some deep traps (of either donor or acceptor nature). This mechanism for YL was originally proposed in an early work on this topic by Ogino and Aoki [97]. An alternative model for YL proposed by Glaser et al. [98], that YL is due to a radiative transition from a deep donor to a shallow acceptor, has not been supported by subsequent experiments reported in Refs. [99–101]. The broad nature of the YL band is typical for deep centers in semiconductors, given a strong electron-phonon interaction (see, for example, Ref. [102]).

In contrast to some apparent agreement on the most plausible scenario for the electronic levels involved in the radiative transition responsible for YL, the chemical origin of the YL band (and, hence, an unequivocal microscopic model for the center responsible for YL) remains a subject of strong debate. In particular, it is still not clear whether the center responsible for YL is of an intrinsic (i.e., due to native lattice defects alone) or of extrinsic (i.e., impurity-related) origin. Such a situation exists partly because most of the experimental techniques used to study YL in GaN are essentially "chemically blind" and allow much room for speculations about the chemical origin of the YL band.

Because YL is generally found in GaN grown by different techniques, it has been widely believed that intrinsic lattice defects (such as simple point defects or extended defects) participate in the formation of YL [1–7]. This conclusion was apparently supported by early ion implantation studies [103]. Indeed, Pankove and Hutchby [103] performed im-

plantation of thirty-five different species into GaN and found that most of the implants resulted in a strong increase in the intensity of YL, measured after postimplantation annealing. As a result, it has been suggested that point defects (which can be produced by ion bombardment) are responsible for YL [97, 103]. To our knowledge, this ion implantation report by Pankove and Hutchby [103] is the only "direct" experimental evidence in favor of intrinsic point defects as the origin of YL. In this chapter, we will discuss the results reported by Pankove and Hutchby [103] in view of our more recent ion implantation data and show that implantation-produced lattice defects alone do not give rise to YL.

Many authors have suggested that different impurities such as C [97, 104–110], O [109, 111–113], H [106, 114], or Si [109, 115, 116] participate in the formation of YL. For example, even one of the first detailed studies of YL in GaN by Ogino and Aoki [97] has shown that doping with C during crystal growth strongly emphasizes the YL band. However, based on this result and on ion implantation data reported by Pankove and Hutchby [103], Ogino and Aoki attributed the origin of YL to a complex consisting of a Ga vacancy and some impurity (not necessarily C) [97]. They have also proposed that the Ga vacancy determines the electronic level of the complex, and, hence, emission energy is independent of the impurity species, in agreement with the experimental data available at that time [97].

In this chapter, we discuss the chemical origin of YL, an understanding of which is very important for (i) the control of undesirable YL in GaN-based optoelectronic devices and (ii) the development of an adequate microscopic model for the center responsible for YL. To study the chemical origin of YL, we have performed an optical doping of GaN with potential impurities which are always unintentionally introduced into GaN during crystal growth (such as H, C, O, and Si) as well as with neutral species (such as N). Optical doping was done by ion implantation, a technique often used to introduce dopants in a well controlled manner. However, ion implantation inevitably produces lattice disorder which is well known to have a detrimental effect on the luminescence of GaN in the visible part of the spectrum. Indeed, a number of previous studies have shown that implantation-produced lattice defects act as non-radiative recombination centers in GaN, resulting in a severe quenching of most characteristic luminescence peaks exhibited by as-grown GaN (see, for example, Refs. [39,40,103,117,118]). Hence, in Sect. 7.3, we first address the effects of ion-beam-produced lattice defects on the optical properties of GaN. An understanding

Table 7.1: Free electron concentration (n) and effective Hall mobility (μ_{eff}) of the three GaN wafers used in sequential implantation experiments. IMRE stands for Institute of Materials Research and Engineering in Singapore.

Wafer	Grower	n (10^{16} cm^{-3})	μ_{eff} (cm^2 V^{-1} s^{-1})
A	IMRE	4	144
B	EMCORE	≤ 1	–
C	Ledex	0.5	90

of such effects is not only important to ascertain the role of intrinsic lattice defects in the formation of YL but is also vital for a correct interpretation of luminescence spectra from GaN optically doped by ion implantation.

7.2 Experimental

The samples used in this study were cut from six wafers of $\sim$ 2-μm-thick wurtzite GaN epilayers grown on c-plane sapphire substrates by MOCVD in three different EMCORE reactors. Both nominally undoped and Si-doped GaN wafers were used. The samples were implanted at RT with keV ^{1}H, ^{11}B, ^{12}C, ^{14}N, ^{16}O, or ^{28}Si ions. During implantation, samples were tilted by $\sim 7^{\circ}$ relative to the incident ion beam to minimize channeling.

As will be shown below, from the species listed above, H, C, and O have been found to be involved in YL. Therefore, using successive masking before each implantation step, we performed identical sequential implantation of H, C, and O into GaN samples cut from three representative wafers (A, B, and C) grown in different laboratories. The electrical characteristics of these wafers are given in Table 7.1, as assessed by Hall effect measurements or specified by the grower. Sequential ion implantation was performed so that, at the end of the implant sequence, each sample had the following areas: (i) virgin (as-grown) material, masked during all implantation steps; (ii) implanted with C; (iii) implanted with O; (iv) implanted with H; (v) implanted with C and O; (vi) implanted with C and H; (vii) implanted with O and H; and (viii) implanted with all three species (C, O, and H). The details of implant conditions used to prepare these samples are given in Table 7.2. The energies of C, O, and H ions shown in this table have been chosen so that the depth

Table 7.2: Implant conditions used to introduce C, O, and H species into GaN by sequential ion implantation at RT. Calculated values of projected ion ranges (R_p) and the average number of lattice vacancies produced by one ion (N_{vac}) are also given.

Implant order	Ion	Energy (keV)	Dose (10^{14} cm^{-2})	Beam flux (10^{11} cm^{-2} s^{-1})	R_p (Å)	N_{vac}
1	^{12}C	120	1	5.5	1945	946
2	^{16}O	150	1	5.5	1890	1429
3	^{1}H	25	1	5.5	1995	17

profiles of implanted species closely overlap, as can be seen from projected ion ranges, calculated using the TRIM code [22], as given in Table 7.2.

In addition, to study the influence of lattice defects on luminescence from GaN, we carried out implantation with 150 keV $^{12}C^{-}$ ions at RT or liquid nitrogen temperature (LN_2) over a wide dose range. During implantation, each sample was partly masked by a piece of Si in order to retain an unimplanted region.

Postimplantation annealing was carried out at 1050 °C in a rapid thermal annealing (RTA) system in a nitrogen ambient at atmospheric pressure. The annealing was performed in the proximity geometry (where GaN samples are placed face-to-face in order to minimize material decomposition). It should be noted that thermal annealing at 1050 °C had a negligible effect on the CL intensities from as-grown GaN samples used in this study. CL measurements were carried out at LN_2 and RT. During data acquisition, a finely focused electron beam was scanned over a frame of $\sim 80 \times 100$ μm^2 at a rate of 10 frames/s. CL kinetics profiling was done in spot mode with a finely focused electron beam. Excitation measurements were performed by changing electron beam current, while maintaining a finely focused electron beam. Depth-resolved CL measurements were conducted under the constant beam power condition; i.e, beam energy × beam current = constant [119].

7.3 Influence of defects on luminescence and absorption

Figure 7.1(a) shows CL spectra obtained at RT from virgin and implanted regions of GaN bombarded with 150 keV C ions at LN_2 to a dose of 10^{14} cm^{-2}. The spectra illustrate the

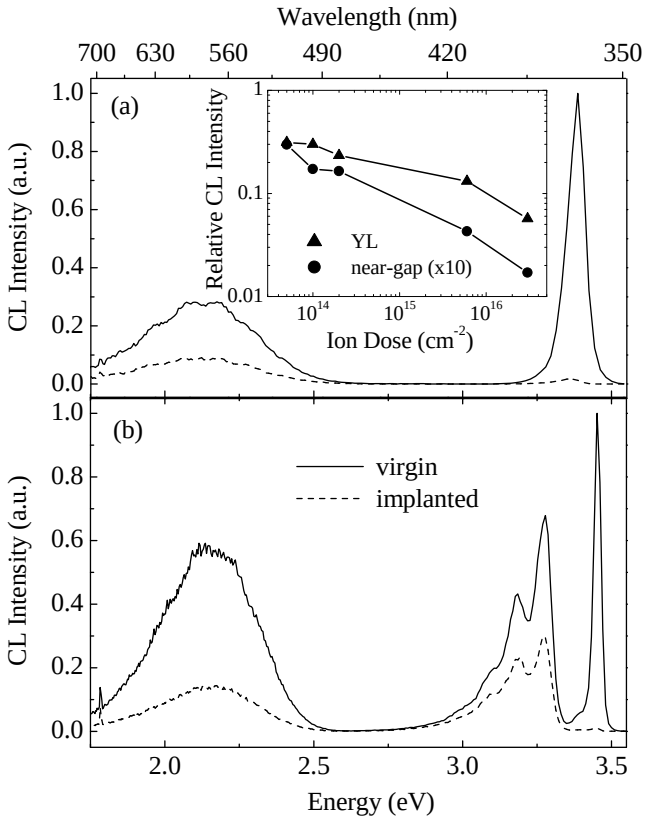

Figure 7.1: CL spectra obtained at RT (a) and LN_2 (b) from virgin and implanted regions of GaN bombarded with 150 keV C ions at LN_2 with a beam flux of 3.4×10^{13}cm^{-2} s^{-1} to a dose of 10^{14} cm^{-2} [wafer A, electron beam energy = 20 keV, CL bandpass = 2.5 nm for (a) and = 1.25 nm for (b)]. The inset in (a) illustrates the ion dose dependence of the intensities of near-gap and yellow luminescence peaks measured at RT from implanted parts of the samples relative to the corresponding CL intensities in the virgin parts of these samples.

well-known effect of implantation-produced quenching of the intensities of both near-gap emission (centered on ~ 3.39 eV) and the YL band (a broad peak centered on ~ 2.12 eV) present in this GaN wafer [39,40,103,117,118]. The ripples usually visible in the YL band can be attributed to the microcavity effect [120]. In addition, the inset in Fig. 7.1(a) shows the ion dose dependence of the intensities of near-gap and YL peaks at RT in implanted parts of samples relative to the corresponding CL intensities in the virgin parts of these samples. It is seen that, with increasing dose of 150 keV C ions, the intensities of both near-gap and YL peaks are drastically reduced.

Figure 7.1(b) shows CL spectra obtained at LN_2 from virgin and implanted regions of a

GaN sample implanted under the same conditions as the sample shown in Fig. 7.1(a). The LN_2 spectra in Fig. 7.1(b) consist of near-gap emission at 3.45 eV; donor–acceptor pair (DAP) emission at 3.28 eV with two LO phonon replicas at 3.18 and 3.08 eV, respectively [2, 3]; a broad YL band centered on 2.16 eV; and sharp Cr^0_{Al} : Al_2O_3 emission from the substrate at 1.78 eV.

It is seen from Fig. 7.1(b) that ion implantation considerably reduces the intensities of all CL peaks present at LN_2 in the visible part of the spectrum. However, the intensity of near-gap emission is quenched more efficiently than that of the other CL peaks shown in Fig. 7.1(b). A similar effect can be seen from Fig. 7.1(a) for the case of RT CL data. Indeed, Fig. 7.1(a) as well as the inset in this figure shows that ion implantation preferentially reduces the measured intensity of near-gap emission. The depth-resolved CL measurements presented below will provide an explanation for this effect.

Figure 7.2 shows near-gap and YL depth profiles obtained at RT from as-grown GaN. In such depth profiles, CL intensity is plotted as a function of electron beam energy or the corresponding electron penetration range, R_{KO}, which can be approximated using the Kanaya-Okayama equation [121]. For a homogeneous GaN sample, under the conditions of constant beam power employed in this work, the CL generation rate is essentially constant at different beam energies. However, Fig. 7.2 shows that, in as-grown GaN, the *measured* intensity of near-gap emission decreases with increasing electron beam energy due to efficient self-absorption (i.e., internal CL absorption caused by an exponential absorption tail at the GaN band-edge), and the YL intensity slightly increases with beam energy due to a corresponding increase in the concentration of YL centers toward the GaN/sapphire interface (see, for example, Ref. [119]) and/or due to the saturation of YL emission [122].[1]

Figure 7.3(a) shows near-gap and YL depth profiles obtained at RT from a GaN sample bombarded with 150 keV C ions at LN_2 to a dose of 5×10^{13} cm^{-2}. It is seen from Fig. 7.3(a) that, in the ion-damaged layer (up to $\sim$ 700 nm from the surface), the intensities of both

[1]Also note that a further decrease in the intensity of near-gap emission for electron beam energies above $\sim$ 20 keV is expected since the electron penetration range becomes larger than film thickness (which is $\sim$ 2 μm). The fact that the intensity of YL does not decrease for electron beam energies above $\sim$ 20 keV (see Fig. 7.2) can be attributed to strong saturation effects of YL discussed in detail in Ref. [122].

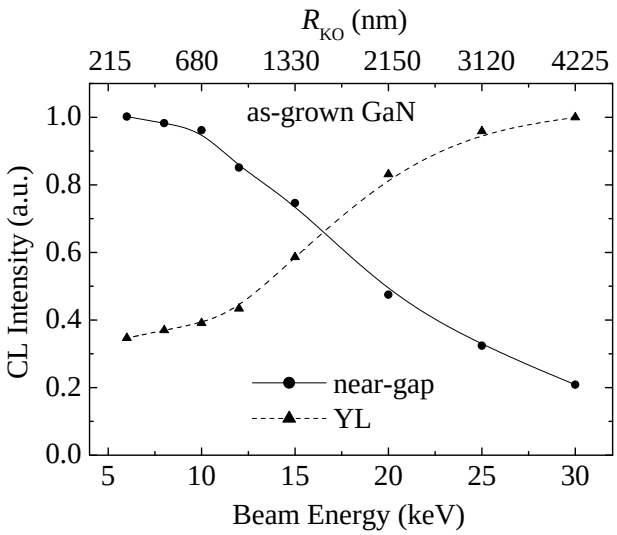

Figure 7.2: Near-gap and YL depth profiles obtained at RT from as-grown GaN (wafer A, CL bandpass = 25 nm, electron beam power = 7 μW).

near-gap and YL peaks are drastically reduced below the detectable level.[2] Therefore, CL emission from the implanted sample shown in Fig. 7.1, obtained with an electron beam energy of 20 keV, is actually generated by the electron beam impinging on virgin GaN, beyond the implanted layer, which is schematically illustrated in Fig. 7.4. This observation can also be used to explain the preferential quenching of near-gap emission compared with the other emission peaks in Fig. 7.1. Indeed, it has previously been shown [119, 123] that self-absorption can change detected CL near-gap emission of as-grown GaN. Our results indicate that implantation-induced absorption of CL in the implanted layer can strongly affect detected near-gap emission from underlying virgin GaN.

Another interesting result from Fig. 7.3(a) is that, in as-implanted GaN, CL is quenched up to a depth of $\sim$ 700 nm, which is well beyond the layer modified by ion bombardment, as given by TRIM [22], which takes into account only collisional processes. Such a quenching of CL emission beyond the ion penetration range can be attributed to the diffusion of implantation-produced point defects. This conclusion is supported by the fact that ion-generated point defects are highly mobile in GaN at LN_2 and above, as discussed in

[2]Note that the sample shown in Fig. 7.1 was bombarded to twice the dose (10^{14} cm^{-2}) of the sample shown in Fig. 7.3 (5×10^{13} cm^{-2}). Therefore, the effect of the quenching of CL emission coming from the implanted layer is even more pronounced in Fig. 7.1.

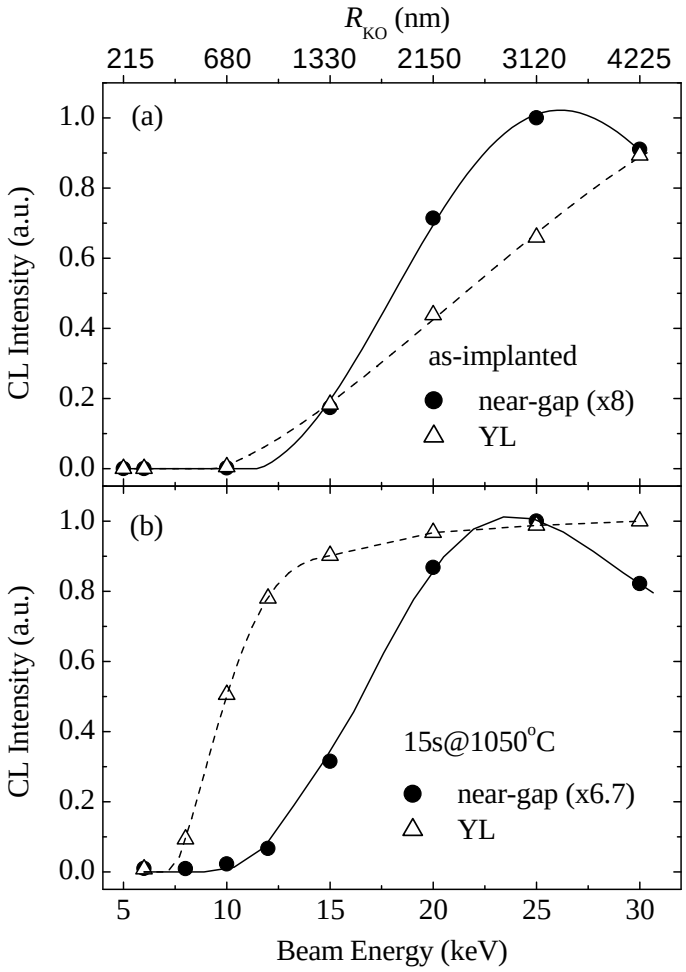

Figure 7.3: Near-gap and YL depth profiles obtained at RT from a GaN sample bombarded with 150 keV C ions at LN_2 with a beam flux of 3.4×10^{13} cm^{-2} s^{-1} to a dose of 5×10^{13} cm^{-2} (wafer A, CL bandpass = 25 nm, electron beam power = 7 μW). Shown are the depth profiles of the implanted GaN sample before (a) and after (b) postimplantation annealing at 1050°C for 15 s.

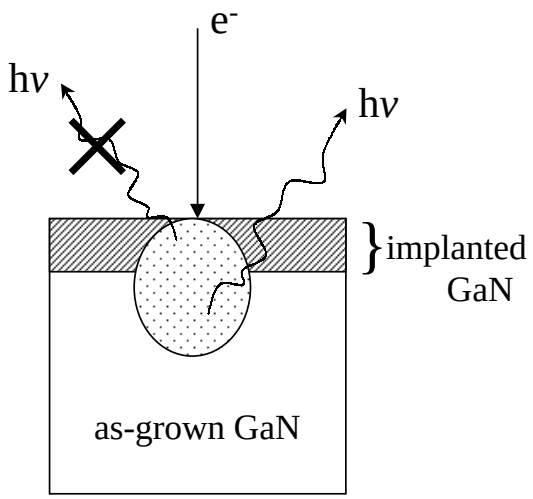

Figure 7.4: Schematic diagram illustrating that CL emission measured from GaN implanted with keV ions is actually generated by the electron beam impinging on virgin GaN, beyond the implanted layer, while CL emission from the implanted layer is dramatically reduced.

detail in Chapter 3.

It should also be noted that the conclusion that CL of GaN is dramatically quenched by relatively low dose ion bombardment is consistent with the results of our luminescence studies of GaN irradiated with MeV light ions, which penetrate throughout the entire GaN film. Indeed, our analysis of CL spectra from GaN implanted with 150 keV C or 1.8 MeV He ions at RT shows that disorder produced by light-ion bombardment to a critical dose corresponding to the generation of $\sim 5 \times 10^{19}$ vacancies/cm^3 (as estimated using TRIM [22]) is sufficient to reduce the intensity of near-gap emission by more than two orders of magnitude. However, the exact value of this critical dose depends on a number of implant parameters, such as ion mass, energy, beam flux, and substrate temperature.

Typical CL spectra of GaN (wafer C) implanted with H, C, and O ions (without postimplantation annealing), illustrating the effects of implantation-produced lattice defects on the luminescence of GaN, are shown in Fig. 7.5. These spectra, obtained at RT, consist of near-gap emission (centered on ~ 3.39 eV), blue luminescence (a broad CL peak centered on ~ 2.82 eV), and the YL band (centered on ~ 2.15 eV). As seen from Fig. 7.5, implantation with different ion species considerably reduces the intensities of all CL peaks observed, which is consistent with results of 150 keV C ion implantation discussed above

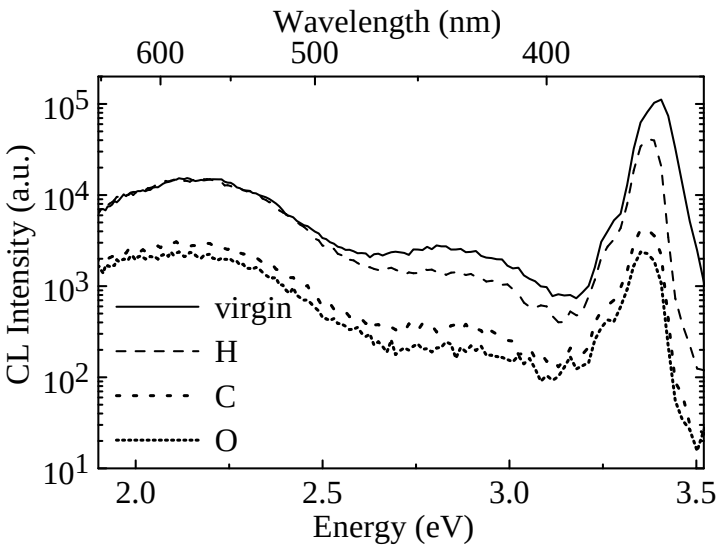

Figure 7.5: CL spectra obtained at RT from as-grown GaN and GaN implanted with H, C, and O ions, as indicated in the legend (wafer C, electron beam energy = 20 keV, electron beam current = 8.6 nA, CL bandpass = 2.5 nm). The details of implant conditions are given in Table 7.2.

(see Fig. 7.1). It is important to note that both Figs. 7.1 and 7.5 show that implantation-produced defects do not give rise to any new luminescent bands in the visible part of the spectrum, which is consistent with luminescence studies of ion-implanted GaN reported previously (see, for example, Refs. [39, 40, 103, 107, 117, 118]). Hence, it can be concluded that intrinsic lattice defects, produced by ion bombardment (i.e., point defect complexes and some planar defects, as discussed in Chapter 3), mainly act as efficient nonradiative recombination centers, resulting in a strong decrease in CL intensity. This conclusion is also supported by annealing studies discussed in Sect. 7.4.

Figure 7.5 also shows that the extent of CL quenching by ion bombardment is roughly proportional to the amount of lattice damage produced. This conclusion follows from a comparison of CL intensities shown in Fig. 7.5 with the number of ion-beam-generated lattice vacancies given in Table 7.2. However, CL depth-profiles illustrated in Fig. 7.3(a) show that, for implant and CL conditions of this study, CL generation within the implanted layer is dramatically quenched. In this case, the detected CL signal is generated by the electron beam impinging on virgin GaN, beyond the implanted layer (see Fig. 7.4). Hence, a further quenching of CL emission with an increase in implantation-produced lattice disorder (see CL spectra in Fig. 7.5 for the cases of implantation with H, C, and O ions)

can be attributed to an increase in the extent of defect-related light absorption within the implanted layer.

7.4 Thermal annealing of implantation damage

As shown above, implantation-produced lattice defects act as very efficient nonradiative recombination centers. Therefore, in order to study the effects of implanted species on YL, such ion-beam-produced defects must be removed. As has been reported by several groups (see, for example, Refs. [39, 40, 103, 117, 118]), the annealing of GaN implanted with keV ions usually recovers (although always only partly) the measured intensities of light emission. Such a partial elimination of ion-beam-induced luminescence quenching by postimplantation annealing has been attributed to a corresponding partial recovery of non-radiative defects produced by ion bombardment [39,40,103,117,118]. Below, we show that implantation-produced damage and postimplantation annealing affect not only light emission from the implanted layer but also the detection of CL emission from virgin GaN due to the absorption of light within the implanted layer. Awareness of this behavior is required for a correct interpretation of luminescence measurements of GaN optically doped by implantation with keV ions. Having understood the influence of irradiation-produced defects on light emission and absorption discussed in this section, we use ion implantation to study the chemical origin of the notorious YL in GaN in Sect. 7.5.

Shown in Fig. 7.3(b) are CL depth profiles taken from the same sample as shown in Fig. 7.3(a) after annealing at 1050 °C for 15 s. It is seen that such annealing does not recover either near-gap or YL emission generated in the near-surface region (up to $\sim$ 450 nm from the surface). This depth is consistent with TRIM calculations [22], which indicate that the layer directly modified by bombardment with 150 keV C ions (say, $R_p + 3\Delta R_p$, where R_p is the projected ion range, and ΔR_p is the ion straggling) is also $\sim$ 450 nm thick. Therefore, an apparent recovery of emission by such annealing[3] can be attributed to the thermal recovery of damage, leading to a reduction in the absorption of light within the implanted layer. This conclusion is consistent with changes in the color

[3]After such annealing of the sample from Fig. 7.3, the relative intensity of near-gap emission (measured with an electron beam energy of 20 keV) in the implanted part to that in the virgin part of the sample recovered from $\sim$ 4% in the as-implanted sample to $\sim$ 14% in the annealed one.

of implanted samples observed to result from annealing. Indeed, GaN bombarded under implant conditions of this study has a yellowish-brown appearance. The 1050 °C annealing treatment significantly decreases the efficiency with which visible light is absorbed in the implanted layer, making implanted GaN appear as transparent as virgin GaN. Our results also show that the (partial) recovery of CL emission in the implanted layer by annealing at temperatures up to 1050 °C occurs only for rather low dose implantation with 150 keV C ions (such as $\sim 10^{12}$ cm^{-2}).

The above results show that RTA annealing at temperatures up to 1050 °C is not sufficient to completely remove lattice defects produced even by the relatively low dose light-ion bombardment used in this study (see Table 7.2 for implant conditions). An apparent recovery of detected luminescence by such annealing can be attributed to (i) thermally-induced recovery of lattice defects that enhance the absorption of light within the implanted layer and (ii) recovery of CL emission in the ion end-of-range region, where the concentration of implantation-produced defects is sufficiently low so that most of these defects can be effectively removed by such annealing. Indeed, Fig. 7.3 shows that CL emission is restored in the ion end-of-range region, where the level of implantation disorder is relatively low, but the concentration of implanted species is relatively high. This interesting result can be explained as follows. In the first approximation, the depth distributions of implanted species and atomic displacements, generated by the ion beam, can be described by the first moments (R_p and R_{p_d} for the distributions of ion ranges and atomic displacements, respectively) and by the second central moments (ΔR_p and ΔR_{p_d} for ion ranges and atomic displacements, respectively) [124]. Because $R_p > R_{p_d}$ (always) and $\Delta R_p > \Delta R_{p_d}$ (in the case of light ions as used in this study) [124], the depth distribution of implanted species is shifted deeper into the crystal bulk with respect to the distribution of atomic displacements. Hence, there is a layer in the ion end-of-range region where the *concentration* of implanted species is relatively high, while the amount of implantation damage, produced both by ballistic collisional processes and due to defect migration, is sufficiently low to be successfully recovered by the annealing treatment used in this study. Hence, a RTA treatment with annealing temperatures up to 1050 °C can be applied to study the optical effects of implanted species, although CL emission within most of the implanted layer can be dramatically quenched even after such annealing.

7.5 Role of implanted species in yellow luminescence

First of all, it should be noted that, from all species implanted (H, B, C, N, O, and Si), only H, C, and O have been found to be involved in YL. Indeed, introduction of B, N, and Si (to ion doses up to $\sim 10^{14}$ cm^{-2}) into all GaN samples studied did not result in an enhancement of the intensity of YL. Therefore, we will concentrate below on the role of H, C, and O in the formation of the YL band.

Shown in Fig. 7.6 are CL spectra obtained at RT from GaN implanted with H, C, or O ions and subsequently annealed at 1050 °C for 15 s. It is seen that H, C, and O implantation results in an increase in the intensity of YL.[4] Table 7.3 gives the intensities of near-gap and YL peaks (normalized to the corresponding values of the intensities in the unimplanted parts of these samples) taken from representative samples A, B, and C implanted with H, C, and O ions. CL measurements performed at LN_2 reveal qualitatively similar results to those shown in Fig. 7.6 and Table 7.3 for CL data obtained at RT. Below, we discuss the role of each of these species separately.

It should be noted that previous studies on redistribution of dopants implanted into GaN have shown that C, O, and Si exhibit negligible diffusion during RTA used in this study (i.e., 15 s at 1050 °C) [1]. Although H generally shows some diffusion in *n*-type GaN at temperatures above $\sim$ 800 °C, previous results [1] as well as our secondary ion mass spectrometry (SIMS) studies indicate that a significant fraction of H still remains within the GaN film after annealing at 1050 °C for 15 s, presumably, due to the affinity of H to decorate as-grown and implantation-produced lattice defects. However, longer anneals (such as $\geq$ 2 min at 1050 °C) of H-implanted samples have revealed a reduction in YL intensity, suggesting an effective out-diffusion of H atoms from the GaN film, which is consistent with previous reports on the redistribution of H in GaN [1].

[4]Figure 7.6 also shows a small red-shift of the *near-gap* emission peak (at $\sim$ 3.4 eV) in the spectra obtained from C- and O-implanted samples as compared to spectra obtained from as-grown and H-implanted GaN. This red-shift can be attributed to defect-induced absorption of CL emission within the implanted layer, as discussed in Sect. 7.3. The absence of such a red-shift in the case of GaN implanted with H ions and subsequently annealed suggests that postimplantation annealing effectively recovers (though only partially) CL emission within the layer damaged by H ion bombardment.

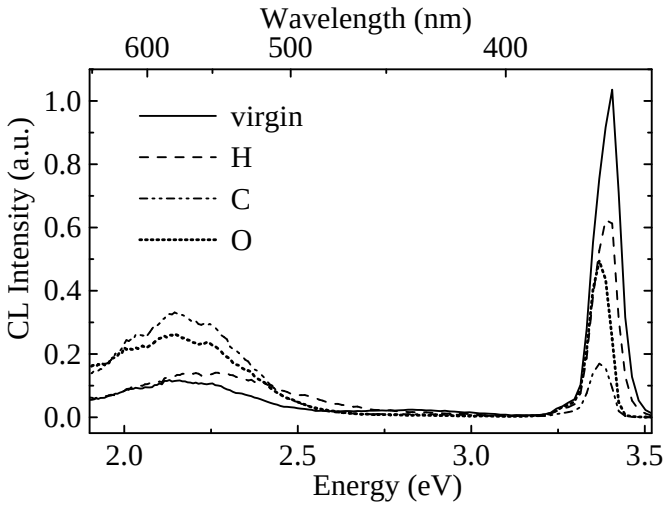

Figure 7.6: CL spectra obtained at RT from GaN implanted with H, C, and O ions, as indicated in the legend, and subsequently annealed at 1050 °C for 15 s (wafer C, electron beam energy = 20 keV, electron beam current = 8.6 nA, CL bandpass = 2.5 nm). The details of implant conditions are given in Table 7.2.

Table 7.3: Intensities of near-gap (NG) and YL peaks obtained from samples cut from GaN wafers A, B, and C (see Table 7.1) implanted with H, C, and O ions. The details of implant conditions are given in Table 7.2. CL intensities were normalized to the intensities of corresponding NG and YL peaks in the unimplanted parts of the samples (electron beam energy = 20 keV, CL bandpass = 2.5 nm).

Species	Wafer A		Wafer B		Wafer C	
	NG	YL	NG	YL	NG	YL
virgin	1.0	1.0	1.0	1.0	1.0	1.0
H	0.679	1.011	0.779	2.618	0.613	1.391
C	0.206	1.698	0.217	1.971	0.169	2.793
O	0.207	0.477	0.372	3.088	0.477	2.203
C+H	0.190	2.295	0.342	3.118	0.169	3.447
O+H	0.201	0.510	0.407	3.382	0.477	4.284
C+O	0.144	1.348	0.224	3.324	0.303	10.523
C+O+H	0.141	1.424	0.342	3.765	0.303	13.860

7.5.1 Oxygen

Figure 7.6 and Table 7.3 show that implantation of O into *some* GaN samples (such as those cut from wafers B and C) enhances the intensity of the YL band. However, in other samples (as represented by wafer A in Table 7.3), the introduction of O does not result in an increase in the intensity of YL. This result is consistent with some previous implantation studies [107,117], which suggests that O may participate in the formation of the YL band. Although the exact role of O in YL is not clear at present, it appears that O acts as a shallow donor involved in YL. Such a conclusion is supported by the fact that the introduction of O by ion implantation enhances YL only in the samples with relatively low initial concentrations of free carriers ($\leq 1 \times 10^{16}$ cm^{-3}), as may be seen from Tables 7.1 and 7.3. Moreover, our additional results show that implantation of O (with an energy of 150 keV and to doses up to $\sim 1 \times 10^{14}$ cm^{-2}) into several Si doped GaN samples with initial free electron concentrations from $\sim 5 \times 10^{16}$ to 5×10^{18} cm^{-3} does not result in an increase in the intensity of YL (as measured either before or after postimplantation annealing). Hence, taking into account the currently most plausible model for the energy transitions involved in YL [97], we attribute the increase in YL intensity caused by O implantation into samples with a low initial free electron concentration (see Tables 7.1 and 7.3) to a formation of DAP's involving O atoms, which are known to act as relatively shallow donors in GaN [1,125], and deep acceptors unintentionally introduced into GaN during crystal growth.

It should also be noted that the involvement of Si in the YL band previously reported in Refs. [115] and [116] might be somewhat similar to that of O discussed here; i.e., Si acts as a shallow donor. However, the effect of self-compensation (see, for example, Ref. [115]), which may result in the formation of deep acceptor traps (involving, presumably, intrinsic defects as well as H and/or C, as discussed below) participating in YL, seems to be a more plausible explanation for the effects of Si doping reported in Refs. [115] and [116]. Indeed, ion implantation results presented here as well as reported elsewhere [107,117] show that introduction of Si itself does not enhance the intensity of YL.

In summary, implantation of O enhances YL only in samples with a relatively low initial concentration of free carriers. This may suggest that shallow donor levels of O are involved in DAP's possibly responsible for YL. However, at present, more work is needed in order to better understand the role of O in the formation of YL.

7.5.2 Carbon

Figure 7.6 and Table 7.3 clearly indicate that C is involved in the complex responsible for the YL band in GaN. Indeed, in this study, implantation of C into six different GaN wafers (with initial free electron concentrations up to 5×10^{18} cm^{-3}, grown by MOCVD in three different laboratories) always resulted in a strong enhancement of the intensity of the YL band, as measured after postimplantation annealing. In addition, our studies show that an enhancement of YL is observed only for implantation to moderate doses of C ions ($\geq 10^{13}$ cm^{-2} of 120 keV C ions, corresponding to the introduction of $\geq 10^{18}$ cm^{-3} of C atoms), while lower dose C ion implantation (say, $\sim 10^{12}$ cm^{-2} of 120 keV C ions) does not result in an enhancement of YL. This latter result is consistent with the fact that the concentration of background C impurities, unintentionally introduced during MOCVD growth, is usually of the same order of magnitude; i.e., $\geq 10^{17} - 10^{18}$ cm^{-3} [1].

Another interesting effect, which can be observed from Figs. 7.5 and 7.6 as well as from Table 7.3, is that, in addition to giving rise to YL, C-related complexes appear to act as efficient nonradiative recombination centers. Indeed, as can be seen from Table 7.2, bombardment of GaN with 120 keV C ions produces ~ 1.6 times fewer atomic displacements than irradiation with 150 keV O ions. This difference in the damage levels produced by different ions is directly reflected by the extent of the quenching of CL emission in as-implanted samples (without postimplantation annealing), as shown in Fig. 7.5. However, Fig. 7.6 and Table 7.3 illustrate that, after postimplantation annealing, the intensity of near-gap emission in C-implanted samples is significantly lower than that in O-implanted samples, despite a large difference in the concentration of ion-beam-generated atomic displacements for C and O ion bombardment. This effect may be attributed to participation of C in complexes which act as efficient nonradiative recombination centers (or centers with low radiative recombination probability) and result in a decrease in the intensity of near-gap emission.

Other possible scenarios for the effect of preferential quenching of all CL peaks by implantation with C ions are (i) the trapping of defects at C-related complexes during thermal annealing, which may result in the suppression of the efficiency of defect removal during annealing and (ii) involvement of C in defect-impurity complexes which act as strong light absorbers and, hence, affect detected CL intensities. However, the former scenario does not seem to be plausible since the concentration of C atoms introduced

is rather low ($\leq 6 \times 10^{18}$ cm^{-3}) to significantly affect the thermally-induced removal of implantation-produced defects. The latter scenario also seems unlikely since a RTA treatment at 1050 °C results in a complete restoration of the original sample color in the cases of all three implants (H, C, and O), which suggests an efficient recovery of light absorbing defects. Indeed, as discussed above, as-implanted samples grown on sapphire substrates have a yellowish-brown appearance, while annealing at 1050 °C completely recovers the apparent transparency of implanted samples to that of as-grown GaN.

In summary, our data shows that implantation of C strongly enhances the intensity of YL in GaN. In addition to giving rise to YL, C-related complexes appear to act as efficient nonradiative recombination centers.

7.5.3 Hydrogen

Figure 7.6 shows a typical spectrum of a H-implanted and subsequently annealed GaN sample, which clearly shows that implantation of H produces a broad luminescent band (centered on $\sim$ 2.25 eV) which is slightly ($\sim$ 0.1 eV for wafer C) blue-shifted relative to the C-related YL peak. This result suggests that H also participates in the formation of the YL band in GaN.

The role of H in the formation of YL in GaN is better illustrated by our (electron) *excitation density* measurements (i.e., the dependence of CL intensity on electron beam current). Indeed, such measurements taken from C and O ion-implanted and subsequently annealed GaN have not revealed any detectable shift in the position of the YL band for the range of excitation densities used (for electron beam currents from 0.5 up to 15 nA with an electron beam energy of 20 keV). However, the results of similar excitation studies of H-implanted and subsequently annealed samples have shown that, with a 30-fold increase in excitation density, *the H-related YL band* undergoes a detectable blue-shift (for example, a blue-shift of $\sim$ 7 meV in the case of wafer B).[5] Such a blue-shift suggests that DAP recombination may be involved in the formation of the H-related YL band. This conclusion follows from (i) the inverse dependence of peak energy on DAP separation and

[5]It should be noted that our detailed kinetics profiling studies show that kinetics effects (i.e., the effects of electron-beam-induced modification of GaN during CL measurements) are very weak and can be neglected in the interpretation of CL data from the ion-implanted and subsequently annealed GaN samples used in this study.

(ii) a reduction in the transition probability with increasing pair separation. As a result, at higher excitation densities, widely separated pairs are saturated, and the contribution from radiative recombination at closely separated pairs increases, leading to a blue-shift in the position of the peak maximum (see, for example, Ref. [29]).

However, in addition to the DAP mechanism, a blue-shift with increasing excitation density may also be due to other processes such as (i) band filling, (ii) a reduction in band-bending if YL is due to radiative transitions involving surface states, and/or (iii) saturation of a lower energy peak if YL is comprised of several broad overlapping peaks. These possible processes have previously been reported to explain photoluminescence data (see, for example, Refs. [2, 3, 29, 126]). However, it is rather unlikely that band filling is responsible for such a blue-shift since the position of other peaks, including near-gap emission, does not change with increasing excitation density. The involvement of surface states in the radiation transition responsible for YL in ion-implanted samples also seems to be unlikely. Indeed, our CL depth profiling studies have shown that, even after postimplantation annealing used in this study, YL is suppressed in the very near-surface layer, as was discussed in Sect. 7.4. Hence, the most plausible explanations for the blue-shift observed in H-implanted samples are DAP transitions and the saturation of a smaller energy peak if the YL band is comprised of several broad overlapping peaks. Additional studies are required to distinguish between these two scenarios.

Finally, in addition to the dependence of the *position* of the YL band on excitation density, the behavior of CL *intensity* as a function of excitation density can help to better understand the role of H, C, and O in the formation of YL. Figure 7.7 shows the intensities of near-gap and YL in H-, C-, and O-implanted and subsequently annealed samples as a function of electron beam current. It is seen from Fig. 7.7 that, in contrast to C- and O-implanted samples, the intensity of the YL band in the H-implanted sample exhibits a more complex behavior with changing excitation density. Such dependencies of the intensity and position of the YL band on excitation density (see the above discussion and Fig. 7.7) suggest that the YL band in H-implanted GaN consists of at least two contributions: (i) H-related YL and (ii) C-related YL, as discussed more fully below. Hence, several radiative recombination channels (at least two: H- and C-related) can contribute to the YL band, which is consistent with a number of previous studies [106, 114, 127, 128].

In summary, implantation of H produces a broad luminescence band which is strongly

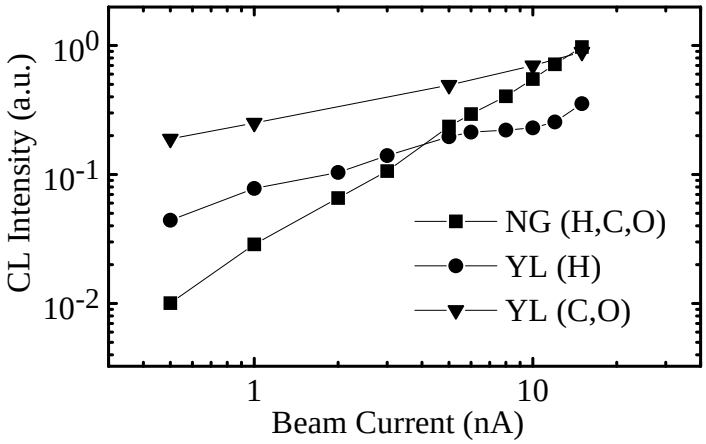

Figure 7.7: Intensities of near-gap (3.39 eV) and YL (2.15 eV) peaks measured at RT from GaN samples implanted with H, C, and O ions (as indicated in the legend), and subsequently annealed at 1050 °C for 15 s, as a function of electron beam current obtained with a finely focused electron beam (wafer B, electron beam energy = 20 keV, CL bandpass = 2.5 nm, scan size $\approx 80 \times 100$ μm^2). The details of implant conditions are given in Table 7.2.

blue shifted relative to the C-related YL peak. In contrast to the behavior of the YL band in C- and O-implanted GaN, the H-related YL band undergoes a blue shift with increasing CL excitation density.

7.6 Discussion of the chemical origin of yellow luminescence

In this section, we discuss the chemical origin of YL based on our data as well as on the results previously reported in the literature. First of all, all experimental data available shows that the chemical origin of YL is not simple, which may explain the apparent contradiction and complexity of the results on the properties of YL reported in the literature [2,3]. In agreement with previous reports [106,114,127,128], our data shows that YL consists of several (at least two: H- and C-related) luminescence bands overlapping in the same spectral region. Hence, several radiative recombination channels contribute to the YL band.

We emphasize that our data shows that lattice defects alone do not give rise to YL. Indeed, bombardment of GaN with species such as B, N, or Si produces lattice defects

but does not emphasize YL. Postimplantation annealing of these samples also does not result in an increase in the intensity of YL as compared to the corresponding intensity of YL in as-grown GaN samples. An apparent contradiction between our results and the results of previous luminescence studies of ion-implanted GaN reported by Pankove and Hutchby [103], where most of implants have been shown to result in a strong increase in the intensity of YL, may be reconciled as follows. Assuming that a C-defect complex is involved in the formation of YL, one can speculate that ion-beam-produced lattice defects forming complexes with C atoms, unintentionally introduced into GaN during crystal growth, were responsible for the ion-beam-induced increase in the intensity of YL reported in Ref. [103]. Such a scenario is strongly supported by the fact that most of the GaN crystals grown in the 1970's had a very large background concentration of impurities such as C and O.

As discussed above, the intrinsic origin of YL (i.e., lattice defects alone) is not supported by our experimental data, which indicates that specific impurities are involved in the center responsible for YL. From the possible candidates, strong *experimental evidence* exists in favor of C. Indeed, experimental studies show that the introduction of C either during crystal growth [97,104,106,108] or by ion implantation [103,107,117] into MOCVD grown GaN *always* strongly enhances the intensity of the YL band. Introduction of other species does not consistently have such an effect on the intensity of YL. An important role of C in the formation of YL in GaN has also been supported by photoionization spectroscopy experiments recently reported by Klein et al. [110].

Despite such strong and unambiguous experimental evidence, the important role of C in the formation of YL is generally not recognized at present. Indeed, in a recent report, Neugebauer and Van de Walle [129] have *theoretically* investigated a number of possible configurations of C in GaN (including several C-defect complexes). They have found that, within the theoretical treatment used, C does not give rise to any deep acceptor level in GaN with a low formation energy. Hence, they have concluded that C cannot be directly involved in YL [129]. This theoretical result has also been confirmed by other calculations reported by Bogusławski et al. [130,131]. However, it is clear that none of the *theoretical* calculations can counter the strong *experimental* evidence of the important role of C in the formation of YL. This latter conclusion is also supported by obvious limitations of the theoretical approaches used to calculate the properties of deep centers in semiconductors,

especially given the complexity of the real defect-impurity complex involved in YL as well as the present immaturity of GaN.

Our data also shows that implantation of O enhances YL only in samples with a relatively low initial concentration of free carriers, suggesting that shallow donor levels associated with O are involved in DAP transitions presumably responsible for YL. However, at present, additional studies are needed to better understand the role of O in the formation of the YL band in GaN.

Finally, our data indicates that H is also involved in a complex giving rise to a luminescence band in the yellow spectral region. This result is consistent with previous reports by Zhang and Kuech [106, 114], who have shown that an introduction of H during GaN crystal growth results in a strong YL band with properties (such as the temperature dependence of photoluminescence intensity) different from those of the C-related YL band. However, at this stage, the microscopic model for the H-related complex which gives rise to the above H-related YL band is not clear, and this issue requires additional systematic studies.

7.7 Summary

Optical properties of ion-implanted GaN have been studied by CL. Results show that the apparent recovery of CL emission from ion-implanted GaN by postimplantation annealing at temperatures up to 1050°C is often caused by changes in the efficiency of the absorption of visible light generated by the electron beam in virgin GaN, beyond the implanted layer. Thus, CL emission in the implanted layer can remain completely quenched even after such annealing. Annealing at temperatures up to 1050 °C can lead to (partial) recovery of CL emission from the layer modified by ion bombardment only for rather low dose light-ion implantation (such as $\sim 10^{12}$ cm^{-2} of 150 keV C ions).

We have also studied the chemical origin of the YL band in GaN by ion implantation and CL. Results have indicated that H, C, and O, presumably in combination with point defects, are involved in the formation of the YL in GaN, while lattice defects alone (as well as the other species implanted such as B, N, and Si) do not give rise to YL. In addition to giving rise to YL, C-related complexes appear to act as efficient nonradiative recombination centers. Our data strongly suggests that several (at least two: H- and C-

related) radiative recombination channels contribute to the formation of the YL band. The H-related YL band is slightly blue-shifted relative to the C-related YL band in the case of relatively high excitation densities. This H-related peak exhibits a DAP-like behavior (i.e., a blue-shift with increasing excitation density), while the position of the C-related peak does not show any detectable shift for the range of excitation densities used in this study. The results of this study may have significant implications for the development of an adequate microscopic model for YL in GaN.

Chapter 8

Electrical characterization of ion-implanted GaN

8.1 Introduction

Ion implantation plays an important role in the development of discrete devices and integrated circuits based on III-V compound semiconductors. In particular, ion irradiation can convert conductive layers of III-V materials into highly resistive ones (see, for example, a review in Ref. [132]). Selective masking of the semiconductor surface with a photoresist followed by ion irradiation is a practical way to electrically isolate closely spaced devices. It is generally believed that trapping of carriers at deep centers associated with irradiation-produced damage (defect isolation) or with implanted species (chemical isolation) is the mechanism responsible for electrical isolation [132].

Irradiation with keV ions has previously been applied for electrical isolation of GaN [133–137]. However, the physical processes involved in this technological step are not completely understood at present. It has been shown that isolation which withstands thermal annealing at temperatures, at least, up to $\sim$ 500 °C can be readily achieved by irradiation of GaN with keV H, He, N, O, Ti, Cr, or Fe ions [133–137]. However, in the case of keV ion implantation, implanted species stop inside the conductive GaN layer, and the damage profile is highly nonuniform throughout the GaN film. This makes the separation of the effects of defect and chemical isolation (and, therefore, the interpretation of data) difficult. Another problem of electrical isolation by keV ion bombardment is that many GaN-based devices are fabricated from quite thick ($\geq$ 1.5 μm) GaN epilayers. In this case, the achievement of adequate electrical isolation using conventional keV ion bombardment requires a large number of overlapping implants, which is undesirable.

In this chapter, we study the formation of highly resistive layers in n-type GaN by MeV ion irradiation. In this case, projected ion ranges are greater than the thickness of the GaN epilayers studied, and the profiles of ion-beam-generated atomic displacements are essentially uniform throughout the conductive GaN film. A single MeV implant, hence, is sufficient to isolate a relatively thick GaN film. Moreover, irradiation with MeV ions has allowed us to separate the effects of defect isolation from chemical isolation and to avoid the formation of a layer with substantial defect-induced (hopping) conduction, which inevitably forms at the ion end-of-range region in the case of keV implants and usually complicates the interpretation of data [132].

Although the possibility of electrical isolation of GaN by ion bombardment has previously been demonstrated [133–137], systematic studies are still lacking in the literature. In

particular, the influence of irradiation parameters (such as ion mass, energy, sample temperature, and beam flux) has not been established. Such systematic studies are needed not only for a choice of irradiation conditions necessary for an effective electrical isolation of GaN-based devices but also for a better understanding of ion-beam processes responsible for isolation.

In Chapter 3, our study of the effect of implant conditions on the structural characteristics of GaN bombarded with keV ions has revealed very efficient dynamic annealing (i.e., defect migration and interaction) processes in this material at liquid nitrogen temperature (LN_2) and above. Although most of ion-beam-generated Frenkel pairs experience annihilation, dynamic annealing is not perfect, and stable lattice disorder accumulates with increasing ion dose. As a result, dynamic annealing causes stable damage which depends on collision cascade density, irradiation temperature, and beam flux. Furthermore, keV ion bombardment leads to the formation of a range of complex stable defects, many of which can be imaged by transmission electron microscopy as extended defects. For example, even irradiation with relatively light ^{12}C ions at keV energies leads to the formation of stable extended defects and exhibits a dependence of the damage buildup on irradiation temperature and beam flux, as discussed in Chapter 3.

Although dynamic annealing has been found to have a dramatic influence on residual damage in GaN bombarded with keV ions (see Chapter 3), particularly for heavy ions, its effect on electrical isolation using low-dose MeV light ions is not obvious.[1] Indeed, the effective diffusivity of irradiation-produced defects (which controls the level of dynamic annealing) may depend on ion dose and collision cascade density due to, for example, (i) processes of defect trapping and de-trapping during migration (which depend on the defect concentration in the lattice), (ii) possible dependence of defect migration parameters on the position of the chemical potential, and (iii) radiation-enhanced migration. It is, therefore, imperative that dynamic annealing (and associated irradiation-temperature and beam-flux dependencies) be investigated in the case of low-dose MeV light-ion bombardment used for

[1]It should be noted that typical ion irradiation studies of structural characteristics (presented in Chapters 3 – 5) and electrical isolation (presented in this chapter) are performed in very different ion dose regimes. Indeed, electrical isolation involves ion doses which result in the number of atomic displacements comparable with the concentration of free carriers (usually $\sim 10^{15} - 10^{18}$ cm^{-3}), whereas typical studies of structural characteristics use ion doses resulting in the number of atomic displacements comparable with the atomic concentration of the material ($\sim 10^{23}$ cm^{-3}).

Table 8.1: Original free electron concentration (n), effective Hall mobility (μ_{eff}), and sheet resistance (R_s) of the three GaN wafers used in our study of electrical characteristics of ion-implanted GaN.

Wafer	n (10^{17} cm^{-3})	μ_{eff} (cm^2 V^{-1} s^{-1})	R_s (Ω/sq)
I	3	570	218
II	23	350	92
III	56	330	37

electrical isolation. Hence, in this chapter, we study the effects of irradiation temperature, ion beam flux, and collision cascade density on electrical isolation of GaN. Results reveal that irradiation temperature and ion beam flux indeed affect electrical isolation in GaN. This suggests that the centers responsible for isolation are defect clusters or antisite-related defects, whereas ion-beam-generated Frenkel pairs (i.e., simple vacancies and interstitials in both sublattices in all possible charge states) in GaN are mobile during ion irradiation, at least at LN_2 and above.

8.2 Experimental

The n-type wurtzite GaN wafers used in this study were $\sim$ 2 μm thick (an $\sim$ 1.5 μm conductive layer over an $\sim$ 0.5 μm undoped GaN buffer), epitaxially grown on c-plane sapphire substrates by MOCVD. Wafers with three different free electron concentrations, achieved by Si doping, were grown. The corresponding electrical characteristics of the wafers are shown in Table 8.1.

Resistors of rectangular geometry (i.e., rectangular samples with two top Ohmic contacts on the opposite sides of each sample) cut from the above three GaN wafers were prepared (see Chapter 2 for further details). Ohmic contacts were formed by electron-beam evaporation of Ti/Al/Au (40 nm/120 nm/500 nm) and subsequent rapid thermal annealing at 900 °C for 30 seconds in an argon ambient at atmospheric pressure. Because the thickness of the contact layer was not sufficient to prevent the irradiation of the underlying GaN regions by MeV light-ion irradiation, additional masking of the contact regions with an aluminum foil was necessary.

These GaN resistors were irradiated at room temperature (RT) with 0.6 MeV ^{1}H, 3.0

MeV ^{7}Li, 6.6 MeV ^{12}C, and 6.6 MeV ^{16}O ions to doses in the range from 1×10^{10} to 2×10^{15} cm^{-2}. To study the effects of irradiation temperature and beam flux on the process of electrical isolation, some GaN resistors cut from wafer I (see Table 8.1) were irradiated at temperatures from -196 up to 150 °C with 0.6 MeV ^{1}H or 6.6 MeV ^{12}C ions to doses in the range from 1×10^{10} to 2×10^{15} cm^{-2}. Such ion energies were chosen to place the damage peak in the sapphire substrate, beyond the GaN layer. During bombardment, samples were tilted by 7° off the surface normal direction to minimize channeling. An average scanned ion beam flux was kept constant during implantation to different doses with different species. It is important to note that, during dose rate effect measurements, ion beam flux was varied by changing beam current from the ion source, without changing beam focusing (i.e., beam spot size) and beam scanning parameters. Sheet resistance (R_s) was measured *in-situ* at RT after each dose step using a Keithley 619 electrometer. In cases where irradiation was performed at low or elevated temperatures, samples were brought to RT before resistance measurements. Selected samples were also studied by Hall effect measurements using the Van der Pauw method [21]. Postirradiation annealing was carried out in a rapid thermal annealing (RTA) system in a nitrogen ambient at atmospheric pressure.

8.3 Results and discussion

8.3.1 Effect of initial free electron concentration

Figure 8.1(a) shows the evolution of R_s of resistors with different original free electron concentrations (n) exposed to irradiation with 6.6 MeV C ions at RT. This figure reveals that each of the curves has three distinct dose regions. The first region comprises the lowest doses, where R_s increases only slightly with increasing ion dose. The second region is characterized by a very fast increase in the value of R_s (by 9–10 orders of magnitude) in a relatively narrow dose interval. Such an increase in R_s is typically caused by the trapping of carriers at defects created by ion irradiation and damage-induced degradation of carrier mobility [132]. A similar sharp increase in R_s has been observed in all the samples studied, but the dose interval where it occurs shifts to higher doses proportionally with n. Figure 8.1(a) also shows that, with further increasing ion dose, R_s values reach their highest levels after a certain dose has been accumulated (Φ_{th} — the so called threshold dose). The third

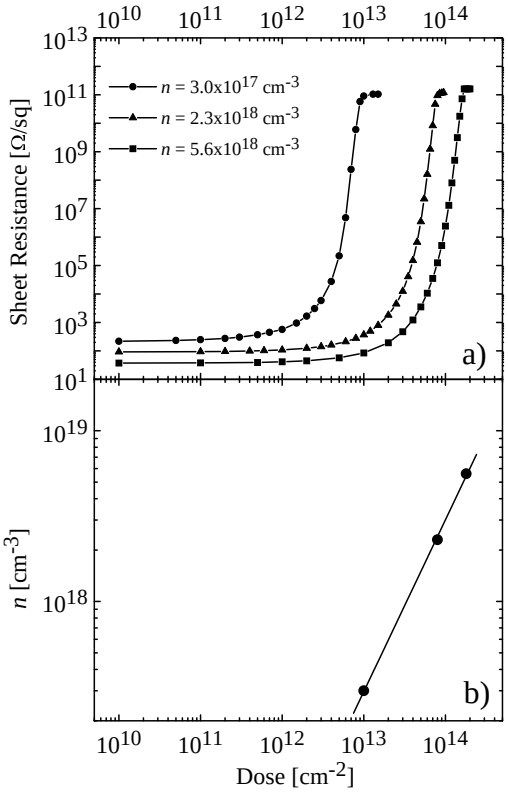

Figure 8.1: (a) Dose dependence of sheet resistance of GaN samples irradiated with 6.6 MeV ^{12}C ions with a beam flux of 6.4×10^{10} cm^{-2} s^{-1}. Samples had different original free electron concentrations, as indicated in the legend. (b) Original free carrier concentration of the samples vs threshold doses obtained from data in (a). The straight line with a slope of 1.0, representing the best fit, is shown.

dose region is for ion doses larger than Φ_{th}. With increasing ion dose above Φ_{th} and up to the maximum doses used in this work, the measured values of R_s remain approximately constant, forming a plateau. The levels of R_s at the plateaus shown in Fig. 8.1 are of the order of $1 - 2 \times 10^{11}$ Ω/sq. However, the real maximum values of R_s of GaN layers are expected to be even larger since the R_s values measured have a contribution from the parasitic resistances of the experimental set-up, which are of the same order of magnitude.

Figure 8.1(a) clearly shows that the dose dependence of R_s is not linear. A similar nonlinear dose dependence in GaN has previously been observed and explained by

Uzan-Saguy et al. [136] based on a theory of electron transport in doped polycrystalline materials. However, this nonlinearity of R_s as a function of ion dose may be more simply explained. Indeed, in the first approximation, the concentration of deep traps, created by ion irradiation, linearly increases with dose, and, consequently, n will linearly decrease with ion dose. Therefore, the strong nonlinear dose dependence of R_s observed in Fig. 8.1(a) is not unexpected, taking into account that $R_s \propto 1/n$. Moreover, with increasing number of traps in GaN, the concentration of charged scattering centers significantly increases, and electron mobility decreases, hence also contributing to strong nonlinearity of R_s on ion dose. In addition, the real dose dependence of R_s may be more complex. For example, the concentration of deep traps may not increase linearly with dose due to complex defect interaction and dynamic annealing processes, as discussed in detail in Chapter 3. We will return to the effect of dynamic annealing on the process of electrical isolation in Sect. 8.3.3.

In Fig. 8.1(b), the threshold doses of C ions [taken from Fig. 8.1(a)] are plotted vs the values of original free carrier concentration. Also shown in this figure is a straight line fit with a slope of 1.0, which shows that Φ_{th} increases linearly with the original concentration of free carriers. This result may support (despite the complexity of the real defect processes taking place in GaN during ion bombardment) the above assumption that the dose dependence of n has a form of $n(\Phi) = n(0) - A \times \Phi$, where Φ is ion dose, $n(\Phi)$ is free carrier concentration in the conductive layer after bombardment to dose Φ, and A is a constant which depends on ion mass and energy.

8.3.2 Effect of ion mass

Figure 8.2(a) shows the evolution of R_s in identical resistors prepared from wafer I (see Table 8.1) irradiated with 0.6 MeV H, 3.0 MeV Li, 6.6 MeV C, and 6.6 MeV O ions at RT.[2] It is seen that the curves progressively shift toward lower doses with increasing ion mass. This fact is related to the creation of a higher defect concentration in the conductive layer in the case of higher ion masses. In all the samples studied, R_s values reach their highest levels after Φ_{th} has been accumulated. Plotted in Fig. 8.2(b) is the number of

[2]To suppress the influence of beam flux on the efficiency of the production of lattice defects responsible for isolation (see Sect. 8.3.3), beam flux values were chosen (3.9×10^{11} for H, 1.6×10^{11} for Li, 6.4×10^{10} for C, and 2.1×10^{10} cm^{-2} s^{-1} for O ions) to keep the damage generation rate constant for irradiation with different species.

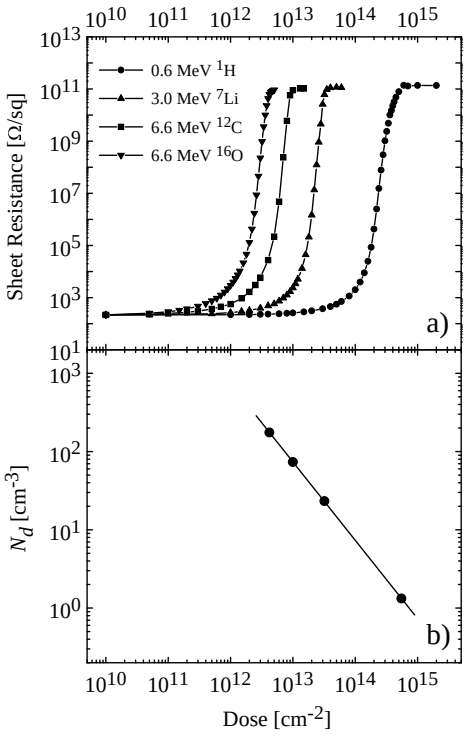

Figure 8.2: (a) Dose dependence of sheet resistance in identical samples ($n = 3\times10^{17}$ cm^{-3}) for irradiation with different ions, as indicated in the legend. (b) The estimated concentration of atomic displacements (N_d) is plotted vs threshold doses obtained from data in (a). Also shown is a straight line with a slope -1.0 which represents the best fit to experimental data.

atomic displacements (calculated using the TRIM code [22]) produced by the above four ion species in the conductive GaN layer vs the threshold doses. A straight line fit (with a slope of -1.0) shown in Fig. 8.2(b) demonstrates that the magnitude depends inversely on the number of atomic displacements, regardless of ion mass for the conditions used in this study.

The above results show that ion doses required for an effective isolation of GaN have simple linear and inverse dependencies on the values of initial free carrier concentration and ion-beam-produced atomic displacements, respectively. As a result, implant conditions necessary for an effective electrical isolation of a particular GaN-based device can be readily estimated based on experimental data presented here and the number of atomic

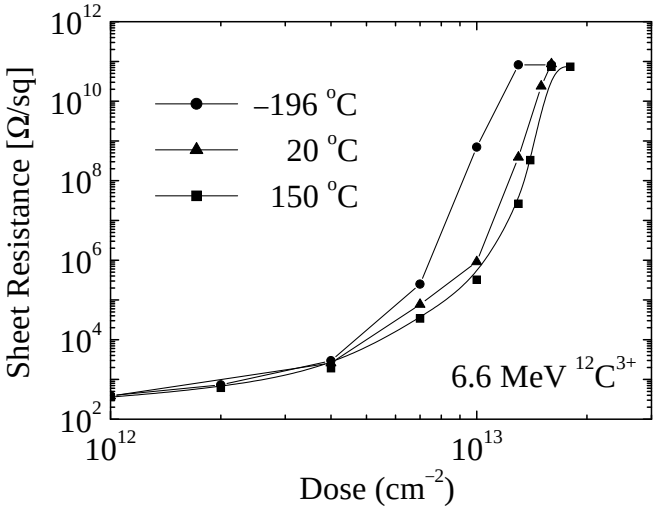

Figure 8.3: Dose dependence of sheet resistance of GaN samples irradiated with 6.6 MeV C ions with a beam flux of 1×10^{11} cm^{-2} s^{-1} at different temperatures, as indicated in the legend.

displacements calculated using, for example, the TRIM code [22]. The technological application of ion bombardment for electrical isolation of GaN based devices is also facilitated by very high thermal stability of such isolation. Indeed, in agreement with previous reports [133, 134], our data shows that the samples irradiated to doses above Φ_{th} remain highly resistive after RTA at temperatures up to ~ 900 °C, the maximum annealing temperature used in this study.

8.3.3 Effect of irradiation temperature and beam flux

Figure 8.3 shows the evolution of R_s of GaN resistors irradiated with 6.6 MeV C ions at three different temperatures. It is clearly seen from Fig. 8.3 that irradiation temperature affects the process of electrical isolation in GaN. Indeed, Fig. 8.3 reveals that the ion dose required to achieve a given value of R_s increases with increasing implantation temperature. This behavior is consistent with dynamic annealing during irradiation, whereby an increase in irradiation temperature enhances the migration, annihilation, and agglomeration processes of ion-beam-generated point defects. With increasing irradiation temperature, more migrating defects experience annihilation, and fewer point defects form the stable and electrically active complexes responsible for electrical isolation.

Interestingly, our results show that the density of collision cascades influences the

magnitude of the irradiation-temperature effect. For example, in contrast to the case of ^{12}C ions shown in Fig. 8.3, results on electrical isolation of GaN using very light 0.6 MeV ^{1}H ions with a beam flux of 3×10^{10} cm^{-2} s^{-1} reveal a negligible effect of sample temperature for temperatures varied from -196 up to 150 °C (the figure is not shown). We discuss the significance of this result below. However, here it should be noted that the maximum irradiation temperature which can be used in dynamic annealing studies is limited by the effects of post-irradiation annealing. Although isolation produced in GaN by large ion doses (when R_s reaches the maximum) is stable to RTA at temperatures as high as $\sim$ 900 °C (see Sect. 8.3.2), isolation produced by lower doses (where R_s is several orders of magnitude lower than the maximum isolation value) is not thermally stable at such high temperatures. Indeed, Fig. 8.4 shows results of isochronal annealing of a GaN sample bombarded with very light 0.6 MeV ^{1}H ions to a dose of 2.4×10^{14} cm^{-2}. It is seen from Fig. 8.4 that, even for rather low doses of very light ^{1}H ions (when R_s is $\sim$ 6 orders of magnitude lower than its maximum value), electrical isolation is stable to post-irradiation thermal annealing at temperatures below $\sim$ 225 °C. However, for annealing temperatures above $\sim$ 225 °C, Fig. 8.4 reveals a pronounced increase in sheet electron density and effective Hall mobility (and an associated decrease in R_s) due to annealing (though not complete) of ion-beam-produced defects. Hence, in the present study, the maximum irradiation temperature has been chosen below $\sim$ 225 °C, to ensure that little thermal annealing of the centers responsible for electrical isolation occurs during irradiation.

Shown in Fig. 8.5 is the evolution of R_s of GaN resistors bombarded with 6.6 MeV C ions at room temperature with different ion beam fluxes. It is seen from Fig. 8.5 that the isolation process depends on ion beam flux.[3] Indeed, the ion dose required to achieve a given value of R_s decreases with increasing beam flux. This so-called "normal" flux effect (when, with increasing beam flux, the level of ion-beam-produced damage also increases) is again consistent with the fact that dynamic annealing processes affect electrical isolation

[3]Note that, in Figs. 8.3 and 8.5, isolation curves shown by triangles do not overlap despite the apparently identical implant conditions used. This is due to different beam focusing (i.e., ion beam spot size) used to irradiate samples shown in Figs. 8.3 and 8.5. This result clearly illustrates that not only averaged beam flux but also instantaneous beam flux (determined by ion current in spot mode and ion beam spot size) should be taken into account during flux effect measurements.

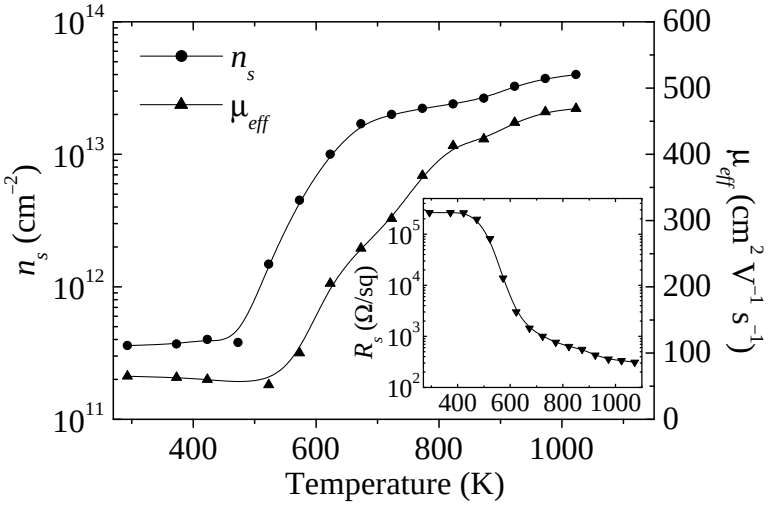

Figure 8.4: Dependencies of sheet electron density n_s (the left scale), effective Hall mobility μ_{eff} (the right scale), and sheet resistance R_s (the inset) on isochronal annealing temperature for a GaN sample implanted at RT with 0.6 MeV H ions with a beam flux of 4×10^{11} cm^{-2} s^{-1} to a dose of 2.4×10^{14} cm^{-2}. Each post-irradiation annealing step was performed for 1 min in an argon ambient at atmospheric pressure. Results of Hall effect measurements.

in GaN. Indeed, an increase in beam flux decreases the average time interval between collision cascades which spatially overlap. Increasing beam flux increases the generation rate of point defects and, hence, enhances the rate of interactions between mobile defects (generated in different collision cascades). Thus, as discussed later, increased beam flux aids the formation of stable defect clusters that are responsible for electrical isolation.

The influence of collision cascade density on the flux effect is illustrated in Fig. 8.6, which shows the evolution of R_s of GaN resistors irradiated at RT with different beam fluxes of very light 0.6 MeV ^{1}H ions (which produce very dilute collision cascades). Figure 8.6 reveals a negligible beam flux effect in this case. Hence, both beam-flux and irradiation-temperature dependencies of complex defect interaction processes appear to be controlled by the density of collision cascades. We discuss these processes and differences between H and C cases in more detail below.

It is clear that the effectiveness of dynamic annealing depends on the defect generation rate [atomic displacements/(cm^3 s)], which is determined by ion mass, energy, and beam flux. In the first approximation, the flux effect can be related to an effective time constant which indicates the time it takes for defects created in a collision cascade to sta-

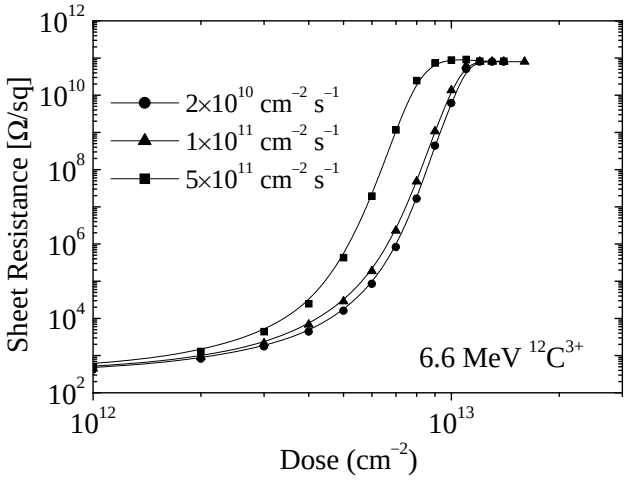

Figure 8.5: Dose dependence of sheet resistance of GaN samples irradiated with 6.6 MeV C ions at RT with different values of beam flux, as indicated in the legend.

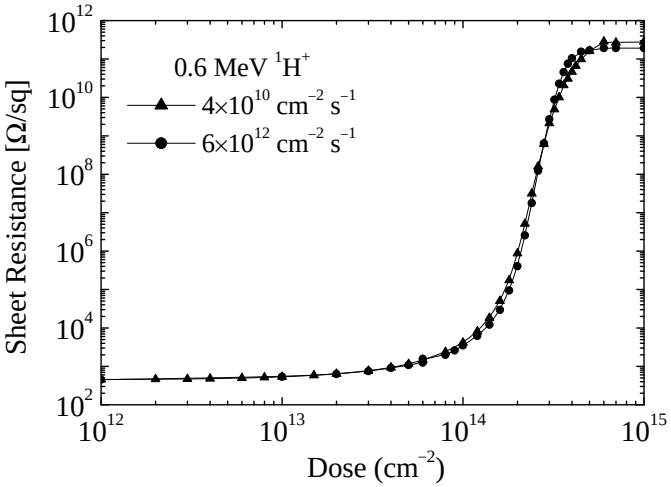

Figure 8.6: Dose dependence of sheet resistance of GaN samples irradiated with 0.6 MeV H ions at RT with different values of beam flux, as indicated in the legend.

bilize. Indeed, although the ballistic formation of a collision cascade by an impinging ion occurs in a very short time interval ($\sim$ 10 ps), cascade stabilization, involving processes of migration and interaction of point defects, proceeds for much longer times. This time constant, determined by the effective diffusivity of defects and defect interaction processes, obviously depends on both material properties and implant conditions (such as implantation temperature, beam flux, and collision cascade sizes and densities). In some cases, this time constant can be of the order of a second (see, for example, Ref. [138]). For a pronounced flux effect, it is important that such a time constant be comparable with the average time interval between collision cascades that spatially overlap. It is expected that the flux effect vanishes in cases of either very low or very high rates of defect generation, which corresponds to cases of either (i) low cascade densities and/or low values of beam flux or (ii) high cascade densities and/or high values of beam flux, respectively.[4]

The above scenario is consistent with our experimental data showing a negligible flux effect in the case of very light 0.6 MeV ^{1}H ions (Fig. 8.6) and a measurable flux effect for irradiation with heavier (but still relatively light) 6.6 MeV ^{12}C ions (Fig. 8.5). The above results also show that the dependence of electrical isolation on irradiation temperature, controlled by the density of collision cascades, vanishes in the case of very light 0.6 MeV ^{1}H ions. This is attributed to the fact that, in the case of very dilute collision cascades produced by very light ions, point defects are very mobile even at LN_2, resulting in a fast stabilization of collision cascades. In this case, an increase in irradiation temperature to 150 °C is not expected to significantly change the number of stable defect complexes formed during ion bombardment, which is consistent with our experimental data. In contrast to this case of very light ions, for heavier ^{12}C ions, when collision cascades are much denser and the interaction of point defects created in different overlapping collision cascades occurs (as indicated by the presence of the flux effect), irradiation temperature affects the rate and nature of defect interaction processes. Hence, in such a case, implantation temperature influences the nature and magnitude of the stable defect complexes responsible for electrical isolation (see Fig. 8.3). These results indicate that, for a material

[4]As discussed in detail in Chapter 3, a pronounced flux effect has also been observed in GaN bombarded with keV (heavy) ions, which generate dense collision cascades. It should be noted that the scenario for the flux effect proposed in this section, discussing the MeV light-ion irradiation regime, also applies for the case of keV ion bombardment considered in Chapter 3.

subject to substantial dynamic annealing such as GaN, an effective electrical isolation requires a careful consideration of all implant conditions (i.e., ion mass, energy, beam flux, and irradiation temperature).

Finally, a comment should be made on the nature of defects responsible for electrical isolation in GaN. The irradiation-temperature and beam-flux dependencies revealed in this study suggest that the centers responsible for isolation are not simple Frenkel pairs but the product of defect migration and interaction processes. The more complex nature of defects responsible for isolation in GaN is also strongly supported by the fact that these defect complexes have quite large dissociation energies, as revealed by their large thermal stability. Indeed, simple Frenkel pairs are expected to anneal out using much smaller thermal budgets than those necessary to recover R_s in GaN (> 900 °C). Possible candidates for defect complexes responsible for isolation in GaN are (i) interstitial or vacancy based defect clusters, (ii) complexes of defects with lattice impurities, and (iii) antisite-related defects. Our present experimental data cannot give preference to any of these defect types. Moreover, the processes of migration, clustering, and dissociation of point defect complexes in GaN have not yet been studied theoretically. Hence, at present, additional both experimental and theoretical studies are needed to identify defect types controlling the technologically important process of electrical isolation in GaN.

8.4 Summary

In summary, we have studied the electrical isolation of n-type GaN by MeV ion irradiation. Results show that sheet resistance of GaN layers increases up to $1 - 2 \times 10^{11}$ Ω/sq as a result of ion irradiation. The threshold dose (i.e., ion dose which is necessary to produce a concentration of effective deep level traps comparable with the initial concentration of free carriers) linearly depends on initial free electron concentration and is inversely proportional to the number of atomic displacements produced in the GaN film. Based on these results, the threshold dose necessary for isolation of a particular device can be readily calculated.

We have also studied the effect of irradiation temperature, beam flux, and collision cascade density on electrical isolation of n-type GaN by MeV light-ion irradiation. Results have revealed the important role of dynamic annealing processes in GaN during MeV light-

ion bombardment used for electrical isolation. This suggests that the centers responsible for electrical isolation are defect complexes or antisite-related defects, whereas ion-beam-generated simple Frenkel pairs in GaN are mobile and unstable during irradiation at LN_2 and above. The influence of irradiation temperature and beam flux revealed in the present study should be taken into account for choosing implant conditions necessary for an effective electrical isolation of GaN-based devices.

Chapter 9

Concluding remarks

Concluding remarks

The work presented in this thesis has resulted in the identification and understanding of a number of technologically important processes which occur in III-nitrides during ion bombardment. However, compared to our understanding of radiation effects in mature semiconductors (i.e., Si and GaAs), the understanding of the complex ion-beam processes in III-nitrides is in its infancy. Indeed, ion implantation studies in III-nitrides presented in this thesis have shown that these materials exhibit a quite unusual and rather complex behavior under ion bombardment. More work is needed before ion damage and its influence on structural, mechanical, optical, and electrical properties of III-nitrides are fully understood. Below, we briefly discuss current problems, mainly associated with implantation-produced disorder, which may hinder a successful application of ion implantation in the fabrication of III-nitrides-based devices. Further work is highly desirable to solve these problems.

The main problem which limits the application of ion implantation for doping and dry etching of III-nitrides is ion-beam-produced lattice disorder. Damage buildup studies presented in Chapter 3 have shown that GaN is extremely resistant to ion-beam disordering. Indeed, very high ion doses are usually required to induce bulk amorphization of GaN due to very efficient dynamic annealing processes in this material as compared to other semiconductors such as Si or GaAs. However, a study of optical and electrical characteristics of ion-implanted GaN presented in Chapters 7 and 8 have shown that GaN is, in fact, far from being resistant to ion-beam disordering. Indeed, even relatively low dose implantation with light ions is sufficient to dramatically quench the intensity of all characteristic luminescent peaks of GaN due to the formation of lattice defects, which act as nonradiative recombination centers. Electrical properties of III-nitrides are also very strongly modified by even relatively low dose implantation. Therefore, even low-dose implantation used for doping requires a postimplantation annealing step to remove ion-beam-produced defects, which are detrimental for device performance.

However, annealing of implantation disorder in III-nitrides faces difficulties. For example, luminescence studies presented in Chapter 7 have shown that annealing at temperatures up to ~ 1100 °C is not sufficient to completely remove lattice disorder produced in GaN even by very low dose light-ion bombardment (such as $10^{11} - 10^{12}$ cm^{-2} of 150 keV C ions). Annealing at higher temperatures is complicated by material decomposition and generally requires capping of the sample surface with a protective layer as well as special

RTA systems [9].

The problem of a satisfactory removal of implantation disorder becomes more difficult for higher dose ion implantation, which is desirable for *p*-type doping and Ohmic contact applications. Results presented in Chapters 3 and 5 have shown that high-dose ion implantation into III-nitrides, under a wide range of implant conditions, results in the formation of extended (planar) defects within the implanted layer. It is well known that extended defects in semiconductors are very resistive to annealing, requiring temperatures of roughly 2/3 of the melting point (or $\sim$ 1600 °C for GaN) [9]. The formation of such planar defects prior to amorphization may explain the well-known difficulties with postimplantation thermal annealing of ion-beam damage and dopant activation in GaN. Hence, more work is needed to understand the evolution of ion-beam-produced defect structures during postimplantation thermal annealing.

Another technologically important issue is the ability to adequately recrystallize amorphous layers in ion-bombarded GaN. Indeed, as discussed in Chapters 3, 4, and 5, high-dose ion implantation of III-nitrides can result in the formation of thick surface amorphous layers. In addition, a thin surface amorphous layer is often formed in GaN even during moderate-dose implantation due to the trapping of migrating point defects at the GaN surface or the amorphous/crystalline interface (see Chapter 3). The formation of thin surface amorphous layers is also expected during dry etching owing to very high ion doses employed in this process. These amorphous layers in III-nitrides represent a current problem due to the present inability to epitaxially recrystallize them. Indeed, results of studies discussed in Ref. [139] show that thermal annealing of amorphous GaN at temperatures above $\sim$ 500 °C results in polycrystallization, rather than in solid phase epitaxial growth (i.e., layer-by-layer recrystallization of an amorphous phase). Annealing of amorphous layers is also complicated by thermally-induced decomposition at temperatures above $\sim$ 400 °C, as has briefly been discussed in Chapter 4. Such undesirable decomposition is related to ion-beam-induced porosity of III-nitrides amorphized by ion bombardment. Unfortunately, amorphous and heavily disordered near-surface layers in III-nitrides, the inevitable result of dry etching, cannot be removed by an annealing step [9]. Additional studies are, therefore, required to address the issues related to avoiding, minimizing, or removing implantation-produced damage in III-nitrides.

References

[1] S.J. Pearton, J.C. Zolper, R.J. Shul and F. Ren, "GaN: Processing, defects, and devices," *Journal of Applied Physics* **86**(1): 1–78, 1999.

[2] J.W. Orton and C.T. Foxon, "Group III nitride semiconductors for short wavelength light-emitting devices," *Reports on Progress in Physics* **61**: 1–75, 1998.

[3] S.C. Jain, M. Willander, J. Narayan and R. Van Overstraeten, "III–nitrides: Growth characterization, and properties," *Journal of Applied Physics* **87**(3): 965–1006, 2000.

[4] H. Morkoç, S. Strite, G.B. Gao, M.E. Lin, B. Sverdlov and M. Burns, "Large-band-gap SiC, III-V nitride, and II-VI ZnSe-based semiconductor device technologies," *Journal of Applied Physics* **76**(3): 1363–1398, 1994.

[5] O. Ambacher, "Growth and applications of Group III nitrides," *Journal of Physics D: Applied Physics* **31**: 2653–2710, 1998.

[6] S.J. Pearton (editor), *GaN and Related Materials*, Gordon and Breach, Amsterdam, 1997.

[7] J.I. Pankove and T.D. Moustakas (editors), *Gallium Nitride (GaN) I*, Semiconductors and Semimetals, Academic Press, London, 1998.

[8] B. Rauschenbach, "Ion implantation, isolation and thermal processing of GaN and related materials," in "III-Nitride Semiconductors: Electrical, Structural and Defects Properties," (editor M.O. Manasreh), chapter 7, Elsevier, Amsterdam, 2000.

[9] S.O. Kucheyev, J.S. Williams and S.J. Pearton, "Ion implantation into GaN," *Materials Science and Engineering, R, Reports: A Review Journal* **33**(2-3): 51–107, 2001.

[10] C. Ronning, E.P. Carlson and R.F. Davis, "Ion implantation into gallium nitride," *Physics Reports* **351**(5): 349–385, 2001.

[11] H. Ryssel and H. Glawischnig (editors), *Ion Implantation Techniques*, Springer, New York, 1982.

[12] W.-K. Chu, J.W. Mayer and M.-A. Nicolet, *Backscattering Spectrometry*, Academic Press, Orlando, 1978.

[13] D.B. Williams and C.B. Carter, *Transmission Electron Microscopy*, Plenum Press, New York, 1996.

[14] D.A. Bonnell (editor), *Scanning Probe Microscopy: Theory, Techniques, and Applications*, Wiley-VCH, New York, 2000.

[15] V.J. Morris, A.R. Kirby and A.P. Gunning, *Atomic Force Microscopy for Biologists*, Imperial College Press, London, 1999.

[16] B.G. Yacobi and D.B. Holt, *Cathodoluminescence Microscopy of Inorganic Solids*, Plenum Press, New York and London, 1990.

[17] W.D. Nix, "Elastic and plastic properties of thin films on substrates: nanoindentation techniques," *Materials Science and Engineering A* **234-236**: 37–44, 1997.

[18] G.M. Pharr, "Measurements of mechanical properties by ultra-low load indentation," *Materials Science and Engineering A* **253**: 151–159, 1998.

[19] M.V. Swain, "Mechanical property characterization of small volumes of brittle materials with spherical indenters," *Materials Science and Engineering A* **253**: 160–166, 1998.

[20] A.B. Mann, R.C. Cammarata and M.A. Nastasi, "Nanoindentation: From angstroms to microns," *Journal of Materials Research* **14**(6): 2195, 1999.

[21] P. Blood and J.W. Orton, *The Electrical Characterisation of Semiconductors: Majority Carriers and Electron States*, Academic Press, London, 1992.

[22] J.P. Biersack and L.G. Haggmark, "A Monte Carlo computer program for the transport of energetic ions in amorphous targets," *Nuclear Instruments and Methods* **174**(1–2): 257–269, 1980.

[23] M. Nastasi, J.W. Mayer and J.K. Hirvonen, *Ion-Solid Interactions: Fundamentals and Applications*, Cambridge University Press, Cambridge, 1996.

[24] J.F. Gibbons and L.A. Christel, "Application of the Boltzmann transport equation to ion implantation in semiconductors and multilayer targets," in "Ion Implantation and Beam Processing," (editors J.S. Williams and J.M. Poate), chapter 3, pp. 59–80, Academic Press, Sydney, 1984.

[25] J.S. Williams, "Ion implantation of semiconductors," *Materials Science and Engineering, A* **253**: 8–15, 1998.

[26] R. Middleton, "A review of negative ion sources," *Revue de Physique Appliquee* **12**(10): 1435–1444, 1977.

[27] R. Middleton, "A survey of negative ions from a cesium sputter source," *Nuclear Instruments and Methods* **144**(3): 373–399, 1977.

[28] J.R. Tesmer and M. Nastasi (editors), *Handbook of Modern Ion Beam Materials Analysis*, Materials Research Society, Pittsburgh, Pennsylvania, 1995.

[29] J.A. Pankove, *Optical Processes in Semiconductors*, Dover, New York, 1971.

[30] T.Y. Tsui and G.M. Pharr, "Substrate effects on nanoindentation mechanical property measurements of soft films on hard substrates," *Journal of Materials Research* **14**(1): 292–301, 1999.

[31] J.S. Field and M.V. Swain, "A simple predictive model for spherical indentation," *Journal of Materials Research* **8**(2): 297–306, 1993.

[32] H.H. Tan, J.S. Williams, J. Zou, D.J. Cockayne, S.J. Pearton and R.A. Stall, "Damage to epitaxial GaN layers by silicon implantation," *Applied Physics Letters* **540**(16): 2364–2366, 1996.

[33] H.H. Tan, J.S. Williams, J. Zou, D.J. Cockayne, S.J. Pearton and C. Yuan, "Ion implantation processing of GaN epitaxial layers," *Electrochemical Society Proceedings* **96-11**: 142–148, 1996.

[34] S. Strite, P.W. Epperlein, A. Dommann, A. Rockett and R.F. Broom, "Properties of Zn implanted GaN," *Materials Research Society Symposium Proceedings* **395**: 795–800, 1996.

[35] N. Parikh, A. Suvkhanov, M. Lioubtchenko, E. Carlson, M. Bremser, D. Bray, R. Davis and J. Hunn, "Ion implantation of epitaxial GaN films: damage, doping and activation," *Nuclear Instruments and Methods in Physics Research Section B* **127/128**: 463–466, 1997.

[36] C. Liu, B. Mensching, K. Volz and B. Rauschenbach, "Lattice expansion of Ca and Ar ion implanted GaN," *Applied Physics Letters* **71**(16): 2313–2315, 1997.

[37] C. Liu, B. Mensching, M. Zeitler, K. Volz and B. Rauschenbach, "Ion implantation in GaN at liquid-nitrogen temperature: Structural characteristics and amorphization," *Physical Review B* **57**(4): 2530–2535, 1998.

[38] H.H. Tan, J.S. Williams, J. Zou, D.J. Cockayne, S.J. Pearton, J.C. Zolper and R.A. Stall, "Annealing of ion implanted gallium nitride," *Applied Physics Letters* **72**(10): 1190–1192, 1998.

[39] A. Suvkhanov, J. Hunn, W. Wu, D. Thomson, K. Price, N. Parikh, E. Irene, R.F. Davis and L. Krasnobaev, "Doping of GaN by ion implantation: does it work?" *Materials Research Society Symposium Proceedings* **512**: 475–480, 1998.

[40] B.J. Pong, C.J. Pan, Y.C. Teng, G.C. Chi, W.-H. Li and K.C. Lee, "Structural defects and microstrain in GaN induced by Mg ion implantation," *Journal of Applied Physics* **83**(11): 5992–5996, 1998.

[41] C. Liu, A. Wenzel, K. Volz and B. Rauschenbach, "Influence of substrate temperature on damage buildup and removal of ion implanted gallium nitride," *Nuclear Instruments and Methods in Physics Research Section B* **148**: 396–400, 1999.

[42] A. Wenzel, C. Liu and B. Rauschenbach, "Effect of implantation-parameters on the structural properties of Mg-ion implanted GaN," *Materials Science and Engineering B* **59**: 191–194, 1999.

[43] W.R. Wampler and S.M. Myers, "Ion channeling analysis of gallium nitride implanted with deuterium," *MRS Internet Journal of Nitride Semiconductor Research* **4S1**: G3.73, 1999.

[44] W. Jiang, W.J. Weber, S. Thevuthasan, G.J. Exarhos and B.J. Bozlee, "Effect of oxygen ion implantation in gallium nitride," *MRS Internet Journal of Nitride Semiconductor Research* **4S1**: G6.15, 1999.

[45] W. Jiang, W.J. Weber, S. Thevuthasan and V. Sutthanandan, "Properties of gallium disorder and gold profiles in GaN," *Materials Research Society Symposium Proceedings* **647**: O5.9, 2000.

[46] W. Jiang, W.J. Weber and S. Thevuthasan, "*In-situ* ion channeling study of gallium disorder and gold profiles in Au-implanted GaN," *Journal of Applied Physics* **87**(11): 7671–7678, 2000.

[47] A. Edwards, M.V. Rao, B. Molnar, A.E. Wickenden, O.W. Holland and P.H. Chi, "Ion implantation doping of OMCVD grown GaN," *Journal of Electronic Materials* **26**(3): 334–339, 1997.

[48] E. Alves, M.F. da Silva, J.C. Soares, R. Vianden, J. Bartels and A. Kozanecki, "Ion beam and photoluminescence studies of Er and O implanted GaN," *Nuclear Instruments and Methods in Physics Research Section B* **147**: 383–387, 1999.

[49] C. Liu, E. Alves, A.D. Sequeira, N. Franco, M.F. da Silva and J.C. Soares, "Fe ion implantation in GaN: Damage, annealing, and lattice site location," *Journal of Applied Physics* **90**(1): 81–86, 2001.

[50] B. Molnar, S.B. Qadri, S. Schiestel, R.M. Stroud and C.A. Carosella, "Surface elevation and strain in ion implanted GaN," *Materials Research Society Symposium Proceedings* **639**: G11.53.1–G11.53.6, 2001.

[51] A. Vantomme, S.M. Hogg, M.F. Wu, B. Pipeleers, M. Swart, S. Goodman, D. Auret, K. Iakoubovskii, G.J. Adriaenssens, K. Jacobs and I. Moerman, "Suppression of rare-earth implantation-induced damage in GaN," *Nuclear Instruments and Methods in Physics Research Section B* **175–177**: 148–153, 2001.

[52] S.O. Kucheyev, J.S. Williams, J. Zou, C. Jagadish and G. Li, "The effects of ion mass, energy, dose, flux and irradiation temperature on implantation disorder in GaN," *Nuclear Instruments and Methods in Physics Research Section B* **178**: 209–213, 2001.

[53] W. Jiang, W.J. Weber and S. Thevuthasan, "Defect annealing kinetics in irradiated 6H-SiC," *Nuclear Instruments and Methods in Physics Research Section B* **166-167**: 410–414, 2000.

[54] S.O. Kucheyev, J.S. Williams, C. Jagadish, J. Zou and G. Li, "Blistering of H-implanted GaN," *Journal of Applied Physics* **91**(6): 3928–3930, 2002.

[55] J.S. Williams, M. Conway, J.A. Davies, M. Petravic, H.H. Tan and J. Wong-Leung, "Analysis of semiconductors by ion channeling: Applications and pitfalls," *Nuclear Instruments and Methods in Physics Research Section B* **136-138**: 453–459, 1998.

[56] R.D. Goldberg, J.S. Williams and R.G. Elliman, "Preferential amorphization at extended defects of self-ion-irradiated silicon," *Physical Review Letters* **82**(4): 771–774, 1999.

[57] X.A. Cao, S.J. Pearton, A.P. Zhang, G.T. Dang, F. Ren, R.J. Shul, L. Zhang, R. Hickmas and J.M. Van Hove, "Electrical effects of plasma damage in *p*-GaN," *Applied Physics Letters* **75**(17): 2569–2571, 1999.

[58] C.R. Eddy, Jr. and B. Molnar, "Plasma etch-induced conduction changes in gallium nitride," *Journal of Electronic Materials* **28**(3): 314–218, 1999.

[59] H.H. Andersen, "Ion-bombardment-induced compositional changes in alloys and compounds," in "Ion Implantation and Beam Processing," (editors J.S. Williams and J.M. Poate), chapter 6, pp. 128–188, Academic Press, Sydney, 1984.

[60] S.O. Kucheyev, J.S. Williams, C. Jagadish, J. Zou and G. Li, "Damage buildup in GaN under ion bombardment," *Physical Review B* **62**(11): 7510–7522, 2000.

[61] K. Schmid, "Some new aspects for the evaluation of disorder profiles in silicon by backscattering," *Radiation Effects* **17**: 201–207, 1973.

[62] R.A. Brown and J.S. Williams, "Nucleation-limited amorphization of GaAs at elevated temperatures," *Physical Review B* **55**(19): 12 852–12 855, 1997.

[63] J.A. Davies, "High energy density collision cascades and spike effects," in "Ion Implantation and Beam Processing," (editors J.S. Williams and J.M. Poate), chapter 4, pp. 81–99, Academic Press, Sydney, 1984.

[64] S.O. Kucheyev, "Amorphous zone evolution in Si during elevated temperature ion bombardment," *Nuclear Instruments and Methods in Physics Research Section B* **174**(1-2): 130–136, 2001.

[65] W.J. Weber, "Models and mechanisms of irradiation-induced amorphization in ceramics," *Nuclear Instruments and Methods in Physics Research Section B* **166–167**: 98–106, 2000.

[66] M.W. Bench, I.M. Robertson, M.A. Kirk and I. Jenčič, "Production of amorphous zones in GaAs by the direct impact of energetic heavy ions," *Journal of Applied Physics* **87**(1): 49–56, 2000.

[67] I. Jenčič, M.W. Bench, I.M. Robertson and M.A. Kirk, "Electron-beam-induced crystallization of isolated amorphous regions in Si, Ge, GaP, and GaAs," *Journal of Applied Physics* **78**(2): 974–982, 1995.

[68] L.A. Christel and J.F. Gibbons, "Stoichiometric disturbances in ion implanted compound semiconductors," *Journal of Applied Physics* **52**(8): 5050–5055, 1981.

[69] J.F. Gibbons, "Ion implantation in semiconductors II. Damage production and annealing," *Proceedings of IEEE* **60**: 1062–1096, 1972.

[70] F. Priolo and E. Rimini, "Ion-beam-induced epitaxial crystallization and amorphization in silicon," *Materials Science Reports* **5**(7-8): 319–379, 1990.

[71] A.I. Titov and S.O. Kucheyev, "Ion beam induced amorphous-crystalline phase transition in Si: Quantitative approach," *Nuclear Instruments and Methods in Physics Research Section B* **168**(3): 375–388, 2000.

[72] S.O. Kucheyev, J.S. Williams, A.I. Titov, G. Li and C. Jagadish, "Effect of the density of collision cascades on implantation damage in GaN," *Applied Physics Letters* **78**(18): 2694–2696, 2001.

[73] J.S. Williams, "Materials modification with ion beams," *Reports on Progress in Physics* **49**(5): 491–588, 1986.

[74] J.P. de Souza, Yu. Suprun-Belevich, H. Boudinov and C.A. Cima, "Damage accumulation in Si crystal during ion implantation at elevated temperatures: Evidence of chemical effects," *Journal of Applied Physics* **87**(12): 8385–8388, 1994.

[75] J.P. de Souza, H. Boudinov and P.F.P. Fichtner, "Enhanced damage accumulation in carbon implanted silicon," *Applied Physics Letters* **64**(26): 3596–3597, 1994.

[76] H.M. Naguib and R. Kelly, "Criteria for bombardment-induced structural changes in non-metallic solids," *Radiation Effects* **25**: 1–12, 1975.

[77] R. Kelly, "Phase changes in insulators produced by particle bombardment," *Nuclear Instruments and Methods* **182/183**: 351–378, 1981.

[78] S.J. Zinkle and L.L. Snead, "Influence of irradiation spectrum and implanted ions on the amorphization of ceramics," *Nuclear Instruments and Methods in Physics Research Section B* **116**: 92–101, 1996.

[79] B.R. Appleton, O.W. Holland, J. Narayan, O.E. Schow III, J.S. Williams, K.T. Short, and E. Lawson, "Characterization of damage in ion implanted Ge," *Applied Physics Letters* **41**(8): 711–712, 1982.

[80] L.M. Wang and R.C. Britcher, "Amorphization, morphological instability and crystallization of krypton ion irradiated germanium," *Philosophical Magazine A* **64**(6): 1209–1223, 1991.

[81] G.L. Destefanis and J.P. Gailliard, "Very efficient void formation in ion implanted InSb," *Applied Physics Letters* **36**(1): 40–42, 1980.

[82] R. Callec, P.N. Favennec, M. Salvi, H. L'Haridon, and M. Gauneau, "Anomalous behavior of ion-implanted GaSb," *Applied Physics Letters* **59**(15): 1872–1874, 1991.

[83] T.K. Chaki and J.C.M. Li, "Radiation damage in an amorphous Lennard-Jones solid. A computer simulation," *Philosophical Magazine B* **51**(5): 557–565, 1985.

[84] J.A. Van Vechten, "Asymmetry in the displacement energy for frenkel-pair production in semiconductors and the conversion of n-type AlN to p-type," in "Radiation Effects in Semiconductors, Institute of Physics, Conference Series Number 31," (editors N.B. Urli and J.W. Corbett), chapter 7, pp. 441–447, The Institute of Physics, Bristol, 1977.

[85] L. Cartz, F.G. Karioris and R.A. Fournelle, "Heavy ion bombardment of silicates and nitrides," *Radiation Effects* **54**: 57–64, 1981.

[86] S.J. Zinkle, L.L. Snead, W.S. Eatherly, J.W. Jones and D.K. Hensley, "Effect of low temperature ion irradiation on the microstructure of nitride ceramics," *Materials Research Society Symposium Proceedings* **540**: 305–310, 1999.

[87] T. Yano and T. Iseki, "A HREM study of neutron-irradiation-induced dislocations in aluminium nitride," *Philosophical Magazine Letters* **62**(2): 83–87, 1990.

[88] T. Yano, K. Ichikawa, M. Akiyoshi and Y. Tachi, "Neutron irradiation damage in aluminium oxide and nitride ceramics up to a fluence of 4.2×10^{26} n/m^2," *Journal of Nuclear Materials* **283-287**: 947–951, 2000.

[89] K. Atobe, M. Okada and M. Nakagawa, "Irradiation temperature dependence of defect formation of nitrides (AlN and c-BN) during neutron irradiations," *Nuclear Instruments and Methods in Physics Research Section B* **166-167**: 57–63, 2000.

[90] K. Atobe, M. Honda, N. Fukuoka, M. Okada and M. Nakagawa, "F-type centers in neutron-irradiated AlN," *Japanese Journal of Applied Physics* **29**(1): 150–152, 1990.

[91] M. Honda, K. Atobe, N. Fukuoka, M. Okada and M. Nakagawa, "Electron paramagnetic center in neutron-irradiated AlN," *Japanese Journal of Applied Physics* **29**(4): L652–L654, 1990.

[92] T. Yano, H. Miyazaki and T. Iseki, "Effect of isochronal annealing on thermal diffusivity of neutron-irradiated AlN," *Journal of Nuclear Materials* **230**: 74–77, 1996.

[93] S.O. Kucheyev, J.E. Bradby, J.S. Williams, C. Jagadish, M. Toth, M.R. Phillips, and M.V. Swain, "Nanoindentation of epitaxial GaN films," *Applied Physics Letters* **77**(21): 3373–3375, 2000.

[94] J.E. Bradby, S.O. Kucheyev, J.S. Williams, J. Wong-Leung, M.V. Swain, P. Munroe, G. Li, and M.R. Phillips, "Indentation-induced damage in GaN epilayers," *Applied Physics Letters* **80**(3): 383–385, 2002.

[95] J.S. Williams, Y. Chen, J. Wong-Leung, A. Kerr, and M.V. Swain, "Ultra-micro-indentation of silicon and compound semiconductors with spherical indenters," *Journal of Materials Research* **14**(6): 2338–2343, 1999.

[96] T.F. Page, W.C. Oliver and C.J. McHargue, "The deformation behavior of ceramic crystals subjected to very low (nano)indentations," *Journal of Materials Research* **7**(2): 450–473, 1992.

[97] T. Ogino and M. Aoki, "Mechanisms of yellow luminescence in GaN," *Japanese Journal of Applied Physics* **19**(12): 2395–2405, 1980.

[98] E.R. Glaser, T.A. Kennedy, K. Doverspike, L.B. Rowland, D.K. Gaskill, J.A. Freitas, Jr., M. Asif Khan, D.T. Olson, J.N. Kuznia and D.K. Wickenden, "Optically detected magnetic resonance of GaN films grown by organometallic chemical-vapor deposition," *Physical Review B* **51**(19): 13 326–13 336, 1995.

[99] P. Perlin, T. Suski, H. Teisseyre, M. Leszczynski, I. Grzegory, J. Jun, S. Porowski, P. Bogusławski, J. Bernholc, J.C. Chervin, A. Polian and T.D. Moustakas, "Towards the identification of the dominant donor in GaN," *Physical Review Letters* **75**(2): 296–299, 1995.

[100] T. Suski, P. Perlin, H. Teisseyre, M. Leszczyński, I. Grzegory, J. Jun, M. Boćkowski, S. Porowski and T.D. Moustakas, "Mechanisms of yellow luminescence in GaN," *Applied Physics Letters* **67**(15): 2188–2190, 1995.

[101] I. Shalish, L. Kronik, G. Segal, Y. Rosenwaks, Y. Shapira, U. Tisch and J. Salzman, "Yellow luminescence and related deep levels in unintentionally doped GaN films," *Physical Review B* **59**(15): 9748–9751, 1999.

[102] A.M. Stoneham, *Theory of Defects in Solids: Electronic Structure of Defects in Insulators and Semiconductors*, Clarendon Press, Oxford, 1975.

[103] J.I. Pankove and J.A. Hutchby, "Photoluminescence of ion-implanted GaN," *Journal of Applied Physics* **47**(12): 5387–5390, 1976.

[104] R. Niebuhr, K. Bachem, K. Dombrowski, M. Maier, W. Pletschen and U. Kaufmann, "Basic studies of gallium nitride growth on sapphire by metalorganic chemical-vapor-deposition and optical-properties of deposited layers," *Journal of Electronic Materials* **24**(11): 1531–1534, 1995.

[105] A.Y. Polyakov, M. Shin, J.A. Freitas, M. Skowronski, D.W. Greve and R.G. Wilson, "On the origin of electrically active defects in AlGaN alloys grown by organometallic vapor phase epitaxy," *Journal of Applied Physics* **80**(11): 6349–6354, 1996.

[106] R. Zhang and T.F. Kuech, "Photoluminescence of carbon in situ doped GaN grown by halide vapor phase epitaxy," *Applied Physics Letters* **72**(13): 1611–1613, 1998.

[107] R. Zhang, L. Zhang, N. Perkins and T.F. Kuech, "Influence of C, N and O ion-implantation on yellow luminescence," *Materials Research Society Symposium Proceedings* **512**: 321–326, 1998.

[108] U. Birkle, M. Fehrer, V. Kirchner, S. Einfeldt, D. Hommel, S. Strauf, P. Michler and J. Gutowski, "Studies on carbon as alternative *p*-type dopant for gallium nitride," *MRS Internet Journal of Nitride Semiconductor Research* **4S1**: G6.6, 1999.

[109] G. Li, S.J. Chua, S.J. Xu, W. Wang, P. Li, B. Beaumont and P. Gibart, "Nature and elimination of yellow-band luminescence and donor-acceptor emission of undoped GaN," *Applied Physics Letters* **74**(19): 2821–2823, 1999.

[110] P.B. Klein, S.C. Binari, K. Ikossi, A.E. Wickenden, D.D. Koleske and R.L. Henry, "Current collapse and the role of carbon in AlGaN/GaN high electron mobility transistors grown by metalorganic vapor-phase epitaxy," *Applied Physics Letters* **79**(21): 3527–3529, 2001.

[111] J. Elsner, R. Jones, M.I. Heggie, P.K. Sitch, M. Haugk, Th. Frauenheim, S. Öberg and P.R. Briddon, "Deep acceptors trapped at threading-edge dislocations in GaN," *Physical Review B* **58**(19): 12 571–12 574, 1998.

[112] M. Toth, K. Fleischer, and M.R. Phillips, "Direct experimental evidence for the role of oxygen in the luminescent properties of GaN," *Physical Review B* **59**(3): 1575–1578, 1999.

[113] G. Salviati, M. Albrecht, C. Zanotti-Fregonara, N. Armani, M. Mayer, Y. Shreter, M. Guzzi, Yu.V. Melnik, K. Vassilevski, V.A. Dmitriev and H.P. Strunk, "Cathodoluminescence and transmission electron microscopy study of the influence of crystal defects on optical transitions in GaN," *Physica Status Solidi A* **171**(1): 325–339, 1999.

[114] R. Zhang and T.F. Kuech, "Hydrogen induced yellow luminescence in GaN grown by halide vapor phase epitaxy," *Journal of Electronic Materials* **27**(5): L35–L39, 1998.

[115] U. Kaufmann, M. Kunzer, H. Obloh, M. Maier, Ch. Manz, A. Ramakrishnan and B. Santic, "Origin of defect-related photoluminescence bands in doped and nominally undoped GaN," *Physical Review B* **59**(8): 5561–5567, 1999.

[116] Y.H. Kwon, S.K. Shee, G.H. Gainer, G.H. Park, S.J. Hwang and J.J. Song, "Time-resolved study of yellow and blue luminescence in Si- and Mg-doped GaN," *Applied Physics Letters* **76**(7): 840–842, 2000.

[117] E. Silkowski, Y.K. Yeo, R.L. Hengehold, M.A. Khan, T. Lei, K. Evans and C. Cerny, "Annealing study of ion implanted MOCVD and MBE grown GaN," *Materials Research Society Symposium Proceedings* **395**: 813–818, 1996.

[118] C. Ronning, E.P. Carlson, D.B. Thomson and R.F. Davis, "Optical activation of Be implanted into GaN," *Applied Physics Letters* **73**(12): 1622–1624, 1998.

[119] K. Fleischer, M. Toth, M.R. Phillips, J. Zou, G. Li and S.J. Chua, "Depth profiling of GaN by cathodoluminescence microanalysis," *Applied Physics Letters* **74**(8): 1114–1116, 1999.

[120] A. Billeb, W. Grieshaber, D. Stocker, E.F. Schubert and R.F. Karlicek, Jr., "Microcavity effects in GaN epitaxial films and in Ag/GaN/sapphire structures," *Applied Physics Letters* **70**(21): 2790–2792, 1997.

[121] K. Kanaya and S. Okayama, "Penetration and energy-loss theory of electrons in solid targets," *Journal of Physics D: Applied Physics* **5**: 43–58, 1972.

[122] S.O. Kucheyev, M. Toth, M.R. Phillips, J.S. Williams and C. Jagadish, "Effect of excitation density on cathodoluminescence from GaN," *Applied Physics Letters* **79**(14): 2154–2156, 2001.

[123] K. Knobloch, P. Perlin, J. Krueger, E.R. Weber and C. Kisielowski, "Effect of internal absorption on cathodoluminescence from GaN," *MRS Internet Journal of Nitride Semiconductor Research* **3**(4), 1998.

[124] M.A. Kumakhov and F.F. Komarov, *Energy Loss and Ion Ranges in Solids*, Gordon and Breach, New York, 1981.

[125] B.-C. Chung and M. Gershenzon, "The influence of oxygen on the electrical and optical properties of GaN crystals grown by metalorganic vapor phase epitaxy," *Journal of Applied Physics* **72**(2): 651–659, 1992.

[126] M. A. Reshchikov, P. Visconti and H. Morkoç, "Blue photoluminescence activated by surface states in GaN grown by molecular beam epitaxy," *Applied Physics Letters* **78**(2): 177–179, 2001.

[127] J.S. Colton, P.Y. Yu, Teo K.L., E.R. Weber, P. Perlin, I. Grzegory and K. Uchida, "Selective excitation and thermal quenching of the yellow luminescence of GaN," *Applied Physics Letters* **75**(21): 3273–3275, 1999.

[128] F.K. Koschnick, K. Michael, J.M. Spaeth, B. Beaumont and P. Gibart, "Optically detected magnetic-resonance mapping on the yellow luminescence in GaN," *Applied Physics Letters* **76**(14): 1828–1830, 2000.

[129] J. Neugebauer and C.G. Van de Walle, "Gallium vacancies and the yellow luminescence in GaN," *Applied Physics Letters* **69**(4): 503–505, 1996.

[130] P. Bogusławski, E. Briggs and J. Bernholc, "Amphoteric properties of substitutional carbon impurity in GaN and AlN," *Applied Physics Letters* **69**(2): 233–235, 1996.

[131] P. Bogusławski and J. Bernholc, "Doping properties of C, Si and Ge impurities in GaN and AlN," *Physical Review B* **56**(15): 9496–9505, 1997.

[132] S.J. Pearton, "Ion implantation for isolation of III-V semiconductors," *Materials Science Report* **4**(8): 313–367, 1990.

[133] S.C. Binari, H.B. Dietrich, G. Kelner, L.B. Rowland, K. Doverspike, and D.K. Wickenden, "H, He, and N implant isolation of *n*-type GaN," *Journal of Applied Physics* **78**(5): 3008–3011, 1995.

[134] S.J. Pearton, C.B. Vartuli, J.C. Zolper, C. Yuan, and R.A. Stall, "Ion implantation doping and isolation of GaN," *Applied Physics Letters* **67**(10): 1435–1437, 1995.

[135] S.J. Pearton, R.G. Wilson, J.M. Zavada, J. Han, and R.J. Shul, "Thermal stability of ^{2}H-implanted *n*- and *p*-type GaN," *Applied Physics Letters* **73**(13): 1877–1879, 1998.

[136] C. Uzan-Saguy, J. Salzman, R. Kalish, V. Richter, U. Tish, S. Zamir, and S. Prawer, "Electrical isolation of GaN by ion implantation damage: Experiment and model," *Applied Physics Letters* **74**(17): 2441–2443, 1999.

[137] X.A. Cao, S.J. Pearton, G.T. Dang, A.P. Zhang, F. Ren, R.G. Wilson, and J.M. Van Hove, "Creation of high resistivity GaN by implantation of Ti, O, Fe, or Cr," *Journal of Applied Physics* **87**(3): 1091–1095, 2000.

[138] J. Linnros and G. Holmen, "Dose rate dependence and time constant of the ion-beam-induced crystallization mechanism in silicon," *Journal of Applied Physics* **62**(12): 4737–4744, 1987.

[139] S.O. Kucheyev, J.S. Williams, C. Jagadish, J. Zou and G. Li, "Polycrystallization and surface erosion of amorphous GaN during elevated temperature ion bombardment," *Journal of Applied Physics* **88**(9): 5493–5495, 2000.